AALBORG UNIVERSITY
DENMARK

Electro-Mechanical System Design

4^{th} Semester Master Thesis

Analysis of Control Performance of a Reluctance Magnetic Lead Screw

Author:
Eric Falcon

Supervisor:
Peter Omand Rasmussen

June 3, 2020

Electro-Mechanical System Designnewline Study Board of Industry and Global Business Development
Fibigerstræde 16
9220 Aalborg East
Phone +45 99 40 93 09
lft@m-tech.aau.dk
www.en.ses.aau.dk

Master Thesis

Title:	Analysis of Control Performance of a Reluctance Magnetic Lead Screw
Author:	Eric Falcon
Semester:	4. Semester
ECTS:	30
Supervisor:	Peter Omand Rasmussen
Submission date:	03.06.2020
Pages:	83

Abstract

The following report is created by Eric Falcon as his masters thesis for the study program of Electro-Mechanical System Design at Aalborg University. The thesis project handles the modeling, analysis, and design of controllers for a reluctance magnetic lead screw linear actuator. The actuator consists of a permanent magnet motor, the rotor of which drives a magnetic nut, which then applies force to the linear translator. The intent of the project is to determine the control characteristics of the system and to investigate the maximum performance achievable by the machine.

The first portion of the report investigates the magnetic lead screw system and related previous works as well as handles the nonlinear and linear modeling of the motor and mechanical system. Additionally, testing of the model in comparison to the expected behavior is conducted in simulation. The model is then analysed with linear analysis methods and the change of behavior over the nonlinear operating region inspected.

The second portion of the report considers the development of controllers for the system. Based on the hardware expected to be used for the implementation of the project, a desired controller architecture is developed and, based on this, linear current controllers and three methods of position control are designed. The position control methods include a cascaded linear slip controller, a cascaded controller where the current necessary for a desired force is calculated, and a traditional LQR with feed forward of the discontinuous frictions in the system. Additionally, as the system has no position sensor, the sensor capabilities necessary for effective control are investigated as well as various methods for estimating the translator state without any sensor feedback.

In an ideal case, the developed controllers would have been implemented on the physical system, however as this was not completed, there are many possibilities for future work. Despite this, the control considerations for developing a control system for such a machine have been considered and a fairly high performance has been seen in simulated testing of the control in many scenarios.

Preface

This master thesis is the final work of Eric Falcon on the Electro-Mechanical System Design program at Aalborg University. The scope of the thesis is the control of a magnetically driven lead screw.

Reading Instructions
This report has features, which make it best to be read digitally e.g. hyper-references. Furthermore, it is necessary to read the report in color in order to properly distinguish lines in some of the figures. Throughout the report, figures, tables, and equations are numbered. The number of all figures, tables and equations refer to the chapter they are located in and the number of its kind in the chapter.

Numeric Notation
The English numeric notation is used. Numbers are therefore given with a point (.) used as a decimal separator.

Dot Notation
Dot notation will be used to denote the time derivative. i.e.:

$$\dot{x} = \frac{dx}{dt} \tag{1}$$

External Literature
Throughout the report references to external literature are made using the IEEE style with numbers in square brackets, which refer to a number in the bibliography at the end of the report.

Aalborg, 3rd ofJune 2020

Contents

Part I

Problem Analysis

Thesis Outline, Background, and Methodology 1

1.1 Thesis Outline

This thesis is carried out in order to investigate the performance capabilities of a reluctance magnetic lead screw system through the modeling, simulation, control design and testing. Each controller tested will be evaluated based on the tracking performance, the maximum cycle speed possible, and the sensor requirements in order to reach the highest performance possible in each configuration.

Figure 1.1: Food Grade RMLS Prototype

The controllers will be designed based on nonlinear and linear models created based on a physical test system available at the university. The system behavior and controllers will be evaluated and tested in simulation.

1.2 Project Background

The target system in this project is a reluctance magnetic lead screw actuator created by researchers at Aalborg university. The goal of creating such an actuator was to remove the mechanical friction component present in all other electrical linear actuators. This mechanical friction is by far the largest energy loss component in the mechanical motion and, in relation, brings increased mechanical wear and thus a reduced functional lifetime.

In creating these magnetic lead screw actuators, two major types were created. One type utilizes magnets in both the magnetic "nut" and on the "screw", see figure 1.2, to achieve a higher peak force whereas the other design utilizes magnetic reluctance and a "screw" geometry to achieve similar behavior with a lower force capability in exchange for compactness and improved manufacturability.

The concept of a magnetic lead screw originated from a patent in 1925[2] where an electro-magnetic linear actuator was designed for use in oil pumps or wells, and was further developed upon in 1945[3]

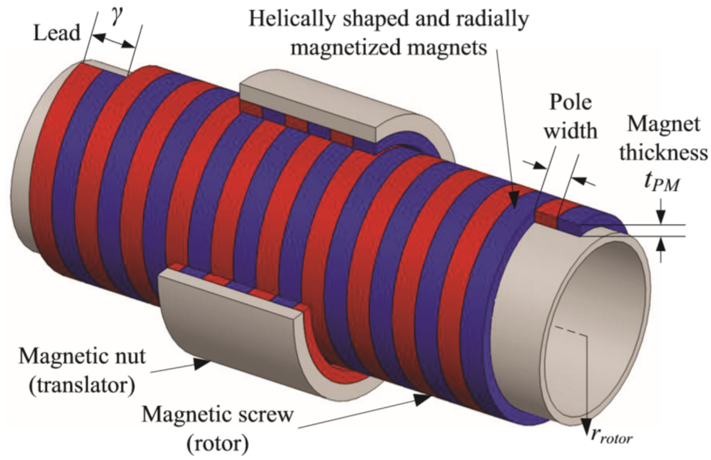

Figure 1.2: Cross section of a permanent magnet MLS as presented in [1]

where a reluctance type coupling is designed, and again in 1999[4] where a permanent magnet to permanent magnet design was developed[1].

Alternatively to magnetic lead screws, there are various competing technologies for linear actuation. The most simple actuation method is a mechanical lead screw where the force is transmitted through a nut and screw, there are various geometries with differing levels of efficiency, however, they all involve significant sliding friction. An improvement on lead screws are ballscrews where the surface on surface force transmission is driven through ball bearings which significantly reduce the friction. Other methods are solenoid, pneumatic, and hydraulic actuators which can have the benefits of speed or force but are more challenging to maintain accurate positions or velocities without a more complex control design. Screw type designs have the benefit of being drivable by a servomotor or stepper motors and as long as the applied force does not surpass the stall force, the position can be assumed to be accurate without a dedicated control design or position feedback. Magnetic lead screws are a middle ground between screw designs and the 'soft' actuators in that the position is not guaranteed, however if the position does not slip, the position will be between some known boundaries.

1.2.1 Magnetic Lead Screw

The working principle of a magnet mounted lead screw (MLS) is very similar to a typical mechanical lead screw with the difference being a magnetic coupling instead of a mechanical surface on surface coupling[1]. In order to create this coupling, both the magnetic "nut" and "screw" consist of helical structures of magnets. The interface between the magnets acts as a nonlinear spring to keep the two spirals aligned. From testing done in previous works[1], the 'spring force' is sinusoidal with relation to where the MLS translator is relative to the magnetic nut, further described in equation 2.2.

Such magnetic lead screws have the benefit of applying a linear force to a shaft without the force being transferred through a high friction coupling. The lead screws are capable of relatively high forces and may additionally be used for energy regeneration as there is no frictive force binding the system in place. On the other hand, the lack of friction in the system allows for the actuator to be more easily back-driven unless the motor applies a holding torque which may be beneficial in some applications but unwanted for others. Additionally, the lack of a mechanical interface means that it is possible for the actuator to slip when the applied force is greater than the peak force or 'stall force' from the magnets. The magnitude of this force is dependant on pole width, 'nut' length and diameter, magnet thickness, and the permanent magnet material.

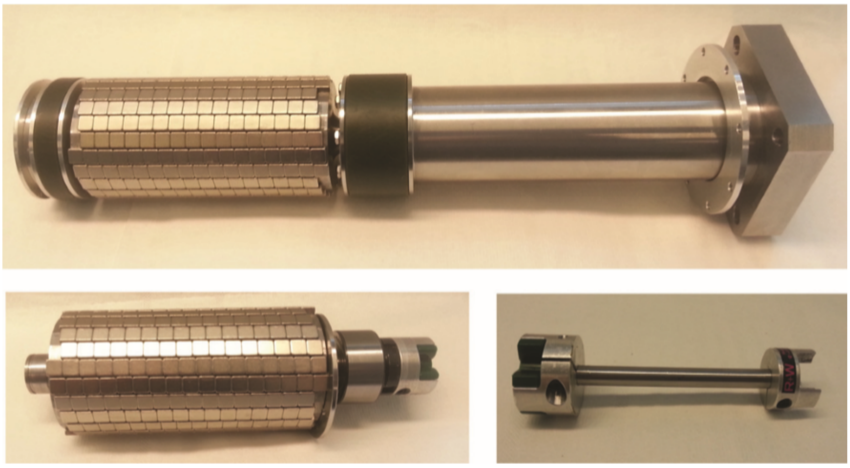

Figure 1.3: Permanent magnet MLS translator as presented in [5]

As the concept of slip is used in many contexts, the slipping of the MLS position past the corresponding thread on the magnetic nut will henceforth be described as a 'slip failure' and the motion of the Magnetic lead screw relative to the nut before failure referred to as 'slip'.

Magnetic leadscrews have been investigated for a variety of applications. Within Aalborg University, tests have been conducted in the evaluation of a PMLS as a damper in a automotive setting[1][5][6]. In order to improve the efficiency of modern vehicles, the ability to convert the linear motion of the shock absorbers on a car to energy is beneficial and due to the lack of mechanical locking and friction, the MLS design allows for this energy to be recaptured with an efficiency of up to 70%[1].

1.2.2 Reluctance Magnetic Lead Screw

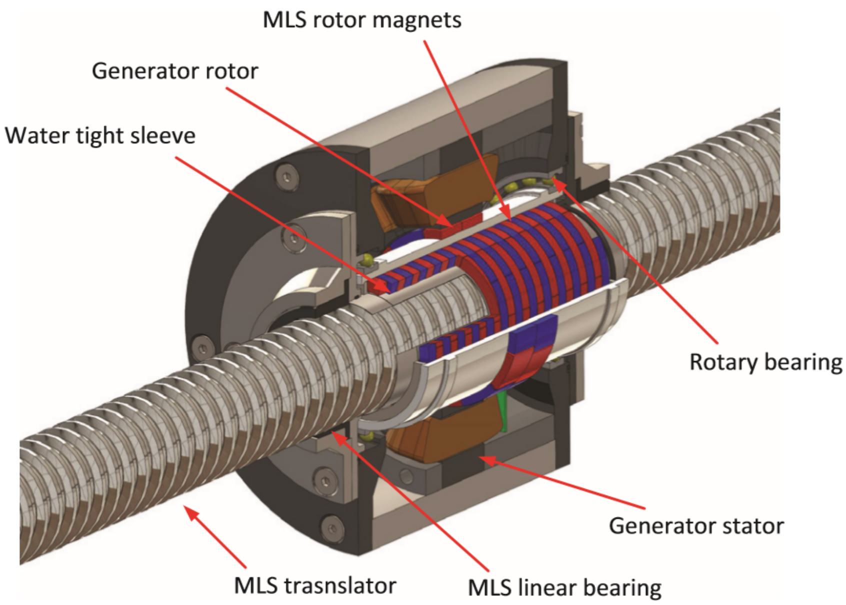

Figure 1.4: Reluctance magnetic lead screw cross section as presented in [7]

A reluctance magnetic lead screw (RMLS) operates very similarly to a permanent magnet lead screw. Again, the coupling behaves similarly to a mechanical lead screw but instead of having two helical magnet structures, the structure on the shaft is replaced with a screw-like geometry which is used for the magnetic linkage. The reluctance design is not as force dense as a permanent magnet design, however, it offers other beneficial capabilities due to its geometry. In the case of the lead screw used in this project, the ’nut’ is driven by the rotor of a permanent magnet brushless motor.

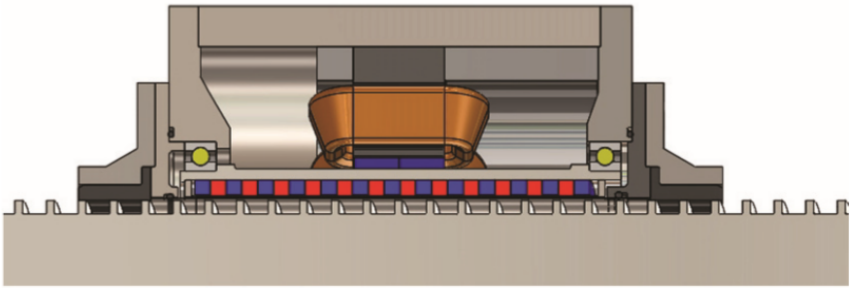

Figure 1.5: Reluctance magnetic lead screw magnet structure as presented in [7]

Though the reluctance based design is not as force dense, it has the benefit of not requiring magnets to be applied to the shaft allowing for much longer actuation distances without a significant material investment. The ’spring’ force of the RMLS is sinusoidal a withs the PMLS, however, the peak forces are a factor of ten lower. A paper released in 2019[8], demonstrates an alternative magnet layout with ferromagnetic rings dividing the magnets in the nut which, though reducing the peak force, results in a sawtooth force curve which could result in more linear system behavior.

The reluctance based machines have been previously investigated in relation to applications in the food industry as well as in a wave energy converter as both applications take advantage of the longer travel capabilities of the RMLS and do not require significant force capabilities. Additionally, the lack of magnets and their associated manufacturing processes allows the designed actuator to offer a more appealing financial outlook.

1.2.3 System Description

The hardware considered in this project consists of a reluctance magnetic lead screw, the permanent magnet synchronous motor(PMSM) used to drive it, a micro-controller for driving an inverter, and an inverter breakout board made to match the microcontroller development board.

As the practical implementation portion of the project was limited by the 2020 Covid-19 outbreak, the micro-controller and inverter will only be considered in respect to the potential limitations they present.

As can be seen in figure 1.4 and figure 1.5, the motor integrated in the linear actuator sits outside of the RMLS ’nut’ where the rotor magnets are attached to the exterior of the ’nut’ and the stator coils are mounted on the actuator housing. The configuration used is a three phase motor with a 12/8 coil/magnet configuration which gives four electrical/magnetic field rotations per mechanical rotation. The motor includes three hall effect sensors for position measurement giving six position measurements per period of magnetic rotation. Within the actuator housing, the rotor is maintained in place by standard ball bearings whereas the ’nut’ is held in place axially by linear bearings.

The reluctance magnetic lead screw has the parameters shown in table 1.1 as either defined in the specification, measured through testing, or as tested on a similar setup in previous works[6].

The permanent magnet synchronous motor used is considered to have the parameters shown in table 1.2.

Description	Parameter	Value	Source
Lead	γ	$0.022[m/rev]$	Spec.
No. Threads	n_{thread}	1	Spec.
Stall force	F_{stall}	$300[N]$	Test
Stall torque	τ_{stall}	$1.92[Nm]$	Spec.
Stroke length	x_{max}	$200[mm]$	Test
Screw diameter	r_s	$19[mm]$	Spec.
MLS static friction	μ_{ss}	$0.06[N]$	From [6]
MLS viscous friction	$B_v r$	$0.002[\frac{N}{m/s}]$	Test

Table 1.1: Parameters of the Reluctance Magnetic Lead Screw

Description	Parameter	Value	Source
Rated torque	τ_n	$2.0[Nm]$	Spec.
Rated speed	ω_{max}	$6000[rpm]$	Spec.
Poles	p	4	Spec.
Rated DC voltage	V_{max}	$48[v]$	Spec.
Rated current (per phase)	a_{max}	$30[A]$	Spec.
Permanent magnet flux linkage	λ_{pm}	$0.02[\frac{v}{rad/s}]$	Test
Inductance	L	$0.4[mH]$	Test
Resistance (per phase)	R	$0.33[\Omega]$	Test
Rotor static friction	μ_{sr}	$0.06[Nm]$	From [6]
Rotor viscous friction	$B_v r$	$0.002[\frac{Nm}{rad/s}]$	From [6]

Table 1.2: Parameters of the Permanent Magnet Motor

1.3 Intended Hardware

The design of the control system is based around the assumed use of a STM32F446-nucleo microcontroller board in combination with an X-NUCLEO-IHM08M1 inverter board.

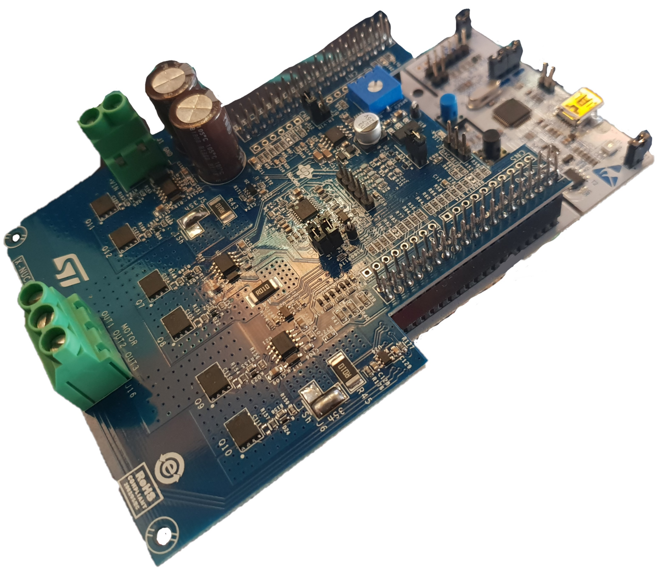

Figure 1.6: STM32f446nucleo with attached IHM08M1 inverter.

The STM32F446 Nucleo board is a development platform based around the STM32F446 microcontroller.

The board provides breakout pins for the I/O pins as well as a programming chip to flash the microcontroller without a requirement for an additional board. The STM32F446 microcontroller is a 32 bit ARM Cortex-M4 floating point processor with a main clock speed of up to 180MHz, and as common with the STM32 platform, it contains a large variety of peripheral functions.

Relevant to this project, the microcontroller offers a large number of configurable timers including two which offer three channel pulse width modulation (PWM) capabilities. The PWM capabilities allow for a single timer to be used to produce both positive and inverse signals which are then modifiable and triggerable through a single interrupt routine. Additionally, the board offers three twelve bit ADCs and a large number of general purpose I/O pins usable for current measurement and hall effect sensor inputs.

The IHM08M1 inverter considered in the project is a brushless DC motor driver expansion board for the nucleo development board platform. The board provides breakout pins intended for use with a hall effect sensor, as well as the power electronics for driving the motor. In relation to the power electronics, the board provides current sensing capabilities through 0.01Ω shunt resistors and associated signal amplification circuits[9]. The details of the amplifier and current measurement may be seen in section 6.3.1. The board is rated for a maximum DC voltage of 48 volts and a maximum per-phase current of 15amps.

1.3.1 Anticipated Challenges

The system as configured in the test setup comes with various limitations that can make controlling the movement challenging.

The primary challenge is the significant nonlinearity of the magnetic lead screw coupling force and the unstable regions reached if the linear force exceeds the MLS stall force. Traditional linear methods are likely to be effective with low accelerations and thus forces, however when accelerating quickly, the lead screw will enter an unstable region and become uncontrollable thus requiring more finesse in control design.

An additional challenge is the limited state feedback available. The motor phase currents are measurable accurately and quickly from the inverter however the rotor position is measured by three hall effect sensors which only give six measurements per motor pole pair which, for the used motor, is a total of 24 locations per rotation. As the magnetic lead screw has a pitch of 22mm per rotation, this gives slightly less than 1 mm in rotor/MLS location resolution which makes exact knowledge of the applied force challenging. Additionally, the magnetic lead screw has no position measurement built in which further complicates a control implementation.

1.4 Problem Formulation

The purpose of the following chapters is, based on the previously described system hardware and the expected challenges, to construct a control system for the mechanical system as to control the position and speed of the linear actuator. The development of the controllers is based on the question: *How effectively can a magnetically driven lead screw be controlled in a way that maintains position accuracy while prioritizing speed in conditions where a load and/or disturbances are present?*

1.4.1 Requirements

- Modeling of the magnetic lead screw and permanent magnet motor
- Analysis of the system to be controlled

- Testing of control schemes on an unloaded application
- Evaluation of control schemes
- Investigation of discretization effects on control

1.5 Thesis Methodology

In the following section, the approach used for the thesis is described, consisting of the following elements.

- Development of a system model
- Validation of the model behavior
- Development of controllers
- Evaluation of the controllers
- Investigation of limited sensor feedback
- Comparison of controllers
- Conclusions

The listed items will be briefly described.

1.5.1 System Model Development

In order to test and develop the controllers, a nonlinear model and a linear model are developed. The nonlinear model is primarily used for the testing of the system behavior with the controllers whereas the linear model is used for analyzing the system behavior and developing linear controllers.

1.5.2 Validation of the System Model

In order to validate the behavior of the nonlinear model, the behavior will be compared to the expected behavior of the test setup and the unknown parameters tuned to minimize the discrepancies. The linear model is then compared to the nonlinear in order to validate the local behavior and to evaluate which operating areas cause differing behavior.

1.5.3 Controller Development

Controllers are developed based initially on the linear model and evaluated based on their performance. Additional controllers are chosen and tested based on the areas where the evaluation finds the control method lacking. This may include both linear control methods and nonlinear.

1.5.4 Evaluation of Controllers

The controller performances are evaluated against each other based on their performance when applied to the nonlinear system model. A set of criteria is defined in order to assist in the quantitative evaluation of the controllers.

1.5.5 Investigation of Limited Sensor Feedback

As the system does not include sensors on every state, the necessity of additional sensors for effective control is investigated through testing of various simulated measurement configurations.

1.6 Evaluation Criteria

The control systems are evaluated based on the following criteria:

- Maximum Speed
- Sensor Requirements

1.6.1 Maximum Speed Capability

The prime evaluation criteria is the maximum point to point speed capability of the system which is evaluated based on the time taken to travel to and settle at a point without slipping.

1.6.2 Maximum Speed Capability

The secondary evaluation criteria is the peak overshoot or subsequent oscillation undershoot present in the controller settling dynamics.

1.6.3 Sensor Requirements

Each control method will be tested with various state feedback setups including the limited hall effect sensor feedback in the current test system, a configuration with inductive sensors on the magnetic lead screw translator, and two with resolvers on the translator with varied measurement resolutions. For each case, the necessity of the additional sensors will be evaluated with respect to the control performance.

Dynamic Model of RMLS Prototype 2

In order to simulate the system and to do further analysis, a nonlinear model must be created based on the known behavior of the system components.

Henceforth dot notation will be used to describe the derivative with respect to time ($\dot{x} = \frac{dx}{dt}$). The second derivative with respect to time will similarly be denoted with two dots.

2.1 Mechanical System Model

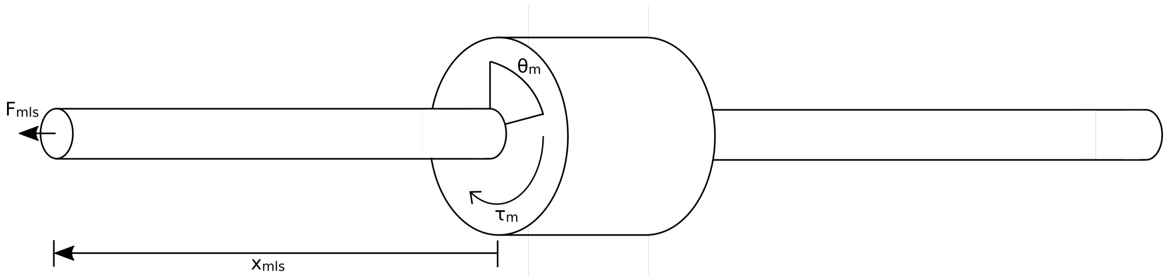

Figure 2.1: Food Grade RMLS Prototype

The mechanical portion of the system consists purely of the lead screw, the nut and rotor, and any attached load to the system. The mechanical system includes frictional losses which are represented by static and viscous friction. The equations of motion for the lead screw are thus:

$$\ddot{x}_{mls} = \frac{F_{mls} - B_{vs}\dot{x}_{mls} - F_{ss}sgn(\dot{x}_{mls})}{M} \tag{2.1}$$

x_{mls}	Rod position [m]
B_{vs}	MLS viscous friction [$\frac{N}{mm/s}$]
F_{ss}	MLS constant friction [N]
M	Rod Mass[kg]

Where the force from the magnetic lead screw is defined by the MLS characteristics, the rotor position, and the MLS position as:

$$F_{mls} = F_{stall} \cdot sin\left(\frac{2\pi}{\frac{\gamma}{n_{thread}}} \cdot \left(x_{mls} - \frac{\theta_m \cdot \gamma}{2\pi}\right)\right) \tag{2.2}$$

F_{stall}	MLS stall force [N]
γ	MLS pitch [$\frac{m}{rad}$]
n_{thread}	Number of MLS threads [N]
θ_m	Rotor position [rad]

Plotting the MLS force across one period of the lead screw shows the curve of the force as the slip varies. For slip values within 5.5mm of zero, the MLS is considered to be within the stable region as the local spring constant is positive. As the MLS passes this region, the spring constant becomes negative and though the force is still acting in the positive direction, the force does not increase further as a larger input is given and thus it is considered an unstable region.

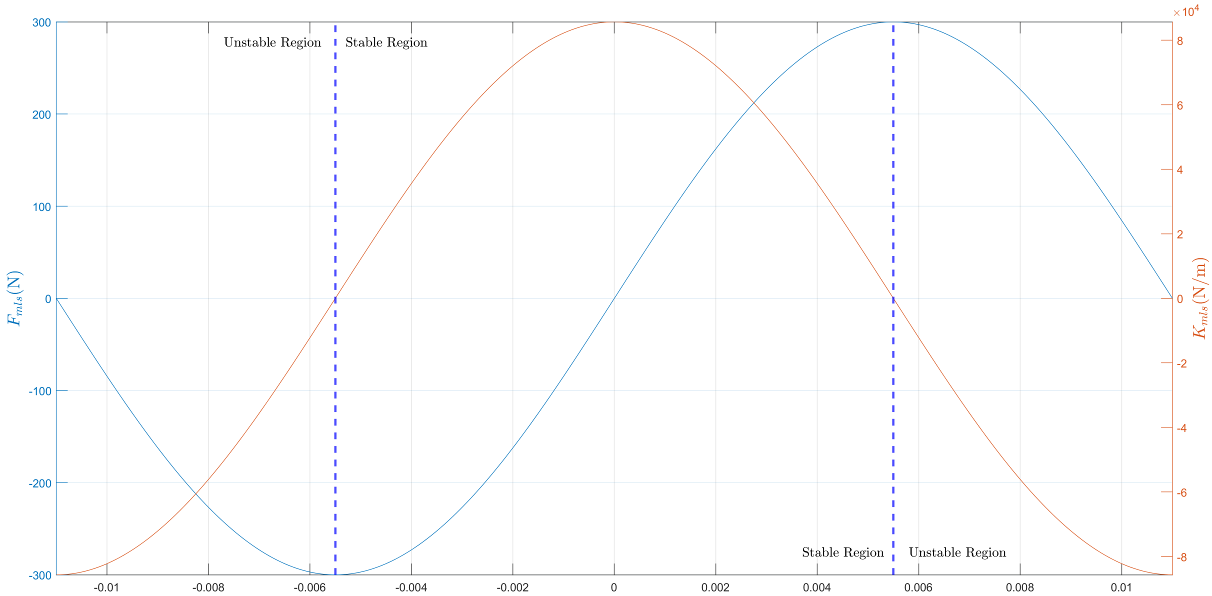

Figure 2.2: MLS force curve and local spring constant across one period of the lead screw.

The dynamic equation for the rotor position is thus defined based on the motor torque, force applied by the magnetic lead screw, and friction as:

$$\ddot{\theta}_r = \frac{\tau_m - \frac{\gamma F_{mls}}{2\pi} - B_{vr}\dot{\theta}_r - F_{sr} sgn(\dot{\theta}_m)}{J} \tag{2.3}$$

τ_m	Motor torque [Nm]
B_{vr}	Rotor viscous friction [$\frac{N}{mm/s}$]
F_{sr}	Rotor constant friction [N]
J	Rotor inertial moment [$\frac{kg}{m}$]

2.2 PMSM Model

A star connected PMSM can be represented as the circuit in figure 2.3 with resistances, inductances, and magnetically induced voltages for each phase.

2.2.1 ABC Reference Frame

The voltage equation for the circuit in figure 2.3 can be written with the inclusion of mutual inductances as:

$$\begin{bmatrix} v_a \\ v_b \\ v_c \end{bmatrix} = \begin{bmatrix} R & 0 & 0 \\ 0 & R & 0 \\ 0 & 0 & R \end{bmatrix} \begin{bmatrix} i_a \\ i_b \\ i_c \end{bmatrix} + p \begin{bmatrix} L_a & L_{ba} & L_{ca} \\ L_{ba} & L_b & L_{cb} \\ L_{ca} & L_{cb} & L_c \end{bmatrix} \begin{bmatrix} i_a \\ i_b \\ i_c \end{bmatrix} + \begin{bmatrix} e_a \\ e_b \\ e_c \end{bmatrix} \tag{2.4}$$

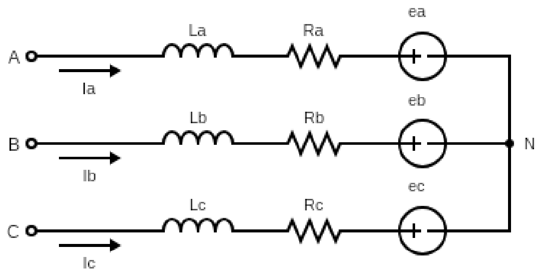

Figure 2.3: Basic circuit of a PMSM neglecting mutual inductances.

$v_{a/b/c}$	Phase input voltage [V]
$i_{a/b/c}$	Phase current [A]
R	Coil resistance [Ω]
$L_{a/b/c}$	Phase coil inductance [H]
$L_{ba/ca/cb}$	Coil mutual inductance [H]
$e_{a/b/c}$	Phase back-emf
p	number of poles

Assuming that the motor is manufactured symmetrically, the inductance of each phase and the mutual inductances between phases will be identical and thus:

$$L_a = L_b = L_c = L \tag{2.5}$$

$$L_{ab} = L_{ca} = L_{bc} = L_m \tag{2.6}$$

$$\begin{bmatrix} v_a \\ v_b \\ v_c \end{bmatrix} = \begin{bmatrix} R & 0 & 0 \\ 0 & R & 0 \\ 0 & 0 & R \end{bmatrix} \begin{bmatrix} i_a \\ i_b \\ i_c \end{bmatrix} + p \begin{bmatrix} L & L_m & L_m \\ L_m & L & L_m \\ L_m & L_m & L \end{bmatrix} \begin{bmatrix} i_a \\ i_b \\ i_c \end{bmatrix} + \begin{bmatrix} e_a \\ e_b \\ e_c \end{bmatrix} \tag{2.7}$$

L	Phase inductance
L_m	Mutual inductance

Following with Kirchoffs law, the sum of currents through a junction equals zero, which in the case of a star-connected machine can be used to state:

$$i_a + i_b + i_c = 0 \tag{2.8}$$

$$L_m i_a + L_m i_c = L_m i_b \tag{2.9}$$

From this and the previous assumption, the inductance matrix can be further be simplified to:

$$\begin{bmatrix} v_a \\ v_b \\ v_c \end{bmatrix} = \begin{bmatrix} R & 0 & 0 \\ 0 & R & 0 \\ 0 & 0 & R \end{bmatrix} \begin{bmatrix} i_a \\ i_b \\ i_c \end{bmatrix} + p \begin{bmatrix} L - L_m & 0 & 0 \\ 0 & L - L_m & 0 \\ 0 & 0 & L - L_m \end{bmatrix} \begin{bmatrix} i_a \\ i_b \\ i_c \end{bmatrix} + \begin{bmatrix} e_a \\ e_b \\ e_c \end{bmatrix} \tag{2.10}$$

The back emf assuming a quasi-sinusoidal magnetic flux is given by:

$$e_{pm} = \frac{d\psi_{pm_k}}{dt} = \lambda_{pm} \frac{d\gamma_k}{dt} \tag{2.11}$$

Adapting the above to include the three phases, the back emf is given as:

$$\gamma_{abc} = \begin{bmatrix} sin(\theta) \\ sin(\theta - \frac{2\pi}{3}) \\ sin(\theta - \frac{4\pi}{3}) \end{bmatrix} \tag{2.12}$$

$$e_{pm} = e_{ABC} = \lambda_{pm} \begin{bmatrix} \omega sin(\theta) \\ \omega sin(\theta - \frac{2\pi}{3}) \\ \omega sin(\theta - \frac{4\pi}{3}) \end{bmatrix} \tag{2.13}$$

The electrical torque can then be calculated based on electrical power from:

$$\tau_e = \frac{e_a i_a + e_b i_b + e_c i_c}{\omega_r} \tag{2.14}$$

2.2.2 Alpha-Beta Coordinate frame

The three phases of the above motor model can be represented by a stator fixed space vector $k_{\alpha\beta}$ which can be used to represent all of the phase quantities of voltage, current, and flux linkage in a two dimensional vector.[10]

The complex vector $k_{\alpha\beta}$ can be derived from athree phase ABC vector through the relation:

$$k_{\alpha\beta} = \frac{2}{3}\left[k_A + a k_B + a^2 k_C\right] \tag{2.15}$$

Where:

$$a = e^{j\frac{2\pi}{3}} \tag{2.16}$$

$$a^2 = e^{j\frac{4\pi}{3}} \tag{2.17}$$

Isolating equation 2.15 into real and complex portions gives:

$$k_{\alpha\beta} = \frac{2}{3}\left[k_A + \left(-\frac{1}{2} + j\frac{\sqrt{3}}{2}\right)k_B + \left(-\frac{1}{2} - j\frac{\sqrt{3}}{2}\right)k_C\right] \tag{2.18}$$

$$Re(k_{\alpha\beta}) = k_\alpha = \frac{2}{3}k_A - \frac{1}{3}k_B - \frac{1}{3}k_C \tag{2.19}$$

$$Im(k_{\alpha\beta}) = k_\beta = \frac{1}{\sqrt{3}}k_B - \frac{1}{\sqrt{3}}k_C \tag{2.20}$$

Which can be further formalized into the Clarke transformation matrix as:

$$\begin{bmatrix} k_\alpha \\ k_\beta \end{bmatrix} = \begin{bmatrix} \frac{2}{3} & -\frac{1}{3} & -\frac{1}{3} \\ 0 & \frac{1}{\sqrt{3}} & -\frac{1}{\sqrt{3}} \end{bmatrix} \begin{bmatrix} k_A \\ k_B \\ k_C \end{bmatrix} \tag{2.21}$$

Applying the Clark transformation allows the voltage equation in equation 2.2.1 to be represented as:

$$u_{\alpha\beta} = R i_{\alpha\beta} + (L_{ABC} - L_M)\frac{di_{\alpha\beta}}{dt} + \lambda_{pm} j\omega_e e^{j\omega_e} \tag{2.22}$$

Defining the flux vector as:

$$\psi_{\alpha\beta} = (L_{ABC} - L_M) i_{\alpha\beta} + \lambda_{pm} j\omega_e e^{j\omega_e} \tag{2.23}$$

Allows for equation 2.22 to be reduced to:

$$u_{\alpha\beta} = R \cdot i_{\alpha\beta} + \frac{d\psi_{\alpha\beta}}{dt} \tag{2.24}$$

2.2.3 dq Coordinate Frame

The α, β reference frame can be further converted into the fixed rotor or d, q reference frame through the relation:

$$\theta_{dq} = \theta_{\alpha\beta} - \theta_e \tag{2.25}$$

Which represents the rotation of the d, q coordinate frame in the α, β space with the electric angular velocity of the motor [11]. From this, the vector k_{dq} can be defined as:

$$k_{dq} = k_d + jk_q = ke^{j\theta_{dq}} \tag{2.26}$$
$$= ke^{j(\theta_{\alpha\beta} - \theta_e)} = ke^{j\theta_{\alpha\beta}}e^{-j\theta_e} \tag{2.27}$$

The α, β vector can be similarly defined as:

$$k_{\alpha\beta} = k_\alpha + jk_\beta = ke^{j\theta_{\alpha\beta}} \tag{2.28}$$
$$= ke^{j(\theta_{dq} + \theta_e)} = ke^{j\theta_{dq}}e^{j\theta_e} \tag{2.29}$$

From these, the Park transformation is defined as:

$$k_{dq} = k_{\alpha\beta}e^{-j\theta_e} \tag{2.30}$$

Applying the park transform to the α, β voltage equation in equation 2.24, the d, q voltage equation may be written as:

$$u_{dq} = Ri_{dq} + L\frac{di_{dq}}{dt} + j\omega_e(Li_{dq} + \lambda_{pm}) \tag{2.31}$$

Which can be split into the real and complex components:

$$u_d = Re(u_{dq}) = Ri_d + L\frac{di_d}{dt} + \omega_e Li_q \tag{2.32}$$
$$u_q = Im(u_{dq}) = Ri_q + L\frac{di_q}{dt} + \omega_e(Li_d + \lambda_{pm}) \tag{2.33}$$

The electromechanical power output by the motor can then be described by:

$$P_{em} = \frac{3}{2}(\omega_e \lambda_{pm} i_q) \tag{2.34}$$

Which, with the mechanical angular velocity, dependant on the number of poles, p, can be used to define the electromagnetic torque.

$$\omega_m = \frac{2}{p}\omega_e \tag{2.35}$$
$$\tau_e = \frac{P_{em}}{\omega_m} = \frac{P_{em}}{\frac{2}{p}\omega_e} = \frac{3p}{4}\lambda_{pm} i_q \tag{2.36}$$

Using equation 2.35 to convert the electrical angular velocity to the mechanical rotor angular velocity gives the voltage equations:

$$u_d = Re(u_{dq}) = Ri_d + L\frac{di_d}{dt} + \frac{p}{2}\omega_r Li_q \tag{2.37}$$
$$u_q = Im(u_{dq}) = Ri_q + L\frac{di_q}{dt} + \frac{p}{2}\omega_r(Li_d + \lambda_{pm}) \tag{2.38}$$

2.3 Full System Model

The full system model can be represented, using the above equations, as the derivatives of some state vector $\boldsymbol{x}$. In this case, $\boldsymbol{x}$ is defined as:

$$\boldsymbol{x} = \begin{bmatrix} i_d & i_q & \theta_r & \dot{\theta}_r & x & \dot{x} \end{bmatrix}^T \tag{2.39}$$

The derivatives of these states can be written as:

$$\dot{i}_d = \frac{1}{L}\left(u_d - Ri_d - \frac{p}{2}\dot{\theta}_m L i_q\right) \tag{2.40}$$

$$\dot{i}_q = \frac{1}{L}\left(u_q - Ri_q - \frac{p}{2}\dot{\theta}_m (L i_d + \lambda_{pm})\right) \tag{2.41}$$

$$\ddot{\theta}_m = \frac{1}{J}\left(\frac{3p}{4}\lambda_{pm} i_q - \frac{\gamma}{2\pi}F_{stall} \cdot sin\left(\frac{2\pi}{\frac{\gamma}{n_{thread}}} \cdot \left(x_{mls} - \frac{\gamma\theta_m}{2\pi}\right)\right) - \dot{\theta}_m B_{vr} - F_{sr} sgn(\dot{\theta}_m)\right) \tag{2.42}$$

$$\ddot{x} = \frac{1}{M}\left(F_{stall} \cdot sin\left(\frac{2\pi}{\frac{\gamma}{n_{thread}}} \cdot \left(x_{mls} - \frac{\gamma\theta_m}{2\pi}\right)\right) - B_{vs}\dot{x}_{mls} - F_{ss} sgn(\dot{x}_{mls})\right) \tag{2.43}$$

2.4 Direct Drive System Model

In order to evaluate the system independent of the significant nonlinearity present in the magnetic interface between the lead screw and rotor, a reduced model is created where the magnetic lead screw is replaced with a linear spring with the same spring constant as the MLS with zero displacement.

3 Parameter Identification and Model Validation

The final step of building the model is identification of the parameters that are not specified in either the information given about the motor or magnetic lead screw, and the validation of the system behavior with the assumed parameters and the developed model.

3.1 Parameter Identification

Of the parameters necessary for modeling the system, the ones that are not strictly defined are:

λ_{pm}	Motor permanent magnet flux linkage
R	Coil resistance
L	Coil inductance
B_{vs}	MLS viscous friction

3.1.1 Motor Back-emf Constant

The permanent magnet flux linkage is measured from the motor by sliding the translator at a constant velocity and measuring the amplitude and frequency of the resultant voltage waveform. This is measured through the use of an oscilloscope connected between two of the three phases of the motor.

Using the test data in figure 3.1, a linear model was fit to give the relation between measured voltage and electrical frequency.

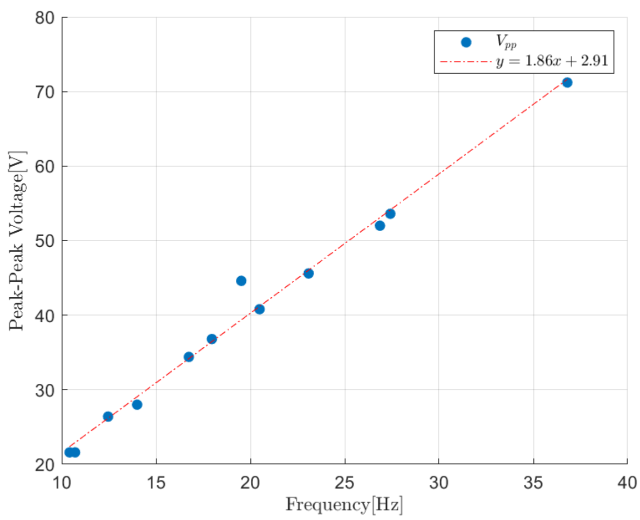

Figure 3.1: Peak to peak voltage and frequency measured when hand-driving the RLMS.

As the voltage is measured across two phases, the voltage across a single phase has to be isolated as well as the frequency adjusted for the multiple poles in the motor.

$$\lambda_{pm} = \frac{V_{pp}}{2p\sqrt{3}\omega_m} \tag{3.1}$$

From this equation, the back-emf constant can be found as $0.0214\frac{V\cdot s}{rad}$.

To further validate this value and the torque behavior of the motor, the motor was powered in various constant current states and the translator moved until the rotor was forced to slip. for the zero current test, the motor was tested with both an open circuit and the closed circuit where the power supply is connected to the motor. In order to measure the force at which the slipping occurred, a strain gauge was used and the peak value chosen.

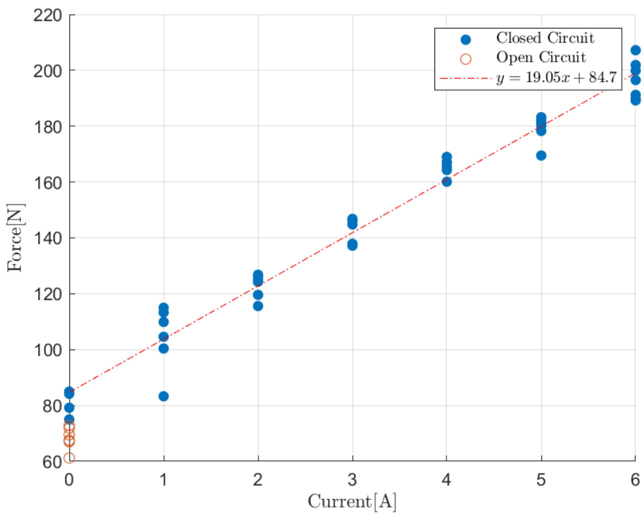

Figure 3.2: Measured force versus applied current when hand-driving the RMLs.

It can be seen that when the circuit is open (unconnected) versus when the circuit is closed (connected) there is a difference in forces when the test is run. This is due to the small back-emf generated by moving the rotor and the related induced current. When the circuit is open, this current is not present.

The open circuit tests reveal that there is roughly $68N$ in static friction in the system and when the circuit is closed, roughly $15N$ is produced by the electrical resistance.

From the rest of the closed circuit load tests, a relationship between the current and the stall torque may be determined as a linear relationship which can then be used to again derive the back-emf constant.

$$\tau_m = \frac{\gamma}{2\pi} F_{mls} \tag{3.2}$$

$$\lambda_{pm} = \frac{\tau_m}{\frac{3p}{4} i_q} \tag{3.3}$$

From this, the back-emf constant is found to be $0.0222\frac{V\cdot s}{rad}$. which is very similar to the value found previously.

3.1.2 Motor Coil Resistance

The motor coil resistance is measured with a HP 4284A LCR meter across each pair of phases in order to identify the values of each phase.

The resistances are found to be:

R_{ab}	0.775Ω
R_{bc}	0.735Ω
R_{ca}	0.847Ω

As each measurement is across two phases, the per-phase resistance is half of the measured value which in this case gives an average phase resistance of 0.392Ω.

3.1.3 Motor Coil Inductance

The motor coil inductance is measured with the same HP 4284A LCR meter across each pair of phases in the same configuration as for the resistance.

The inductances are found to be:

I_{ab}	$33.29\mu H$
I_{bc}	$29.50\mu H$
I_{ca}	$30.29\mu H$

Again as each measurement is across two phases, the per-phase inductance is half of the measured value which gives an average phase inductance of $15.51\mu H$.

3.1.4 MLS Static Friction

From the torque testing, the minimum amount of force required to mechanically move the MLS was identified. Using this knowledge, the static friction in the system may be determined.

$$F_s = F_{ss} + \frac{\gamma}{2\pi} F_{sr} \tag{3.4}$$

Using this and the rotor static friction value from a similar machine in previous works[6], the MLS translator static friction is found to be approximately $50.8N$.

3.2 Model Validation

In order to validate the behavior of the nonlinear model, a zero-slip and a nonlinear model for the magnetic lead screw system are built up in Matlab Simulink and tested with identical inputs.

3.2.1 Basic Behavior Validation

In this test of the nonlinear model, a voltage step input is given to the magnetic lead screw and the zero-slip models in order to gauge the differences in response caused by the nonlinear behavior.

The step input magnitude is chosen here as 10v in order to avoid a slip failure of the MLS while still being large enough to cause the system dynamics to become noticeably excited.

The d and q axis currents can be seen to have some minor coupling as the d axis current drops in relation to the q axis current increasing. It can additionally be seen that the current spikes while the motor has not yet reached the maximum speed and gradually reduces down until equilibrium.

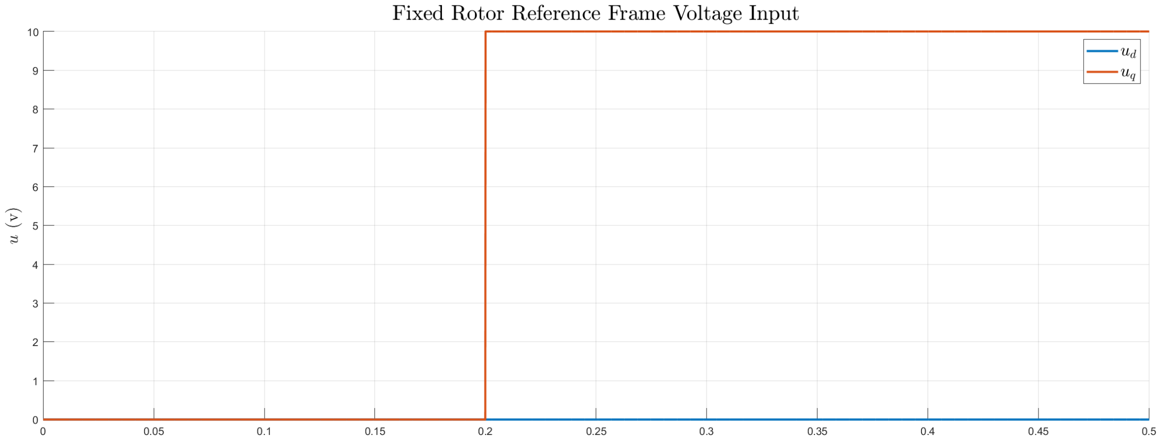

Figure 3.3: q axis voltage step input

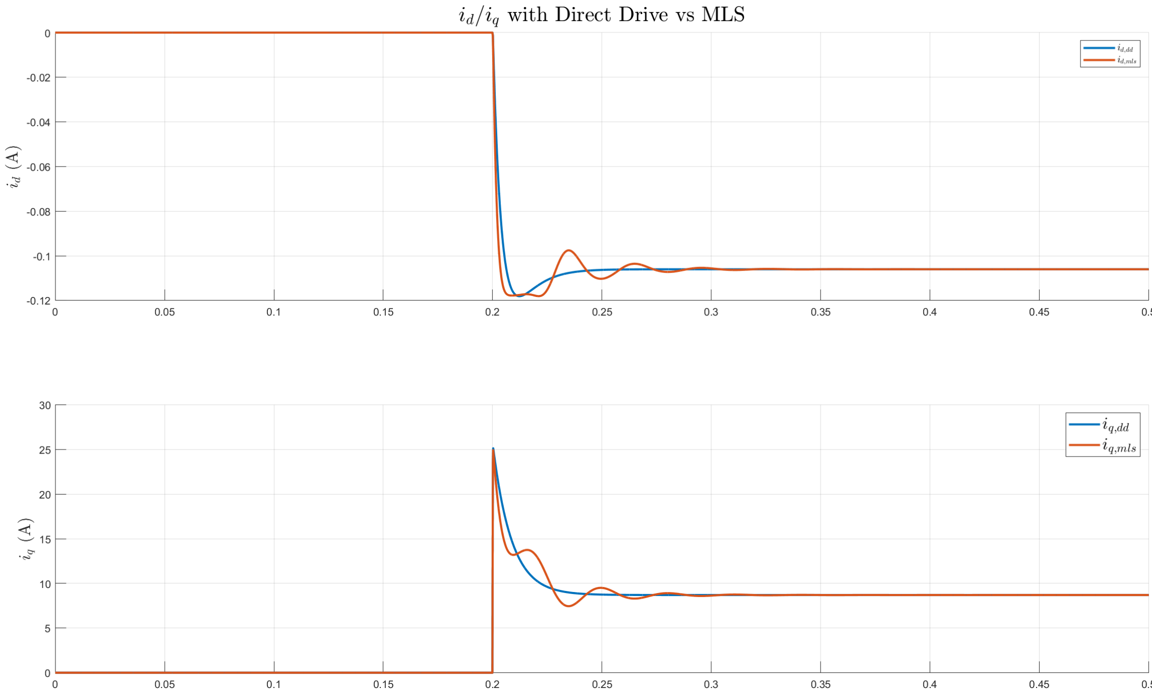

Figure 3.4: Current Response to a 10v q axis step.

The current is additionally affected by the oscillating velocity of the rotor due to the nonlinear behavior of the MLS and thus the back-emf causes it to oscillate.

The rotor position is seen to behave as expected where it increases in velocity until the equilibrium point. The zero-slip model and the MLS model follow nearly the same trajectory with the difference being the oscillations created by the interactions between the MLS and the rotor. The oscillations are strongly tied to the inertial moment of the rotor and MLS in terms of frequency and magnitude.

The x_{mls} dynamics behave similarly to the rotor, however the amplitude of the oscillation is lower due to the larger mass of the MLS.

The oscillation causing the difference in behavior between the two models comes from the interaction between the rotor dynamics, lead screw dynamics, and the nonlinearity of the MLS coupling. Here it can be seen that the force applied by the magnetic lead screw jumps up significantly along with the step input and gradually settles as the rotor reaches the maximum speed and thus the required MLS acceleration, and torque, is reduced.

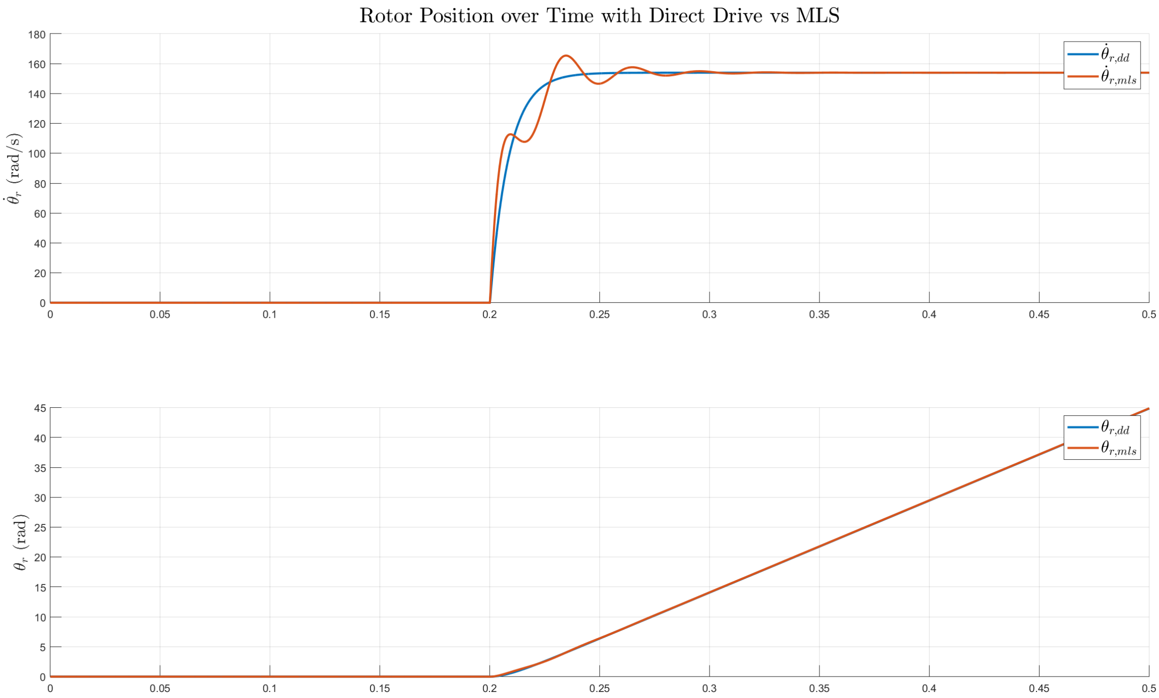

Figure 3.5: Rotor response to a 10v q axis step.

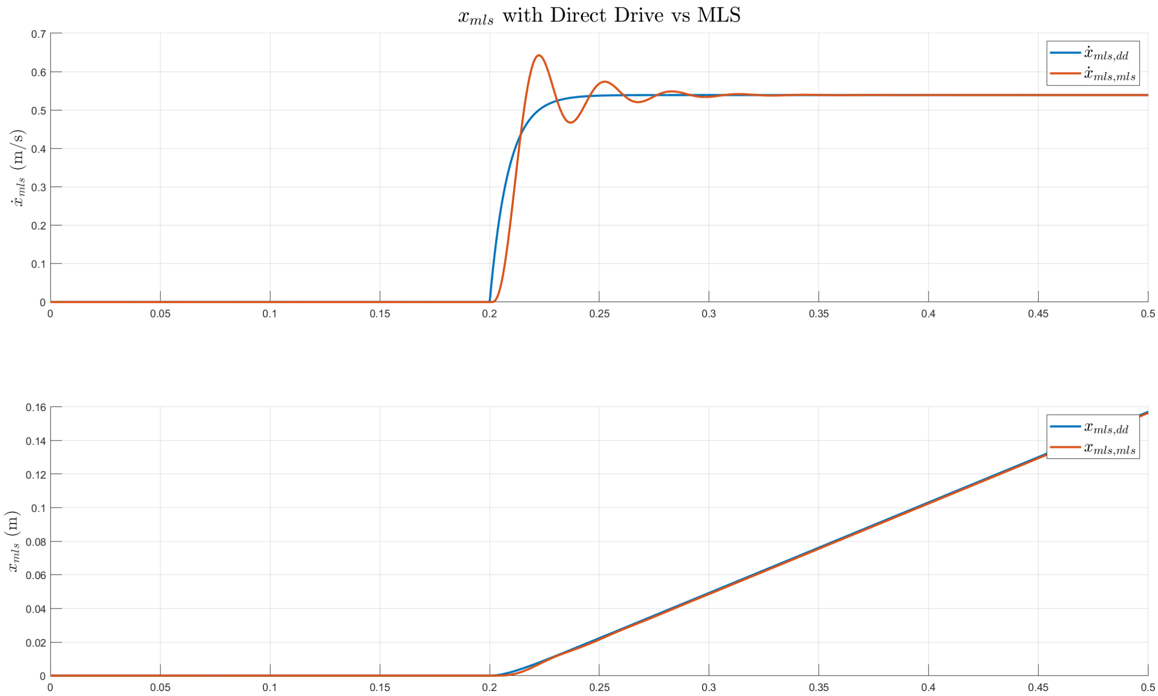

Figure 3.6: Translator response to a 10v q axis step.

In the case where a ramp or filtered input are given, the oscillations are significantly reduced though the acceleration to the maximum speed is additionally reduced.

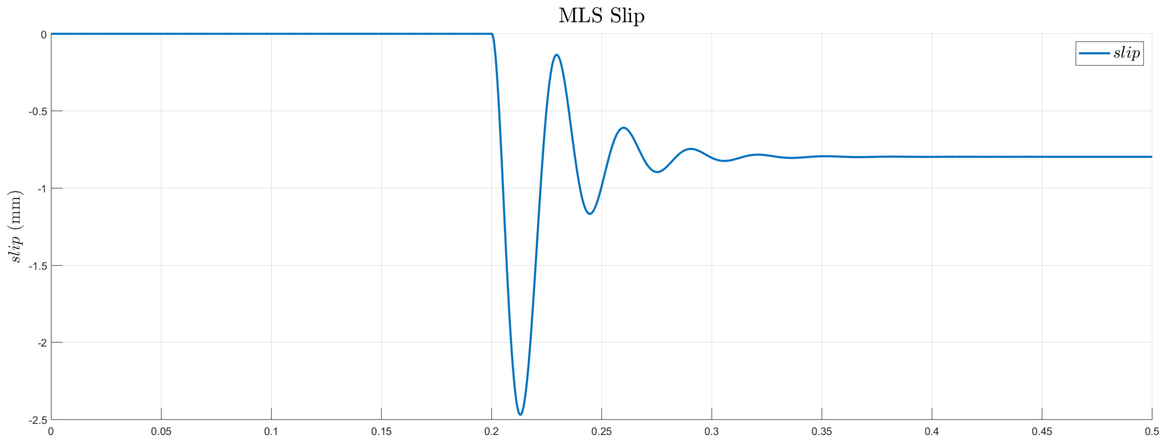

Figure 3.7: Slip response to a 10v q axis step.

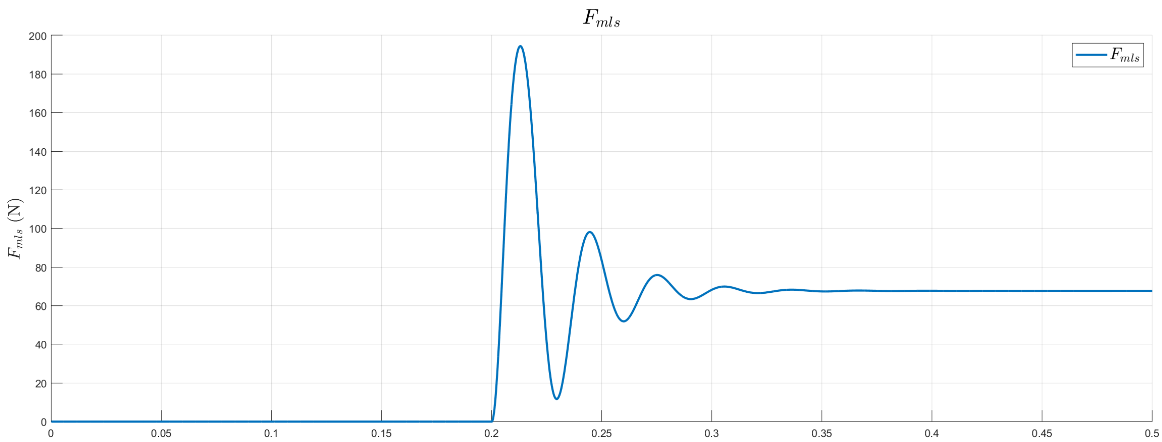

Figure 3.8: MLS force response to a 10v q axis step.

3.2.2 Slip Fault Behavior

When a larger input is given, the slip fault behavior may be observed. Here, a 48v step input is given which very effectively causes the MLS to slip out of the stable region.

In the slip fault condition, the rotor in the MLS model settles at a higher velocity than the zero-slip model as the damping present in the linear motion is no longer transmitted to the rotor. The rotor can be seen to oscillate as it passes over each period of the MLS.

The MLS can be seen to initially follow the rotor, however, once the force applied exceeds 300N corresponding to a slip of 6mm, the MLS velocity oscillates around zero.

As can be expected in this condition, the slip continually increases and the resultant sinusoidal force coupling causes the oscillations seen in figure 3.9 and figure 3.10.

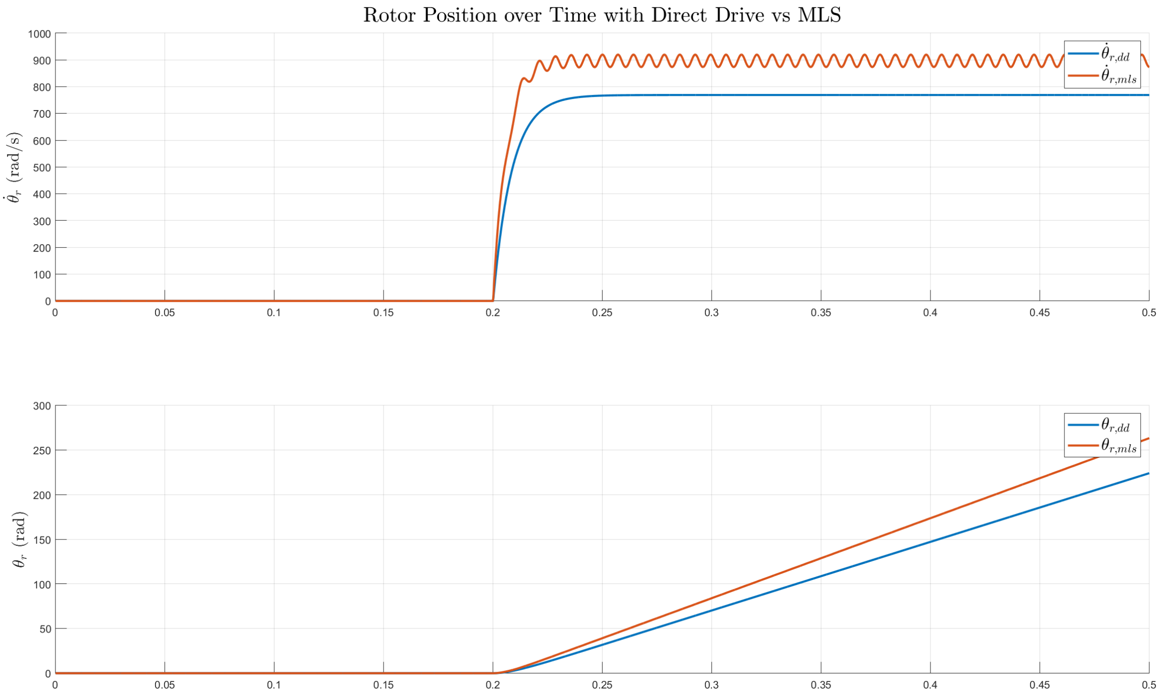

Figure 3.9: Rotor behavior when a slip fault occurs in the nonlinear model versus the zero-slip model.

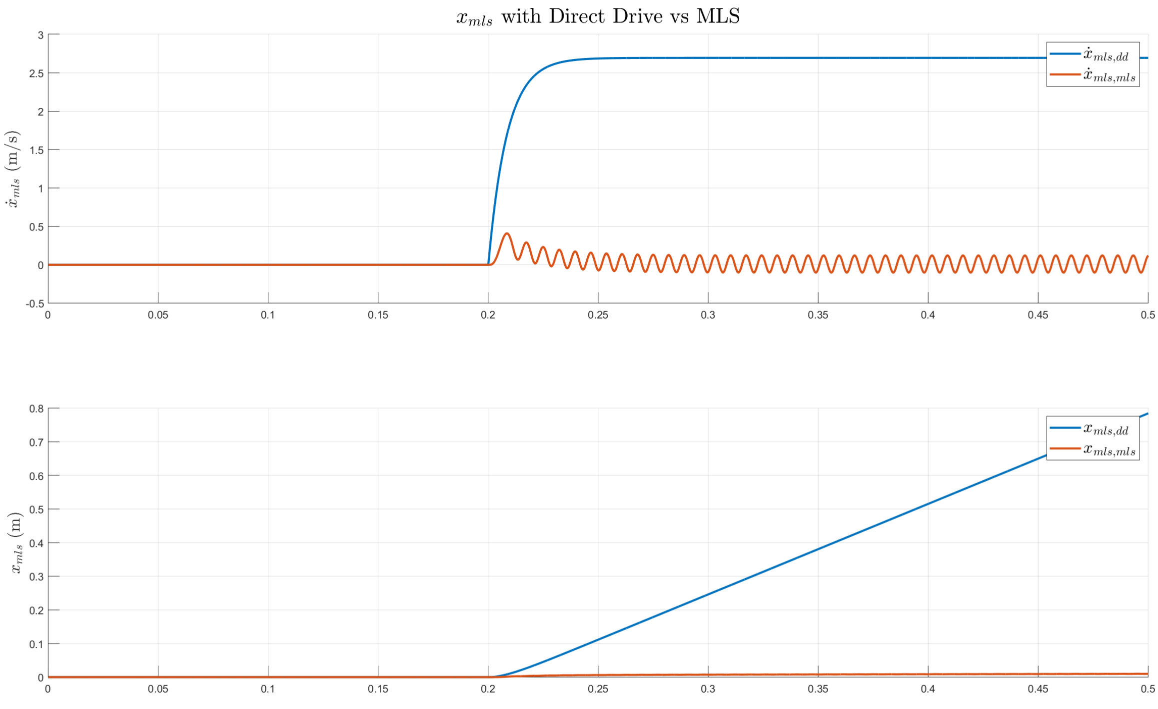

Figure 3.10: Translator behavior when a slip fault occurs in the nonlinear model versus the zero-slip model.

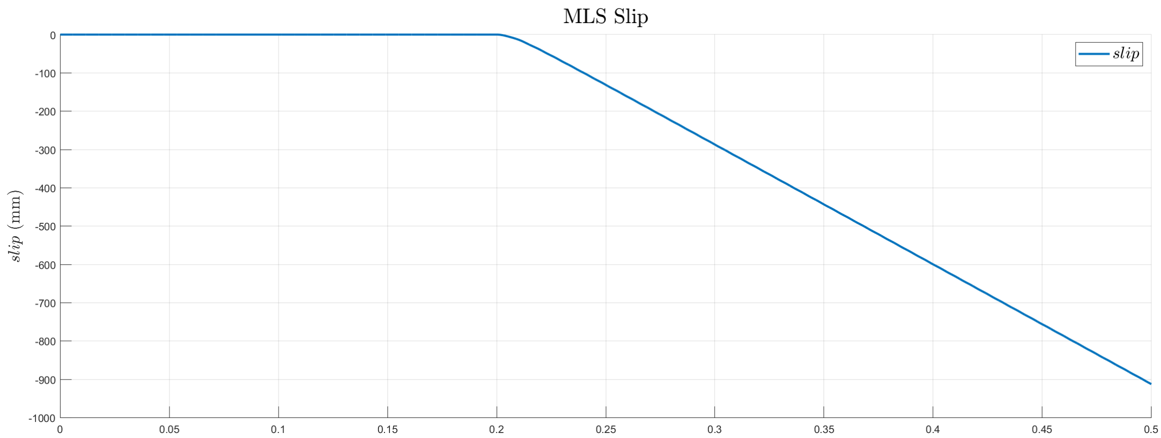

Figure 3.11: MLS slip under slip fault conditions.

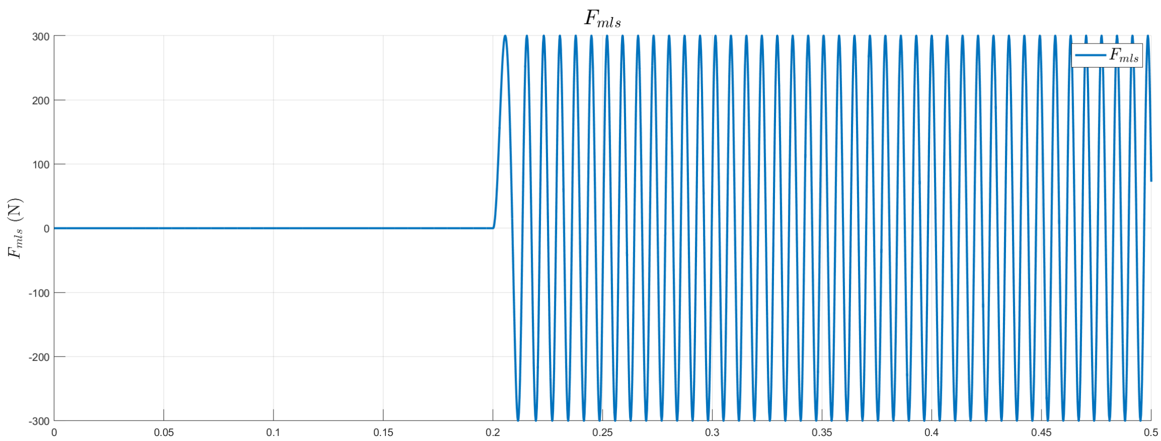

Figure 3.12: MLS force under slip fault conditions.

3.2.3 Torque Validation

In order to validate the torque behavior of the motor, PID controllers are tuned by hand for the d and q axis currents. The d axis current is given a reference of 0A while the q axis current is given a step reference of 30A corresponding with the rated current of the motor.

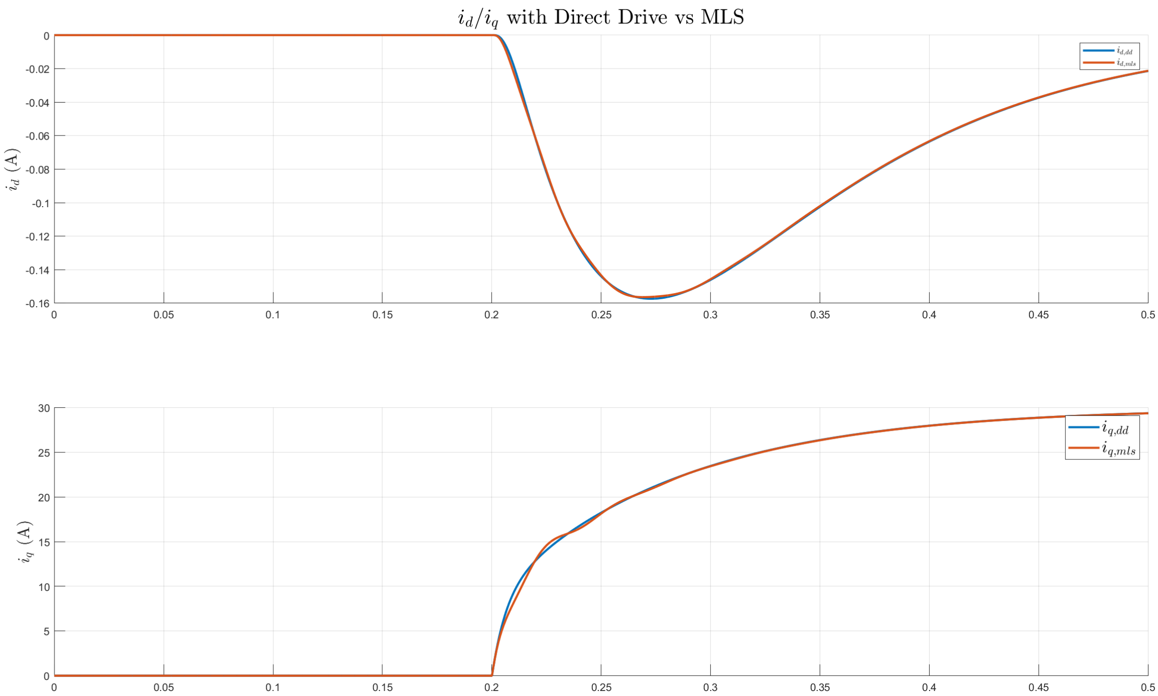

Figure 3.13: Direct and quadrature axis currents in nonlinear versus zero-slip models

The controller is not optimised for speed and aims to avoid a slip fault while achieving zero current error in the steady state.

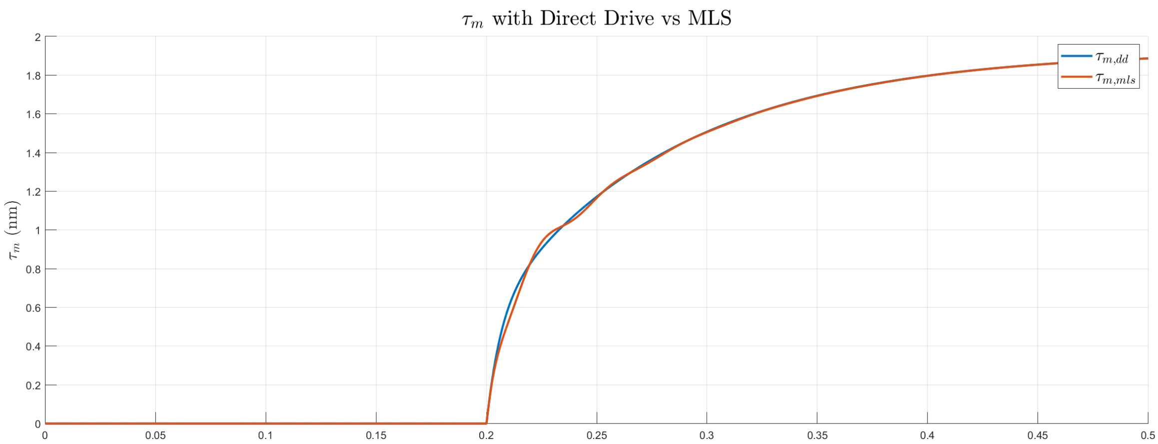

Figure 3.14: Motor torque in nonlinear versus zero-slip models.

It can be seen that the motor torque reaches $2Nm$ when the current is at the rated current of 30A which validates the expected behavior as defined in the motor specifications.

Part II

System Controller Design

Linear Model 4

In order to analyze the system, the previously developed model is reduced to a linear model based on the d, q fixed rotor reference frame.

$$\dot{i}_d = \frac{1}{L}\left(u_d - Ri_d - \frac{p}{2}\omega_r L i_q\right) \tag{4.1}$$

$$\dot{i}_q = \frac{1}{L}\left(u_q - Ri_q - \frac{p}{2}\omega_r (L i_d + \lambda_{pm})\right) \tag{4.2}$$

$$\ddot{\theta}_r = \frac{1}{J}\left(\frac{3p}{4}\lambda_{pm} i_q - \frac{1}{2\pi}\gamma F_{stall}\cdot sin\left(\frac{2\pi}{\frac{\gamma}{n_{thread}}}\cdot\left(x - \frac{\gamma\theta_r}{2\pi}\right)\right) - \dot{\theta}_r B_{vr}\right) \tag{4.3}$$

$$\ddot{x} = \frac{1}{M}\left(F_{stall}\cdot sin\left(\frac{2\pi}{\frac{\gamma}{n_{thread}}}\cdot\left(x - \frac{\gamma\theta_r}{2\pi}\right)\right) - B_{vs}\dot{x} - F_s sgn(\dot{x})\right) \tag{4.4}$$

4.1 Model Linearization

Through first order taylor series expansion, the system equations are linearized about the linearization points denoted by the subscript $_{,0}$.

$$\dot{i}_d = \underbrace{\frac{\partial \dot{i}_d}{\partial u_d}\bigg|_0}_{K_{1ud}}(u_d - u_{d,0}) + \underbrace{\frac{\partial \dot{i}_d}{\partial i_d}\bigg|_0}_{K_{1id}}(i_d - i_{d,0}) + \underbrace{\frac{\partial \dot{i}_d}{\partial i_q}\bigg|_0}_{K_{1iq}}(i_q - i_{q,0}) + \underbrace{\frac{\partial \dot{i}_d}{\partial \dot{\theta}_r}\bigg|_0}_{K_{1\dot{\theta}r}}(\dot{\theta}_r - \dot{\theta}_{r,0}) \tag{4.5}$$

$$\dot{i}_q = \underbrace{\frac{\partial \dot{i}_q}{\partial u_q}\bigg|_0}_{K_{2uq}}(u_q - u_{q,0}) + \underbrace{\frac{\partial \dot{i}_q}{\partial i_q}\bigg|_0}_{K_{2iq}}(i_q - i_{q,0}) + \underbrace{\frac{\partial \dot{i}_q}{\partial i_d}\bigg|_0}_{K_{2id}}(i_d - i_{d,0}) + \underbrace{\frac{\partial \dot{i}_q}{\partial \dot{\theta}_r}\bigg|_0}_{K_{2\dot{\theta}r}}(\dot{\theta}_r - \dot{\theta}_{r,0}) \tag{4.6}$$

$$\ddot{\theta}_r = \underbrace{\frac{\partial \ddot{\theta}_r}{\partial i_q}\bigg|_0}_{K_{3iq}}(i_q - i_{q,0}) + \underbrace{\frac{\partial \ddot{\theta}_r}{\partial \theta_r}\bigg|_0}_{K_{3\theta r}}(\theta_r - \theta_{r,0}) + \underbrace{\frac{\partial \ddot{\theta}_r}{\partial x}\bigg|_0}_{K_{3x}}(x - x_0) + \underbrace{\frac{\partial \ddot{\theta}_r}{\partial \dot{\theta}_r}\bigg|_0}_{K_{3\dot{\theta}r}}(\dot{\theta}_r - \dot{\theta}_{r,0}) \tag{4.7}$$

$$\ddot{x} = \underbrace{\frac{\partial \ddot{x}}{\partial \theta_r}\bigg|_0}_{K_{4\theta r}}(\theta_r - \theta_{r,0}) + \underbrace{\frac{\partial \ddot{x}}{\partial x}\bigg|_0}_{K_{4x}}(x - x_0) + \underbrace{\frac{\partial \ddot{x}}{\partial \dot{\theta}_r}\bigg|_0}_{K_{4\dot{\theta}r}}(\dot{\theta}_r - \dot{\theta}_{r,0}) \tag{4.8}$$

Within the given taylor series expansion, the linearization constants for the d axis current are:

$$k_{idud} = \frac{1}{L} \tag{4.9}$$
$$k_{idid} = -\frac{R}{L} \tag{4.10}$$
$$k_{idiq} = -\frac{p\,\dot{\theta}_{r,0}}{2} \tag{4.11}$$
$$k_{id\dot{\theta}_r} = -\frac{p\,i_{q,0}}{2} \tag{4.12}$$

The linearization constants for the q axis current are then:

$$k_{iquq} = \frac{1}{L} \tag{4.13}$$
$$k_{iqiq} = -\frac{R}{L} \tag{4.14}$$
$$k_{iqid} = -\frac{p\,\dot{\theta}_{r,0}}{2} \tag{4.15}$$
$$k_{iq}\dot{\theta}_m = -\frac{p\,(\lambda_{\mathrm{pm}} + L\,i_{\mathrm{d},0})}{2\,L} \tag{4.16}$$

The linearization constants for the rotor acceleration are:

$$k_{\theta_m iq} = \frac{3\,\lambda_{\mathrm{pm}}\,p}{4\,J} \tag{4.17}$$
$$k_{\theta_m\theta_m} = \frac{\mathrm{Fstall}\,\gamma\,n_{\mathrm{thread}}\,\cos\left(\frac{2\,\pi\,n_{\mathrm{thread}}\left(x_0 - \frac{\gamma\,\theta_{m,0}}{2\,\pi}\right)}{\gamma}\right)}{2\,J\,\pi} \tag{4.18}$$
$$k_{\theta_m\dot{\theta}_m} = -\frac{B_{\mathrm{vr}}}{J} \tag{4.19}$$
$$k_{\theta_m x} = -\frac{\mathrm{F}_{\mathrm{stall}}\,n_{\mathrm{thread}}\,\cos\left(\frac{2\,\pi\,n_{\mathrm{thread}}\left(x_0 - \frac{\gamma\,\theta_{m,0}}{2\,\pi}\right)}{\gamma}\right)}{J} \tag{4.20}$$

The linearization constants for the rod position are then:

$$k_{x\theta_m} = -\frac{F_{stall}\,\gamma\,n_{\mathrm{thread}}\,\cos\left(\frac{2\,\pi\,n_{\mathrm{thread}}\left(x_0 - \frac{\gamma\,\theta_{\mathrm{r}0}}{2\,\pi}\right)}{\gamma}\right)}{2\,M\,\pi} \tag{4.21}$$
$$k_{xx} = \frac{F_{stall}\,n_{\mathrm{thread}}\,\cos\left(\frac{2\,\pi\,n_{\mathrm{thread}}\left(x_0 - \frac{\gamma\,\theta_{\mathrm{r}0}}{2\,\pi}\right)}{\gamma}\right)}{M} \tag{4.22}$$
$$k_{x\dot{x}} = -\frac{B_{\mathrm{vs}}}{M} \tag{4.23}$$

4.2 State Space Model

In order to investigate the linear behavior in both single input single output (SISO) and multiple input multiple output (MIMO) cases, the linearized model is arranged into a state space model of the form:

$$\dot{x} = \boldsymbol{A}x + \boldsymbol{B}u \tag{4.24}$$
$$y = \boldsymbol{C}x + \boldsymbol{D}u \tag{4.25}$$

Within the state space model, the A and B matricies are defined as:

$$A = \begin{bmatrix} k_{idid} & k_{idiq} & 0 & k_{id\dot{\theta}_m} & 0 & 0 \\ k_{iqid} & k_{iqiq} & 0 & k_{iq\dot{\theta}_m} & 0 & 0 \\ 0 & 0 & 0 & 1 & 0 & 0 \\ 0 & k_{\theta_m iq} & k_{\theta_m \theta_m} & k_{\theta_m \dot{\theta}_m} & k_{\theta_m x} & 0 \\ 0 & 0 & 0 & 0 & 0 & 1 \\ 0 & 0 & k_{x\theta_m} & 0 & k_{xx} & k_{x\dot{x}} \end{bmatrix} \quad B = \begin{bmatrix} k_{idud} & 0 \\ 0 & k_{iquq} \\ 0 & 0 \\ 0 & 0 \\ 0 & 0 \\ 0 & 0 \end{bmatrix} \tag{4.26}$$

The state feedback matrix C will be defined as a 6x6 identity matrix for analysis, but will be later reduced in order to investigate the sensor requirements for controlling the system. There is no input to measurement coupling thus the D matrix is 0.

4.3 Selection of Linearization Points

The linearization points are selected based on the expected operation areas of the system and in order to maximize the more troublesome characteristics of the system.

The d axis current linearization point is selected at zero as it only causes resistive losses in the system and thus will be controlled to zero. The q axis current point is selected at 30A in order to maximize the coupling relation to the d axis current that may need to be compensated for in controllers if significant enough.

The x_{mls} and the θ_r position linearization points are selected as 0 and 0 such that the magnetic lead screw spring constant is in the central most linear region.

The linearization point for $\dot{x}_{mls}$ is selected at zero as well. The point selected for the rotor angular velocity is selected at $\frac{1}{4}$ of the maximum rotational speed of the motor as the machine is unlikely to operate at high speeds as often as lower, however as the current coupling is exacerbated by the rotation of the motor, a linearization point of 0 would be unsuitable.

4.4 Linear Model Validation

In order to validate the accuracy of the linear model versus the nonlinear models, the simulated systems are first given a small step input of 5volt which generates a current to surpass the static friction of the nonlinear models, a small step perturbation of 1 volt is given, and then a larger step of an additional 20 volts.

In order to compare the behavior independent of the static friction, which is not present in the linear model, the linear model response is offset to match the steady state condition after the initial input.

The q axis current response can be seen infigure 4.2 to be well represented by the linear approximation for small step inputs but deviates with larger steps, especially in the case of the MLS nonlinear model. The initial difference in current is due to the higher maximum velocity of the linear approximation and thus a higher back-emf and lower steady state current per input volt. The d axis current in this test was not approximated well due to the lack of a d axis input voltage and thus the behavior is much more sensitive to the multiplicative relation between rotor velocity and q axis current which the linear model cannot accurately reproduce. When an input is given however, the discrepancy becomes significantly smaller as the inputs tend to be significantly larger.

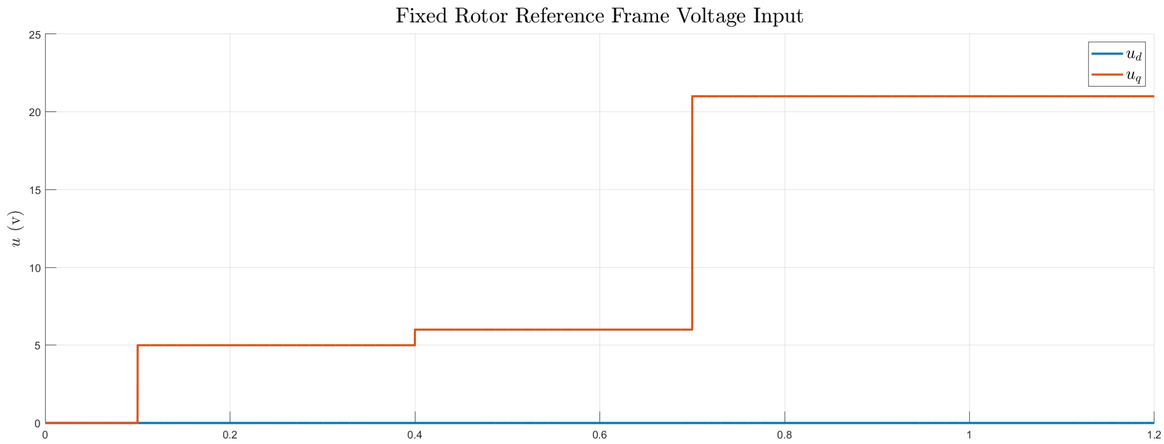

Figure 4.1: Voltage input trajectory used to validate models.

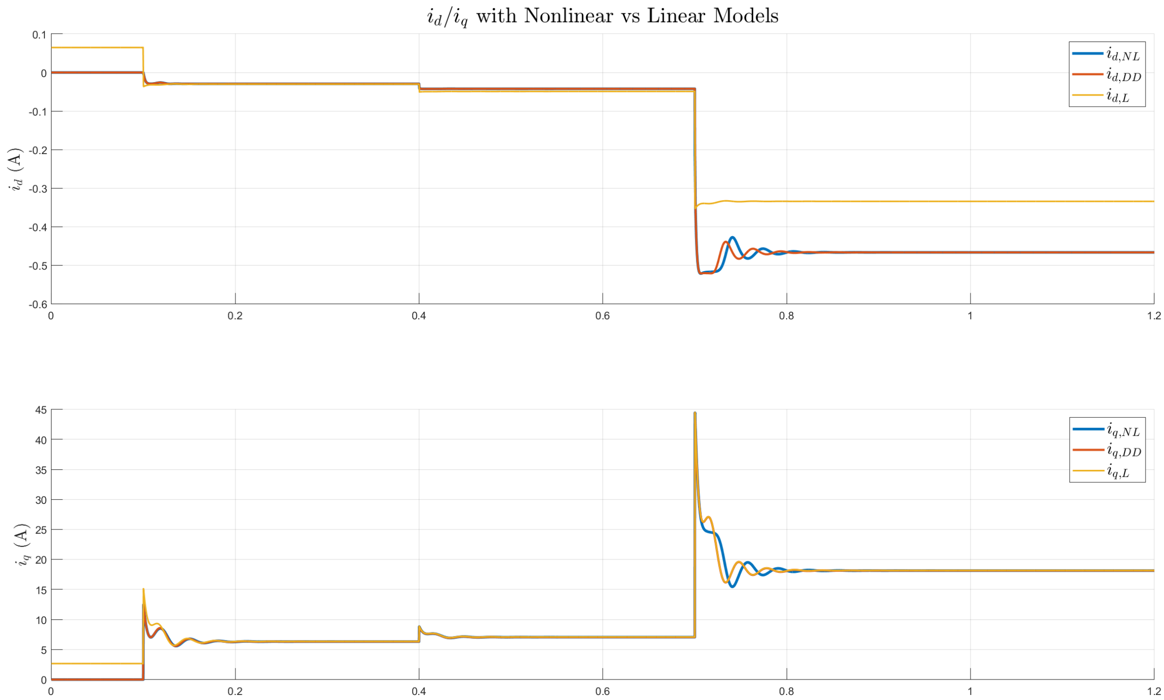

Figure 4.2: Comparison of direct and quadrature axis currents in linear and nonlinear models.

The linearized rotor position and the translator position, when given the initial smaller steps, other than the initial error, can be seen in figure 4.3 and figure 4.4 to follow the nonlinear model very well with only minor differences due to the differing steady-state velocities.

When a larger input is given, the nonlinear model differs more significantly from the linear and directly driven models due to the reducing force at the peak of the F_{mls} curve as seen in figure 2.2. This causes a phase shift and an initial reduction of response amplitude.

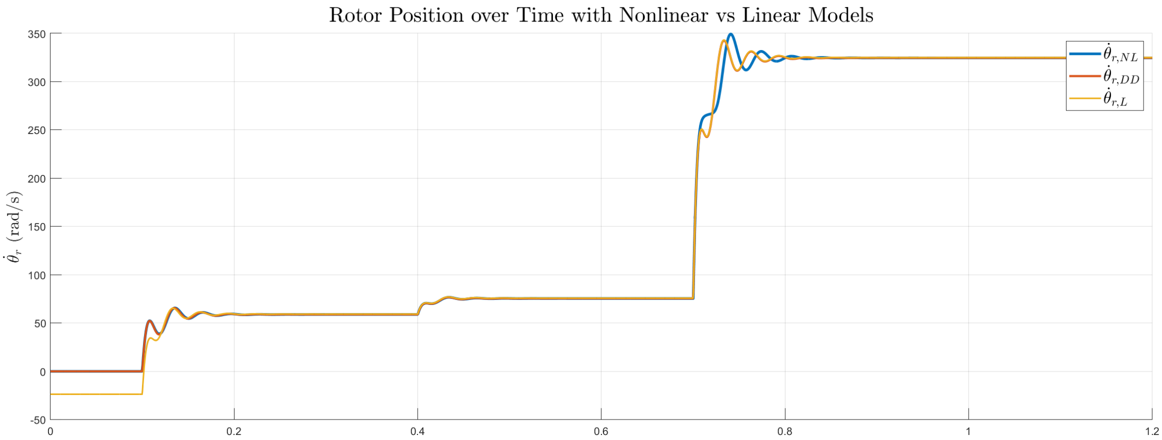

Figure 4.3: Comparison of rotor velocity in linear and nonlinear models.

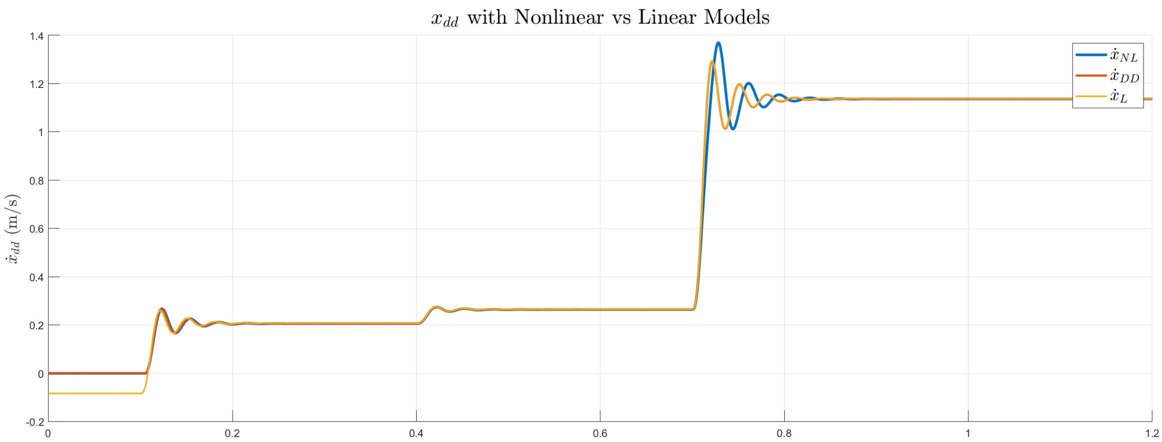

Figure 4.4: Comparison of translator velocity in linear and nonlinear models.

Model Analysis 5

In order to decide how to approach the control design, further analysis of the system behavior is conducted. The analysis begins with investigation of the linearized frequency response of the motor system and a related order reduction of the model, as well as investigation into the coupling between the two inputs of the system. The nonlinearity of the rotor to MLS translator coupling and its significance are then investigated.

5.1 PMSM Behavior

The state space linearized model is first reduced to the current and rotor states in order to determine the behavior of the motor subsystem.

$$\boldsymbol{x} = \begin{bmatrix} i_d & i_q & \theta_r & \dot{\theta}_r \end{bmatrix} \tag{5.1}$$

5.1.1 Current Response

First of all, the behavior of the currents is investigated with direct and quadrature voltage inputs.

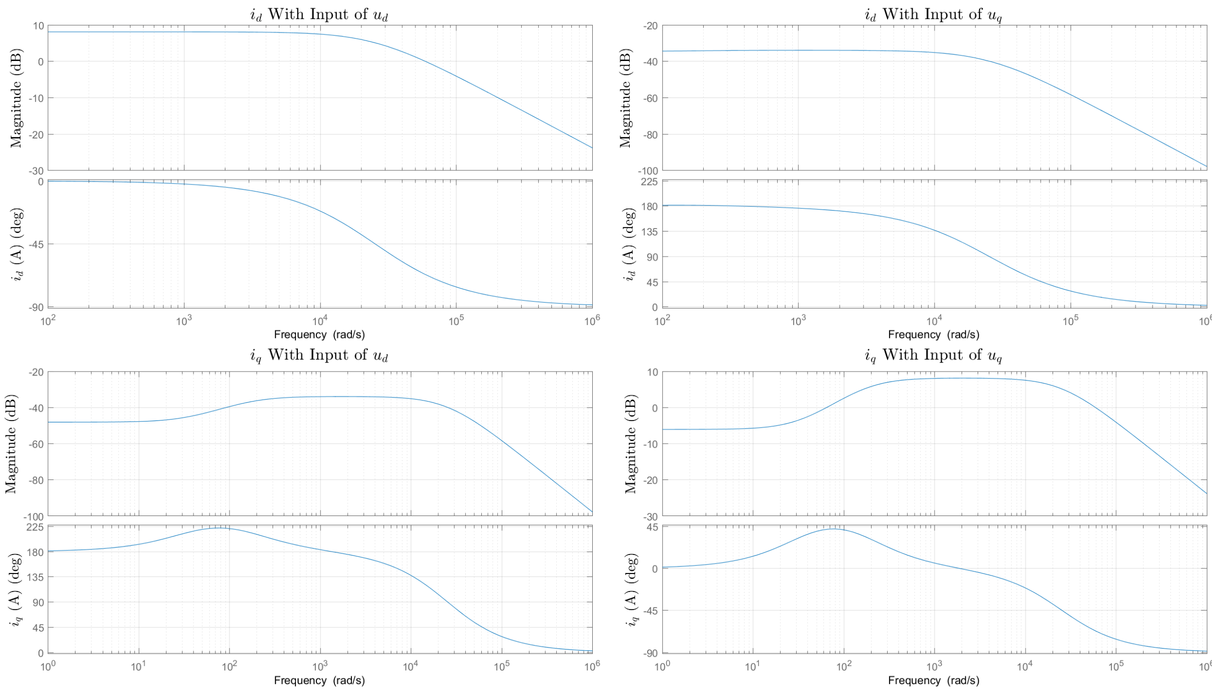

Figure 5.1: Direct and quadrature current frequency responses with respect to both d and q axis voltage inputs.

It can be seen that the d axis current, with a d axis input, behaves as a first order system with a constant gain up to a cutoff frequency of 20000[rad/s]. The d axis current behavior with a q axis input is very similar, however the steady state gain is significantly lower.

The q axis current has a similar cutoff frequency and amplitude to the d axis at higher frequencies, however, at lower frequencies the amplitude is reduced due to the rotor dynamics and associated back-emf. The same behavior can be seen with a d axis input, just with a reduced magnitude.

From these plots, it can be seen that the magnitude of the coupling between the d and q axis currents are significantly lower than the magnitude of the direct relation. Additionally, there are no frequencies where this relation is significantly different thus there are no frequencies of concern where the coupling may become more significant. This means that the coupling effects, though present, should be possible to easily compensate for with basic controllers.

5.1.2 Rotor Response

The behavior of the rotor is then inspected based on a quadrature axis voltage input.

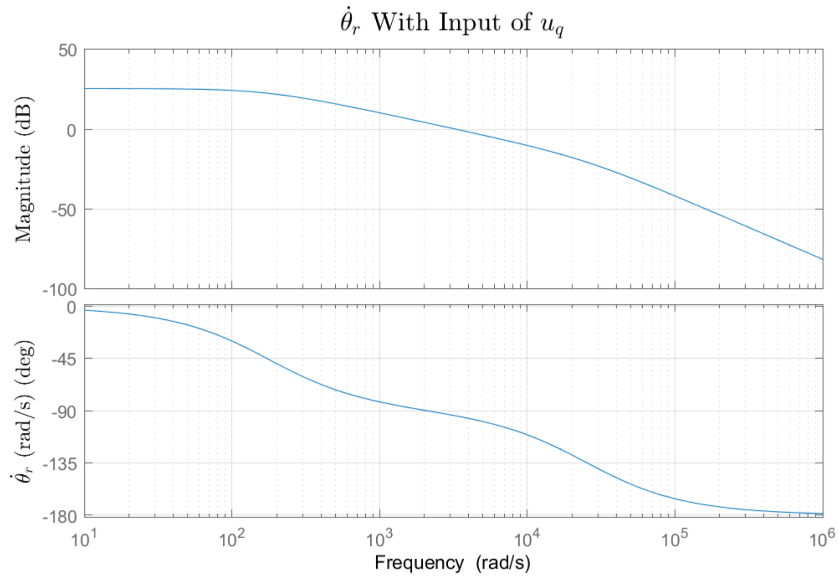

Figure 5.2: Rotor frequency response with respect to quadrature axis voltage input.

It can be seen that the rotor has a consistent steady-state gain up to around 200 rad/s. The amplitude then drops of as the frequency increases. This is in line with the features seen in the bode plots of the q axis current where the magnitude drops even further above 20000 rad/s.

5.2 Mechanical System Response

In order to analyze the behavior of the mechanical system, a reduced model is made with the current states removed and with the q axis current as the input.

$$\boldsymbol{x} = \begin{bmatrix} \theta_r & \dot{\theta}_r & x & \dot{x} \end{bmatrix} \tag{5.2}$$

5.3 Frequency Response

The frequency response about the linearization point is the first portion of the mechanical system to be analyzed. This region is important, though not the most complex region, due to the fact that the settling of the system occurs there.

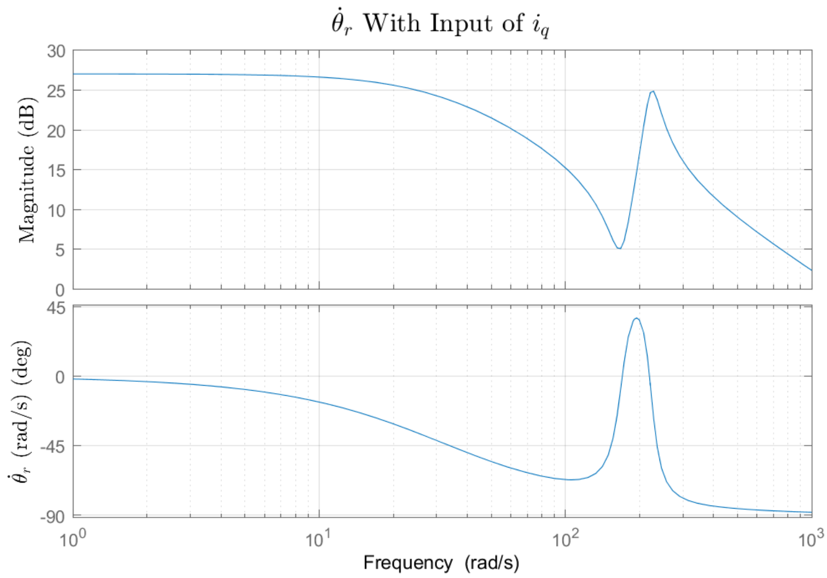

Figure 5.3: Rotor frequency response to quadrature axis input.

It can be seen that there is a significant resonance peak in the rotor response at around 220 rad/s which additionally comes with a significant phase shift as the resonance is caused by feedback from the translator.

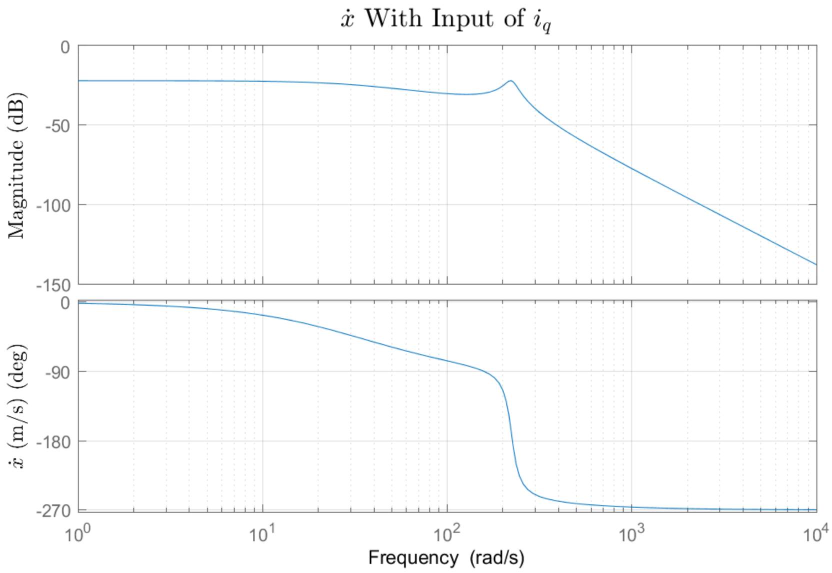

Figure 5.4: Frequency response of MLS translator with quadrature axis input.

The translator can be seen to have a resonance peak in the same location as the rotor, but with a much lower magnitude due to the much larger mass.

Further investigating the poles and zeros of the rotor response, it can be seen that the severe resonance peak is caused by an extra complex zero at 170 rad/s which significantly increased the depth of the trough before the peak at 220radians per second.

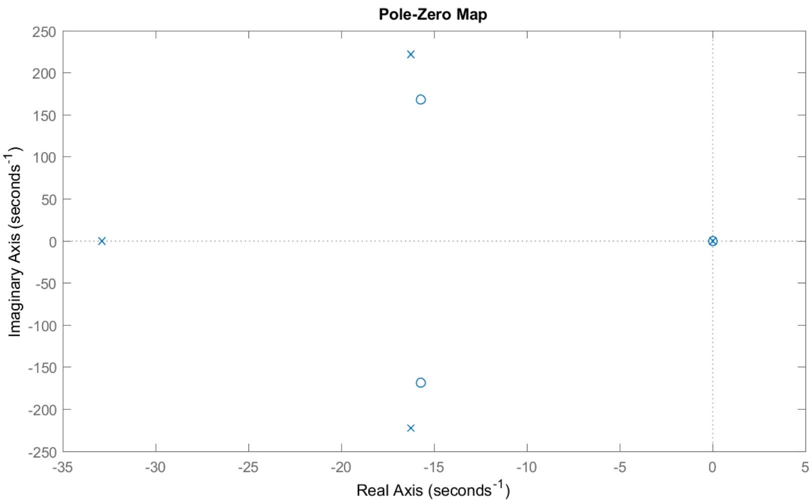

Figure 5.5: Pole-zero map of rotor transfer function.

5.3.1 MLS Nonlinearity

The same mechanical system frequency responses are investigated at various linearization points. The Linearization points are chosen with varying MLS slip amounts in order to gauge the response when the MLS and rotor are in different positions relative to each other. The points chosen are scattered between the zero slip location and 5.5mm slip which is the maximum displacement before the MLS force begins to decrease again.

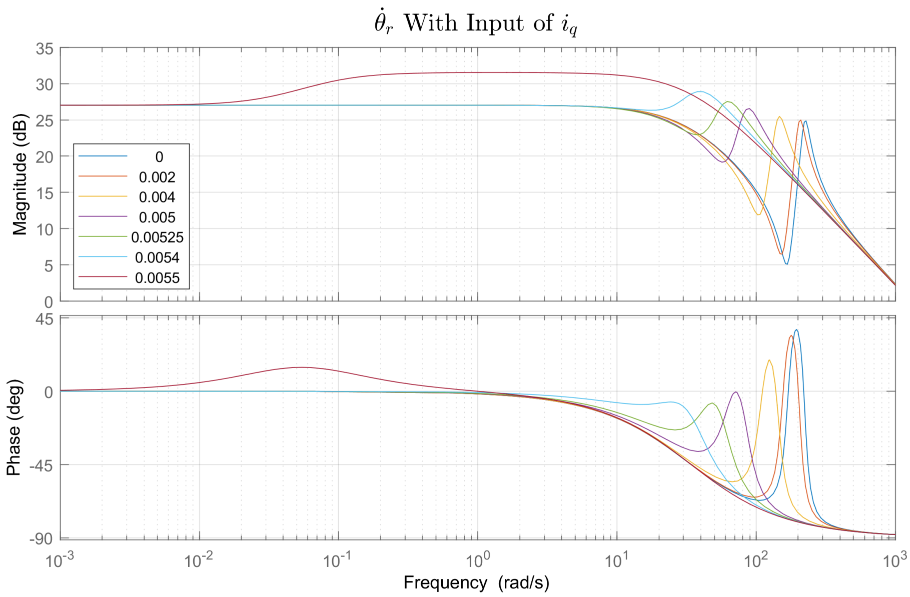

Figure 5.6: Rotor frequency response at various slip distances.

It can be seen that the magnitude and location of the rotor resonance peak decreases as the slip increases. When the MLS is in the maximum force location, it can be seen that changes in the rotor position are a higher amplitude.

Similar behavior can be seen in the translator position where, figure 5.4,as the slip increases the cutoff frequency decreases. As the slip reaches the peak of the force curve, the cutoff frequency drops

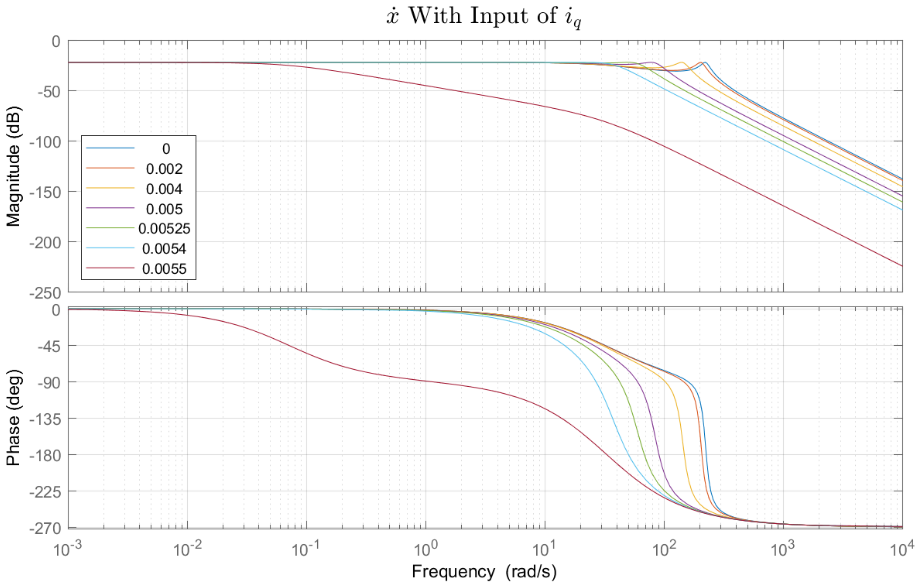

Figure 5.7: MLS translator frequency response at various slip distances.

considerably as the coupling between the rotor and translator is much less.

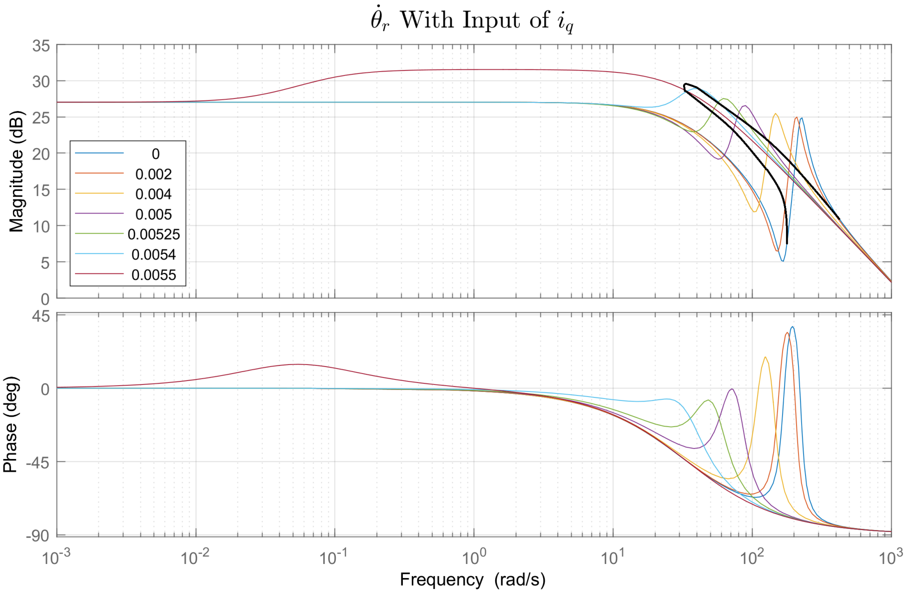

Figure 5.8: Extrapolated nonlinear rotor frequency response curve.

The continuous bode plot for the rotor may be extrapolated from the various curves as seen in figure 5.8. This relationship may be seen in the general behavior of nonlinear softening springs[12]. As the derivative of the force drops to zero as the displacement increases, the extrapolated curve could be extended to a point, however, the specifics of this curve are difficult to determine without extensive testing. As can be seen from the curve, the system is sensitive to the direction of frequency changes, and has the possibility of snap-through where the system jumps from the higher amplitude state to the lower amplitude curve. Thus, it is very difficult to determine a linear localized controller as there are various potential states to compensate for dependant on both frequency and amplitude.

5.4 Linear Model Reduction

In order to conduct the control design, the state-space models are converted into transfer functions. The transfer functions resulting from the model tend to be relatively high order due to the number of interconnected states, thus a model reduction of the insignificant characteristics is helpful for controller design.

5.4.1 Motor Model

In order to calculate the transfer function matrix from the motor reduced state space model, the following equation is used[13].

$$\boldsymbol{L}(s) = \boldsymbol{C}_{motor}(sI - \boldsymbol{A}_{motor})^{-1}\boldsymbol{B}_{motor} + \boldsymbol{D}_{motor} \tag{5.3}$$

$$\boldsymbol{L}(s) = \begin{bmatrix} L_{u_d,i_d} & L_{u_q,i_d} \\ L_{u_d,i_q} & L_{u_q,i_q} \\ L_{u_d,\theta_r} & L_{u_q,\theta_r} \\ L_{u_d,\dot{\theta}_r} & L_{u_q,\dot{\theta}_r} \end{bmatrix} \tag{5.4}$$

Direct Axis Current

From the transfer function matrix, it can be found that the transfer function for the direct axis voltage to direct axis current is third order and has two zeros.

$$L_{u_d,i_d}(s) = \frac{64475(s+2.513e4)(s+175.2)}{(s+2.541e4)(s+2.499e4)(s+175.2)} \tag{5.5}$$

It can be easily seen that one of the poles and one of the zeros are extremely close to each other while the other zero is relatively close to the other two poles.

$$L_{u_d,i_d}(s) = \frac{64475\cancel{(s+2.513e4)}\cancel{(s+175.2)}}{(s+2.541e4)\cancel{(s+2.499e4)}\cancel{(s+175.2)}} \tag{5.6}$$

The closest poles and zeros are cancelled with each other leaving a first order transfer function with a cutoff frequency of $\approx 25k$ rad/s.

$$L_{u_d,i_d}(s) = \frac{64475}{(s+2.541e4)} \tag{5.7}$$

Comparing the two responses with a step input shows that the model reduction very minorly affects the steady-state result of the step, but overall does not create a significant change to the behavior of the direct axis current response.

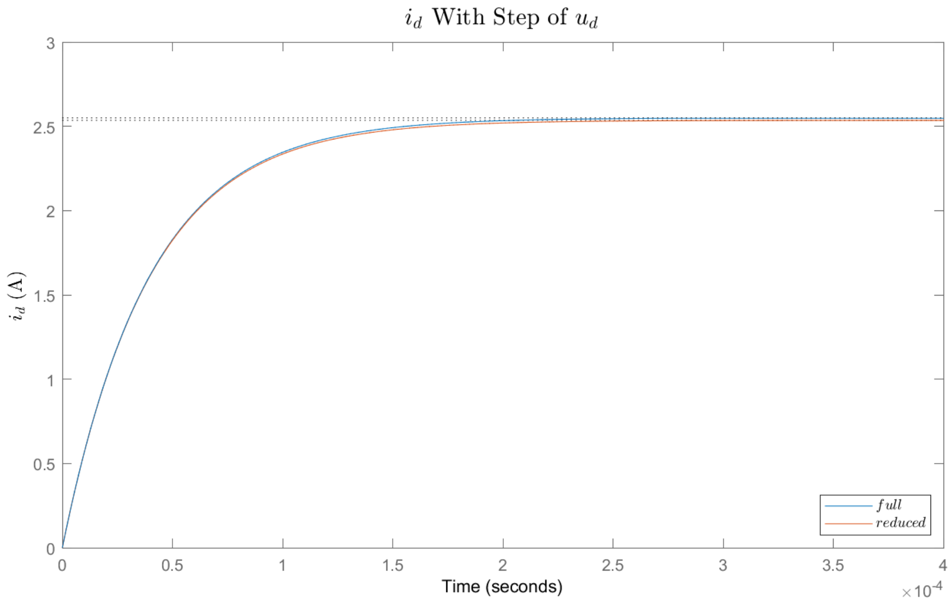

Figure 5.9: Comparison of direct axis current step response with full, and reduced order transfer functions.

Quadrature Axis Current

The transfer function for the quadrature axis current, using the same method, is thus:

$$L_{u_q,i_q}(s) = \frac{64475(s + 2.527e04)(s + 34)}{(s + 2.541e04)(s + 2.499e04)(s + 175.2)} \tag{5.8}$$

Following the same method as before, the high frequency poles may be neglected, however the lower frequency poles in this case are not as close and do not cancel easily. These frequencies are those associated with the rotor velocity and may or may not be relevant depending on the application.

$$L_{u_q,i_q}(s) = \frac{64475\cancel{(s + 2.527e04)}(s + 34)}{(s + 2.541e04)\cancel{(s + 2.499e04)}(s + 175.2)} \tag{5.9}$$

$$L_{u_q,i_q}(s) \approx \frac{64475(s + 34)}{(s + 2.541e04)(s + 175.2)} \approx \frac{64475}{(s + 2.541e04)} \tag{5.10}$$

The fully reduced transfer function can be seen to be identical to the direct axis transfer function.

From the step response of the quadrature axis reduced models, it can be seen that the single order reduced transfer function matches the original closely, however, the double order reduced model is significantly different over large time frames which can be expected due to the change in DC gain caused by canceling a pole with a non-matching zero.

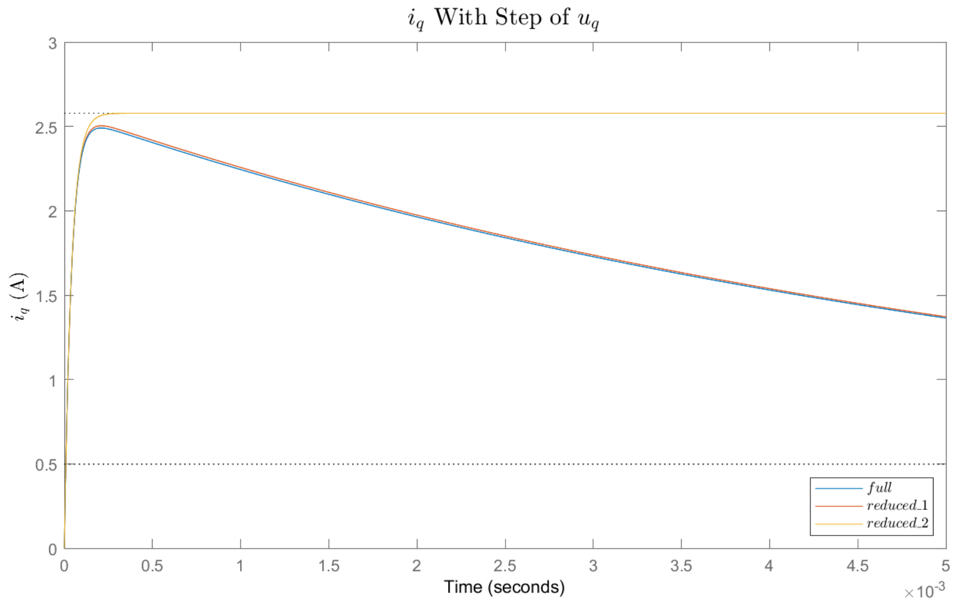

Figure 5.10: Comparison of quadrature axis current step response with full, and reduced order transfer functions.

5.4.2 Mechanical Model

A transfer function matrix is calculated again based on the mechanical system reduced state space model.

$$\boldsymbol{L}(s) = \boldsymbol{C}_{mls}(sI - \boldsymbol{A}_{mls})^{-1}\boldsymbol{B}_{mls} + \boldsymbol{D}_{mls} \tag{5.11}$$

$$\boldsymbol{L}(s) = \begin{bmatrix} L_{i_q,\theta_r} \\ L_{i_q,\dot{\theta}_r} \\ L_{i_q,x} \\ L_{i_q,\dot{x}} \end{bmatrix} \tag{5.12}$$

MLS Translator

The transfer function for the MLS translator is found to be:

$$L_{i_q,\dot{x}} = \frac{1.284e5s}{s(s+32.92)(s^2+32.53s+4.957e4)} \tag{5.13}$$

The transfer function consists of one complex pole, one real pole, and a pair of poles and zeros at 0 rad/s. These poles and zeros can be easily cancelled to reduce the transfer function to a third order transfer function.

$$L_{i_q,\dot{x}} = \frac{1.284e5}{(s+32.92)(s^2+32.53s+4.957e4)} \tag{5.14}$$

From this point, neither the 32.92 rad/s pole or the complex pole may be neglected as they are the first order response dynamics, and the oscillatory feedback from the rotor, respectively.

As can be expected, the step response of the full and reduced transfer functions are identical.

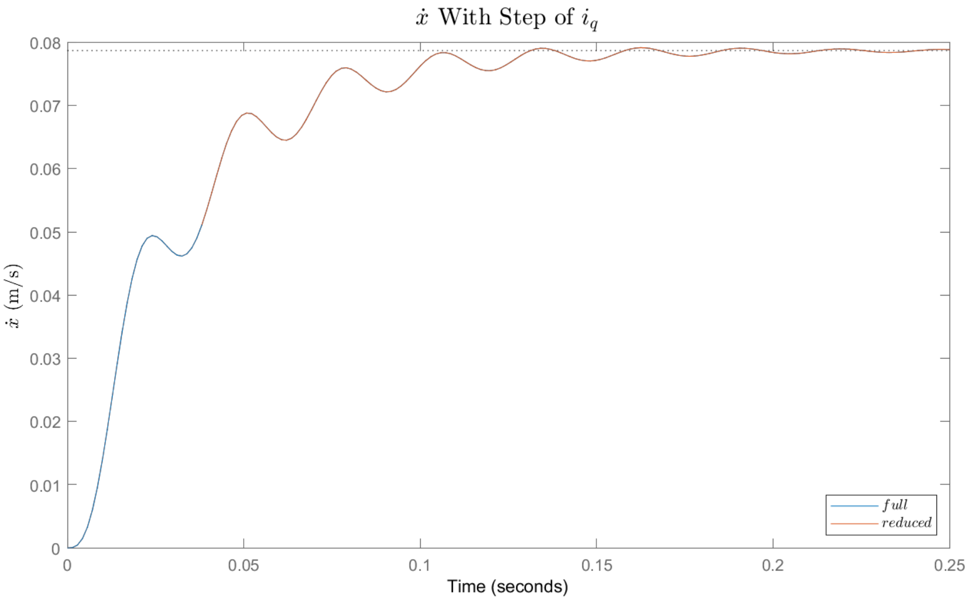

Figure 5.11: Comparison of MLS step response with full and reduced order transfer functions.

PMSM Rotor

The model reduction for the rotor dynamics follows the same process again where the transfer function is:

$$L_{i_q,\dot{\theta}} = \frac{1284s(s^2 + 31.45s + 2.856e4)}{s(s + 32.92)(s^2 + 32.53s + 4.957e4)} \tag{5.15}$$

Again the pole and zero at 0 rad/s may be cancelled.

$$L_{i_q,\dot{\theta}} = \frac{1284(s^2 + 31.45s + 2.856e4)}{(s + 32.92)(s^2 + 32.53s + 4.957e4)} \tag{5.16}$$

The complex poles and zeros are far enough apart that they may not be easily cancelled with each other and the significance of these features can be seen in the higher frequency oscillatory behavior of the rotor.

With the reduced transfer function, it can again be seen that the step behaviors are identical.

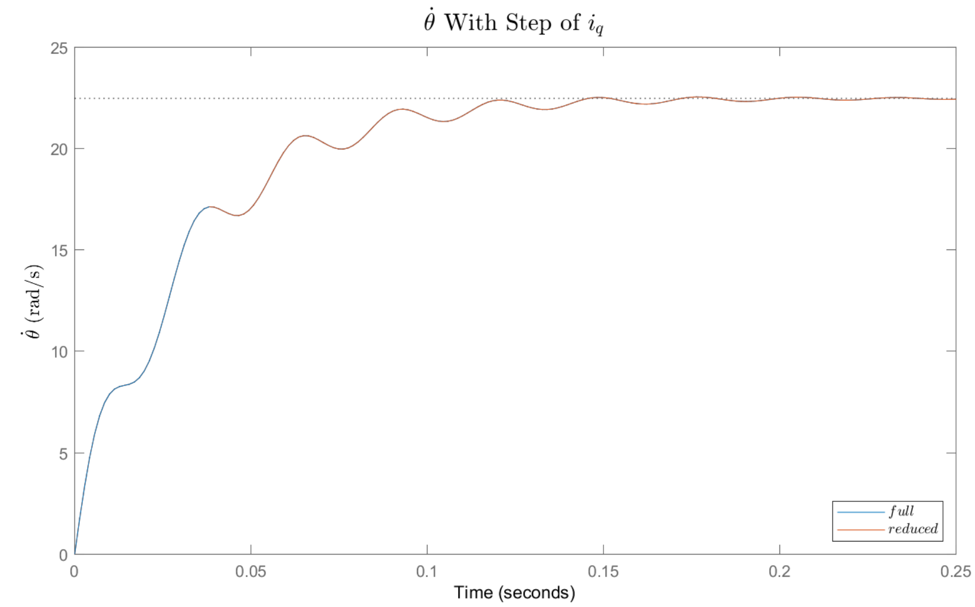

Figure 5.12: Comparison of rotor step response with full and reduced order transfer functions.

5.5 Analysis Conclusion

From the analysis of the motor-reduced system, it can be concluded that the currents can reasonably be controlled by individual controllers as the coupling is insignificant and the mechanical dynamics of the rotor may be neglected in the current controller design due to the much lower bandwidth.

In the analysis of the mechanical subsystem, it can be seen that around the central operating point, there is a significant resonance peak which must be considered when operating at higher velocities. The translator does not have as significant of a peak in this area, however, the significant phase shift must be considered. In the analysis of the non-linearity of the MLS, it was found that the non-linearity significantly affects the higher frequency response of the system and is significantly amplitude dependant.

Based on the understanding of the critical characteristics of the system, a model reduction was conducted on transfer functions calculated from the state space model. Based on these and the previous analysis, a basis is created for the control design.

Control Design 6

In this section, the control design and the process used for making the control decisions will be discussed.

6.1 Control Design Methodology

The system to be controlled, as modelled, has the following properties:

- Two inputs, one which does not have a significant effects on the system states (u_d), and one which strongly effects the system states (u_q).
- Two states which respond significantly faster than the other system states (100x).
- One state to be controlled (x_{mls}).
- Mechanical dynamics are dominated by a first order response (32 rad/s).
- Both mechanical states are sensitive to oscillation at high frequencies (222 rad/s).

Based on these properties, the control design will begin by developing controllers for the motor currents. The direct axis current will be controlled to a reference of 0A as it does not significantly impact the system behavior. The quadrature axis current will be controlled in order to be fast enough to be used as an input to the mechanical system without having to consider the input dynamics.

The control design for the mechanical system will thus be able to consider the quadrature axis current(i_q) as the only input and the MLS translator position (x_{mls}) as the only output, making the control problem possible to be considered as a single input single output (SISO) problem.

Based on the above properties and decisions, for the purpose of the control design, the control system will be considered to be implemented as shown in figure 6.1. This means that the items within each loop will be assumed to have the related sampling frequency and will be limited by the calculation capabilities of the microcontroller within the associated timeframe.

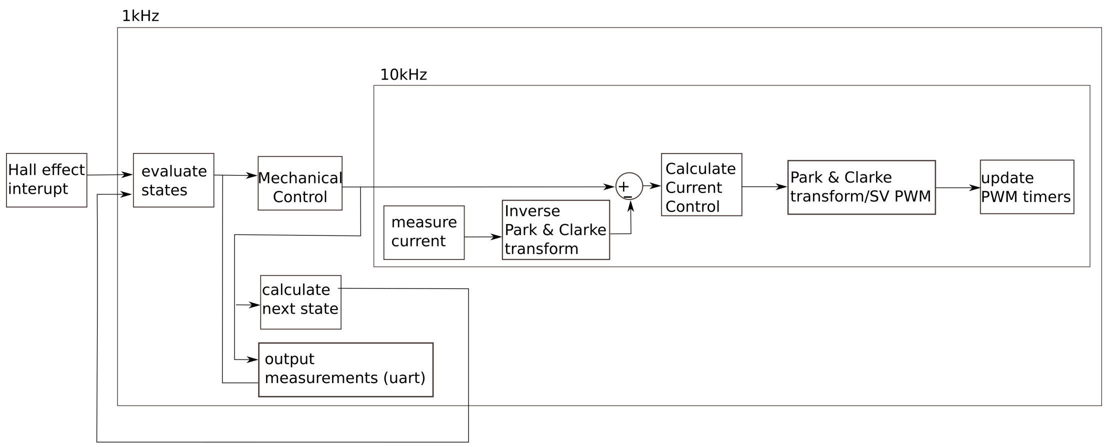

Figure 6.1: The assumed implementation of controllers on the microcontroller used in control design.

In order to determine the suitability of a control solution, the solutions will be evaluated based on the speed possible with the solution, the peak overshoot, and the sensor requirements for realising the solution.

6.2 Ideal MLS Trajectory

As the main goal of the control design is optimising the speed of the control, the theoretical ideal speed must be identified. In order to do this, the reference to be used for testing must be defined.

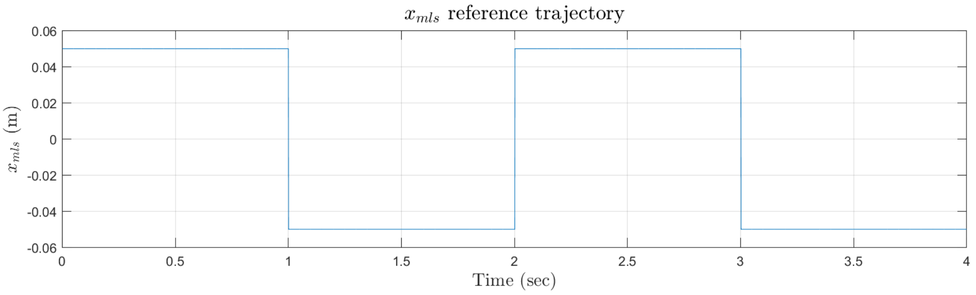

Figure 6.2: Reference trajectory used for testing control performance.

As the system has various characteristics that make stable acceleration and deceleration challenging, the reference is defined as a square wave with a period of two seconds and an amplitude of 0.05m.

The amplitude of this reference is chosen in order to stay comfortably within the bounds of the MLS stroke on the test machine without risking collisions. The time frame is chosen to be much larger than that theoretically possible in order to ensure that any settling dynamics are identified.

The maximum acceleration possible to be realized by the MLS is defined by the stall force and the translator mass as:

$$a_{max} = \frac{F_{max}}{M} \approx 100\frac{m}{s^2} \tag{6.1}$$

Using this number, the time needed to accelerate over some distance may be calculated. As the trajectory includes acceleration and deceleration, the time needed to accelerate half the distance is used.

$$t = 2\sqrt{\frac{2d}{a_{max}}} = 2\sqrt{\frac{2 \cdot 0.05}{100}} \approx 0.063sec \tag{6.2}$$

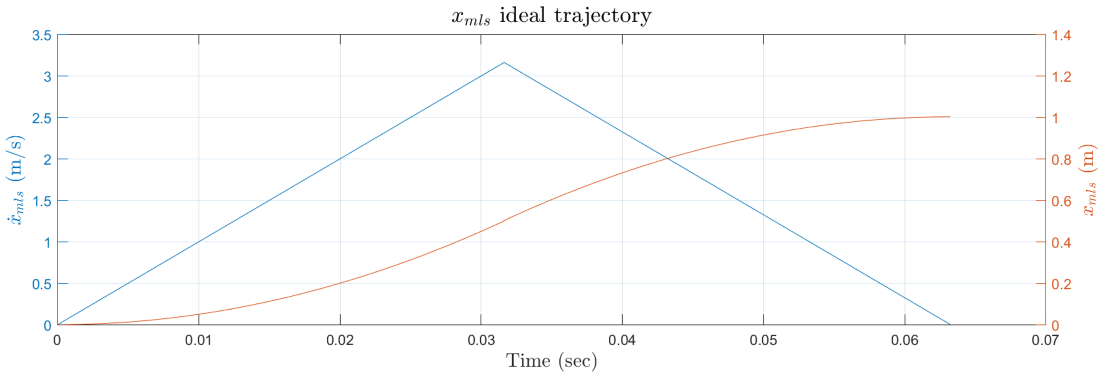

Figure 6.3: Idealized MLS translator travel and settling behavior.

This travel time is very fast, and in fact is unrealistic for various reasons. The main reason that a triangular trajectory is not possible is due to the presence of viscous and static frictions in the system.

Accounting for these, the trajectory becomes fairly different and the travel time increases to 0.73 seconds.

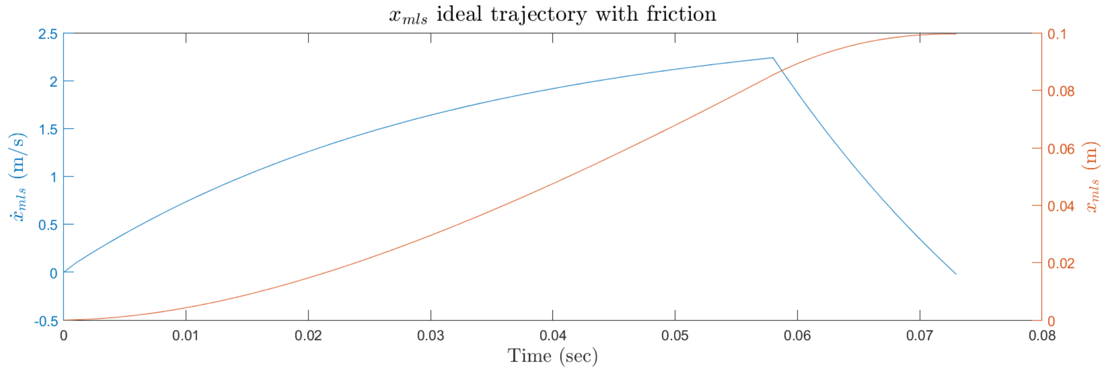

Figure 6.4: Idealized MLS translator travel and settling behavior with friction.

This trajectory only considers the dynamics of the MLS and thus the actual realizable time is increased by the amount of time it takes for the rotor to apply the peak force to the MLS, as well as the efficiency of the control algorithm.

6.2.1 Evaluating Tracking Performance

In order to judge the efficiency of the control performance, the controllers will be judged on the following criteria:

Travel Time

The main criteria for judging the performance of the controller is the time taken to settle at the reference value.

$$e = x_{ref} - x_{mls} \tag{6.3}$$

Based on the error, the settling time is defined as the time at which the absolute value of the error settles under ± 0.001m and remains within that bound until the reference is updated.

6.2.2 Peak error

The second criteria is the peak error. As the reference used is a step function, the peak error will always be the reference, thus the peak error measured will be the peak once the reference is reached. This is not as informative in terms of system speed, however it does provide some insight into the settling behavior of the system with a controller.

6.3 Cascaded Current Controllers

The first controllers to be developed are the current controllers. As the current dynamics are significantly faster than those of the mechanical system, they will be considered independently.

6.3.1 Discrete Time Considerations

In addition to the previous considerations in the system analysis, the discrete nature of the implementation has to be considered. Relevant to the current control are the sample time, the control calculation time, and the measurement resolution.

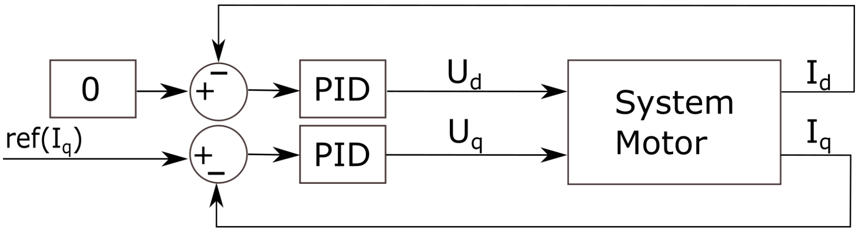

Figure 6.5: Block diagram for implementation of current controllers.

The sample time and the control calculation time are assumed to be at the same frequency as they will be measured and calculated in the same step. For the purpose of the control testing, the sample time will be defined by:

$$t_s = \frac{1}{10kHz} = 0.1ms \tag{6.4}$$

The current measurement resolution is determined by the electronics on the inverter board as well as the resolution of the analog to digital converter in the microcontroller.

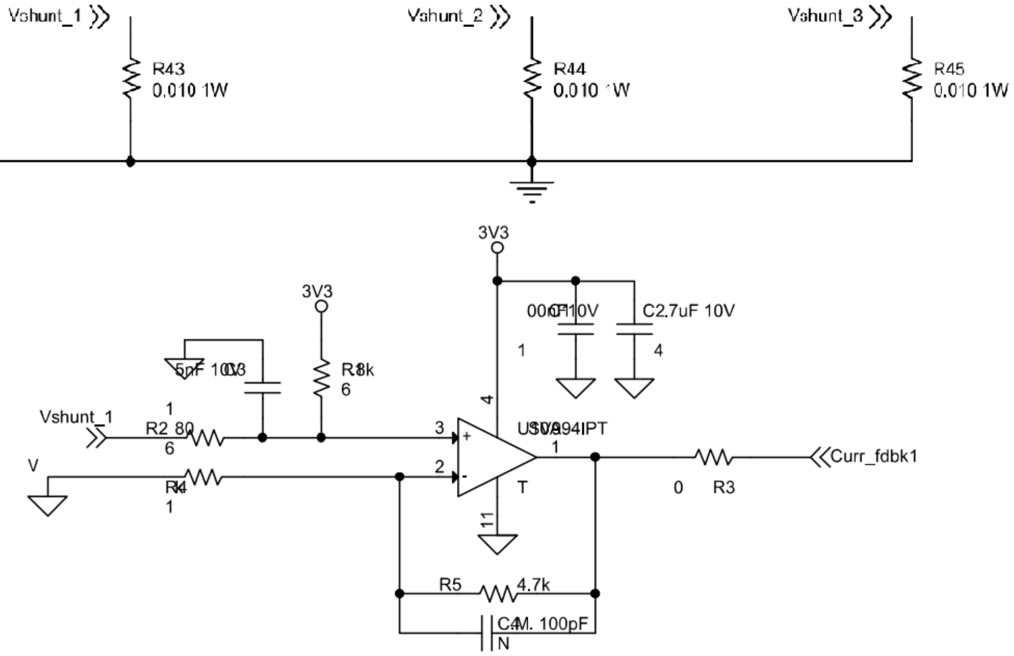

Figure 6.6: IHM08M1 inverter current measurement circuitry as presented in the datasheet[9].

The current is measured through the use of a 0.01Ω shunt resistor between each phase and ground. The voltage difference is amplified through use of an operational amplifier in a non-inverting amplifier configuration. Directly from the resistor, the current measurement can be found to be:

$$V = IR \tag{6.5}$$

$$\frac{V}{I} = R = 0.01\frac{v}{A} \tag{6.6}$$

As the ADC in the STM32F446 has a 12 bit resolution, the measurement resolution would be defined by:

$$\frac{0.01\ I}{V_{ref}} 4096 = \frac{12.4}{A} \tag{6.7}$$

$$\frac{1}{12.4} = 0.08\frac{A}{LSB} \tag{6.8}$$

The amplifier can be described by:

$$V_{out} = \left(1 + \frac{R_2}{R_1}\right) V_{in} \tag{6.9}$$

Where in this case, the terms are replaced with the values from the above schematic.

$$V_{out} = \left(1 + \frac{4.7k\Omega}{1k\Omega}\right) V_{in} \tag{6.10}$$

$$V_{out} = 5.7V_{in} \tag{6.11}$$

$$\frac{5.7 \cdot 0.01\ I}{V_{ref}} 4096 = \frac{70.7}{A} \tag{6.12}$$

$$\frac{1}{12.4} = 0.014 \frac{A}{LSB} \tag{6.13}$$

This gives a more reasonable current resolution which, while it may not be necessary for the application, allows for much more accurate calculations based on the current.

6.3.2 Direct Axis Current Controller

In order to design the d axis current controller, the transfer function identified in the analysis section is used.

$$L_{u_d,i_d}(s) = \frac{64475}{(s + 2.541e4)} \tag{6.14}$$

An 'ideal' controller for this transfer function would be defined as the inverse of the response transfer function.

$$C_{i_d}(s) = \left(\frac{64475}{(s + 2.541e4)}\right)^{-1} = 1.551e{-5}(s + 2.542e4) \tag{6.15}$$

Thus the open loop response can be determined by:

$$L_{u_d,i_d}(s) CON_{i_d}(s) = 1 \tag{6.16}$$

This response means that, theoretically, the current would be exactly the input, however this is not guaranteed to be true when non-linearities or disturbances are present. Additionally, the input saturation as an infinite voltage may not be provided, means that the response will not follow the reference ideally. In order to rectify this, a desired first order response time is defined, where tau is the time constant.

$$\frac{K}{\tau s + 1} \tag{6.17}$$

For a first order system, the settling time is typically considered to be 4 to 5 times the time constant[14]. Thus, the desired settling time can be defined by:

$$t_{settling} = 4\tau \tag{6.18}$$

In order to realise the first order dynamics, an integral controller is added to the previously determined 'ideal' controller.

$$C_{i_d}(s) = 1.551e - 5(s + 2.542e4) \cdot \frac{1}{\tau s} \tag{6.19}$$

When the controller is applied to the system in a closed loop, the transfer function becomes:

$$\frac{C_{i_d}(s)L_{u_d,i_d}(s)}{1+C_{i_d}(s)L_{u_d,i_d}(s)} = \frac{1}{\tau s+1} \tag{6.20}$$

Due to the discretised signal,the controller may not behave reliably if the time constant is too low, thus the time constant will be selected to settle within ten measurement periods.

$$\tau = \frac{10t_s}{4} \tag{6.21}$$

$$C_{i_d}(s) = \frac{0.06204(s+2.542e4)}{s} \tag{6.22}$$

In order for the controller to be implemented, it may be decomposed into a PID controller with the format[14]:

$$u(t) = K_p e(t) + K_i \int_0^t e(t)dt = \frac{K_p s + K_i}{s} \tag{6.23}$$

$$K_p = 0.062 \quad K_i = 1576 \tag{6.24}$$

Applying this controller to the system with a low amplitude step to the direct axis current results in the response seen in figure 6.7.

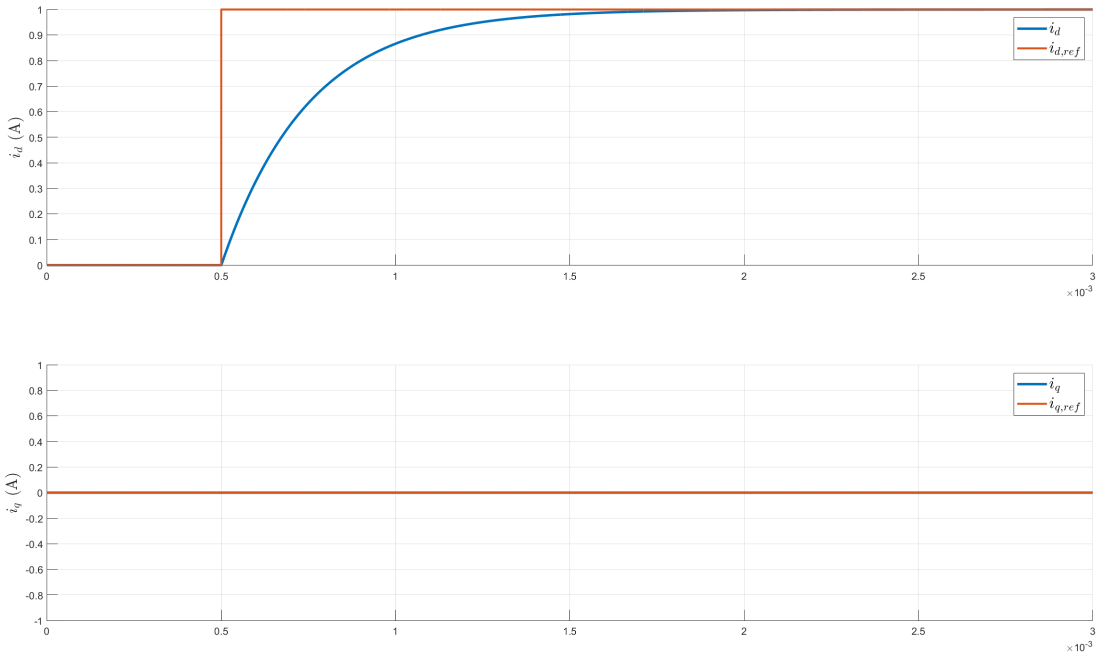

Figure 6.7: Testing of continuous time direct axis current controller.

The direct axis current reaches the desired value at approximately ten times the sample time. The quadrature axis current stays at zero as the rotor is stationary. No steady-state error is seen as can be expected with an integral component to the controller and with the test chosen.

6.3.3 Quadrature Axis Current Controller

The controller for the quadrature axis will follow the same process and many of the same considerations apply. The transfer function previously identified is:

$$L_{u_q,i_q}(s) \approx \frac{64475(s+34)}{(s+2.541e04)(s+175.2)} \approx \frac{64475}{(s+2.541e04)} \tag{6.25}$$

The low frequency dynamics caused by the rotor back-emf are chosen to be neglected in the controller design as the integral controller should dominate the response. With this exclusion, the same process as the direct axis current controller may be used and an identical controller is created.

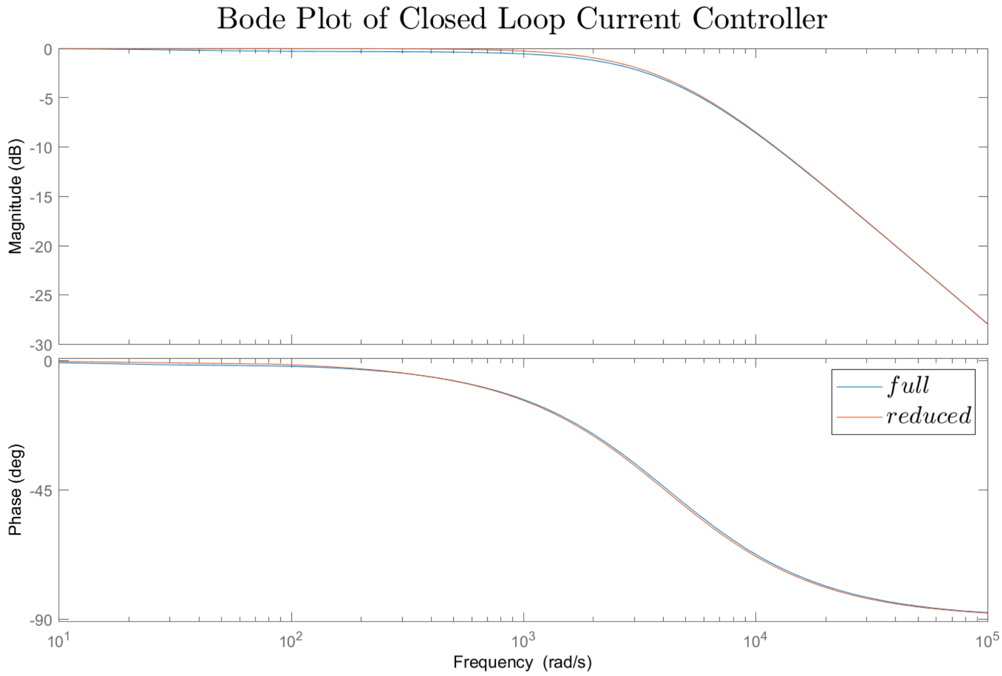

Figure 6.8: Closed loop frequency response of quadrature axis current controller when applied to the full and the reduced order transfer functions.

In the bode plot of the closed loop response in figure 6.8, when the controller is applied to the full and the reduced transfer functions for the quadrature axis current, it can be seen that the frequency response discrepancies are very small.

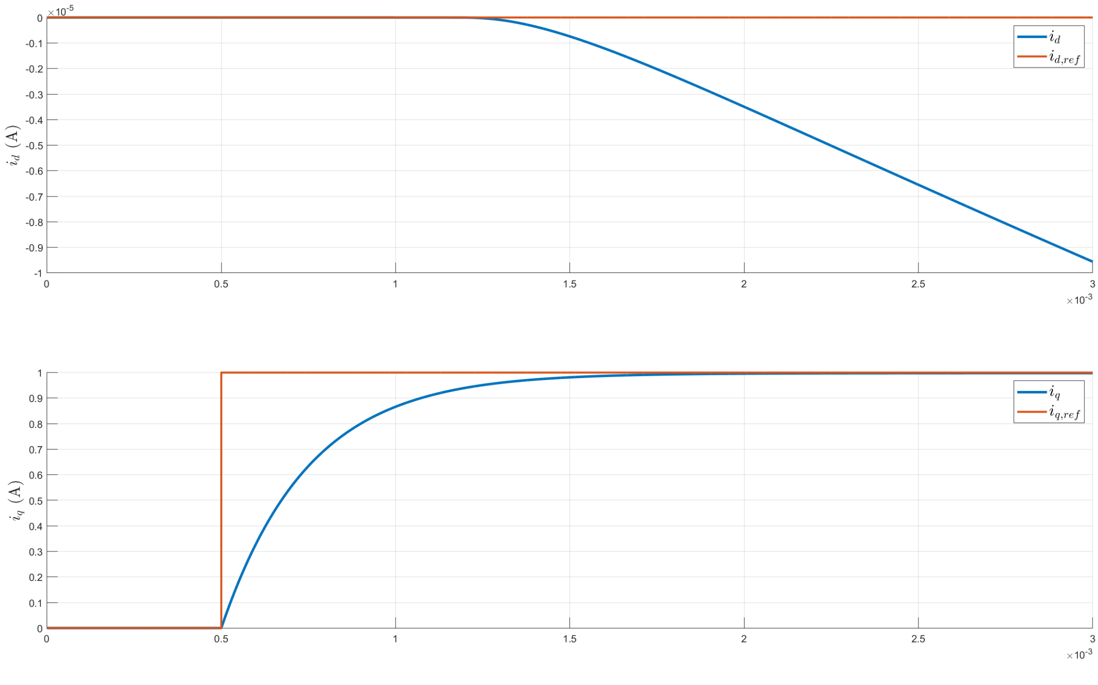

Figure 6.9: Testing of continuous time quadrature axis current controller.

When the controller is applied to the quadrature axis current, the response is seen to be very similar to that of the direct axis test. As no controller is applied to the direct axis, the d axis current diverges from zero, however, the magnitude is so small in this timeframe, due to the low rotor speed, that it does not effect the q axis response significantly.

6.3.4 Discrete Time Current Controllers

As the controllers are not able to be calculated continuously in implementation, they have to be converted to work in discrete time. In a discrete time implementation, the equations typically take the form of difference equations as such:

$$0th\ order \quad m(0) = b_0 e(0) \tag{6.26}$$

$$1st\ order \quad m(T) = b_0 e(T) + b_1 e(0) - a_1 m(0) \tag{6.27}$$

$$2nd\ order \quad m(2T) = b_0 e(2T) + b_1 e(T) + b_2 e(0) - a_1 m(T) - a_2 m(0) \tag{6.28}$$

The general form for a nth order difference equation may be written as[14]:

$$m(k) = b_0 e(k) + b_1 e(k-1) + ... + b_n e(k-n) - a_1 m(k-1) - ... - a_n m(k-n) \tag{6.29}$$

In order to convert the controller transfer function into a discrete time form, the bilinear transform is used. The bilinear transform is a first order approximation of the mapping of the s-plane to the z-plane.

$$s = \frac{2}{T}\frac{1-z^{-1}}{1+z^{-1}} \tag{6.30}$$

Applying the transformation to the controller transfer function results in a discrete time PI controller:

$$C_{i_d}(s) = \frac{0.06204(s + 2.542e4)}{s} \tag{6.31}$$

$$C_{i_d}(z) = \frac{0.14089(z + 0.1193)}{(z-1)} = K_p + K_i \frac{T_s(z+1)}{2(z-1)} = K_p + K_i \frac{T_s(1+z^{-1})}{2(1-z^{-1})} \tag{6.32}$$

Which may be converted into a difference equation through:

$$\frac{u(z)}{e(z)} = K_p + K_i \frac{T_s(1+z^{-1})}{2(1-z^{-1})} = \frac{2K_p(1-z^{-1}) + K_i T_s(1+z^{-1})}{2(1-z^{-1})} \tag{6.33}$$

$$2(1-z^{-1})u(z) = (2K_p(1-z^{-1}) + K_i T_s(1+z^{-1}))e(z) \tag{6.34}$$

$$2(u(z) - u(z-1)) = 2K_p(e(z) - e(z-1)) + K_i T_s(e(z) + e(z-1)) \tag{6.35}$$

$$u(z) = u(z-1) + 2K_p(e(z) - e(z-1)) + \frac{1}{2}K_i T_s(e(z) + e(z-1)) \tag{6.36}$$

Implementing the discrete-time PID controller to the system results in the response seen in figure 6.10. These results are obtained with a sampling time/control loop frequency of 10kHz. As well as the implementation of the current measurement sampling resolution. The response with the discrete controller can be seen to behave similarly to the continuous tests, however a small amount of overshoot is present as well as a low frequency error caused by the motor back-emf.

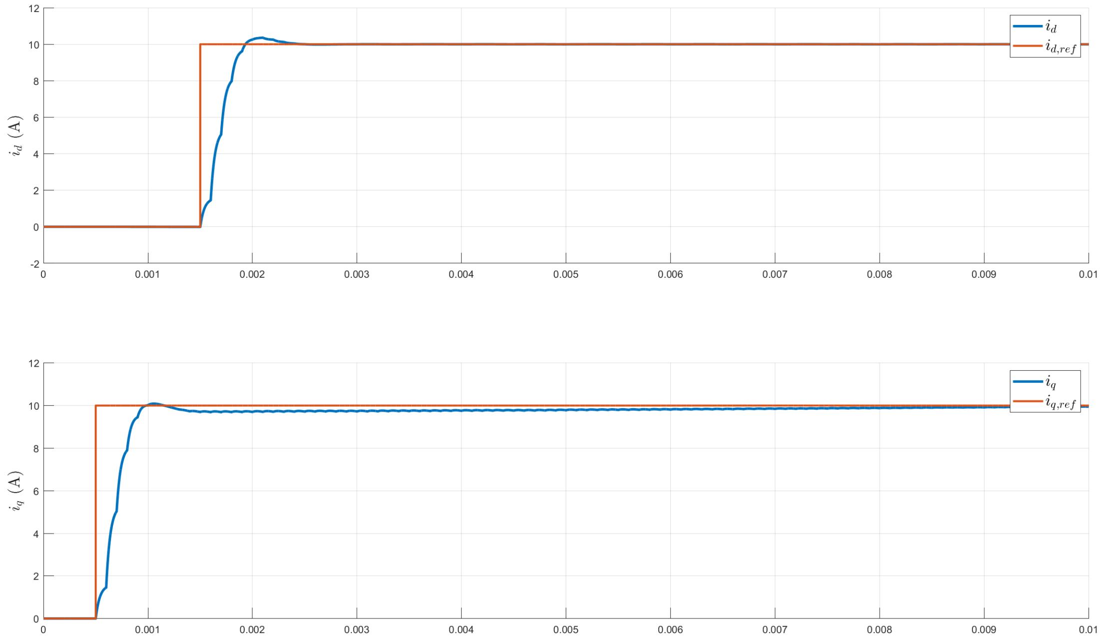

Figure 6.10: Testing of discrete time current controllers.

6.4 Two Stage Slip Controller

As the main complicating factor in the control design is the slip between the rotor and the translator position, it logically follows to control the slip in some way to give a more predictable behavior. For this, the transfer function for the slip is found through subtracting the scaled rotor velocity transfer function from the translator velocity transfer function.

$$L_{slip} = L_{\dot{x}_{mls}} - \frac{\gamma}{2\pi} L_{\dot{\theta}} \tag{6.37}$$
$$L_{slip} = \frac{-4.4981(s+32.92)(s+31.01)(s+0.4397)}{(s+32.92)^2(s^2+32.53s+4.957e04)} \tag{6.38}$$

The poles causing the oscillation and thus the majority of the complications in the control are the complex poles previously mentioned in the section 5.3. Canceling out these poles can be done by creating a transfer function with zeros in the same location, and then adding a filter with cutoff frequency ω_f in order to make the transfer function proper. Additionally, to get the desired closed loop settling dynamics, an integrator is added similarly to with the current controllers.

$$C_{slip} = \frac{(s^2+32.53s+4.957e04)}{1} \left(\frac{\omega_f}{s+\omega_f}\right)^2 \frac{1}{\tau s} \tag{6.39}$$

Applying the controller to the slip transfer function presents a much more desirable frequency response as seen in figure 6.11.

In order to test this controller, the step response of the slip was tested on both the linear "Direct Drive" model and on the nonlinear model. A reference step of 3mm was given as beyond this, the nonlinearity of the MLS makes the linear controller unstable.

In figure 6.12, both the nonlinear and the direct drive systems are effectively pushed to the reference value. The nonlinear response has many more oscillations, likely due to the changing natural frequency of the rotor-translator system as the slip increases.

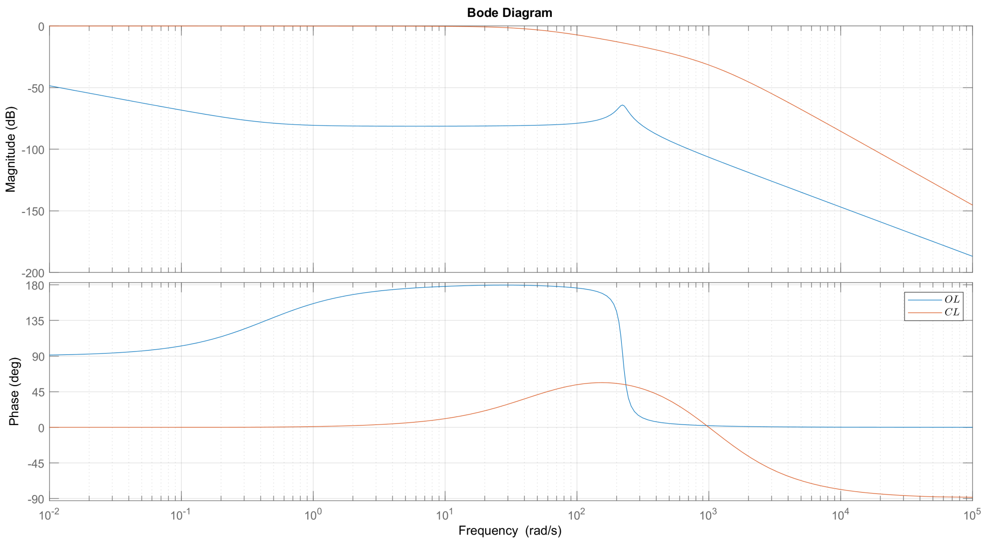

Figure 6.11: Open loop slip frequency response compared to closed loop with controller.

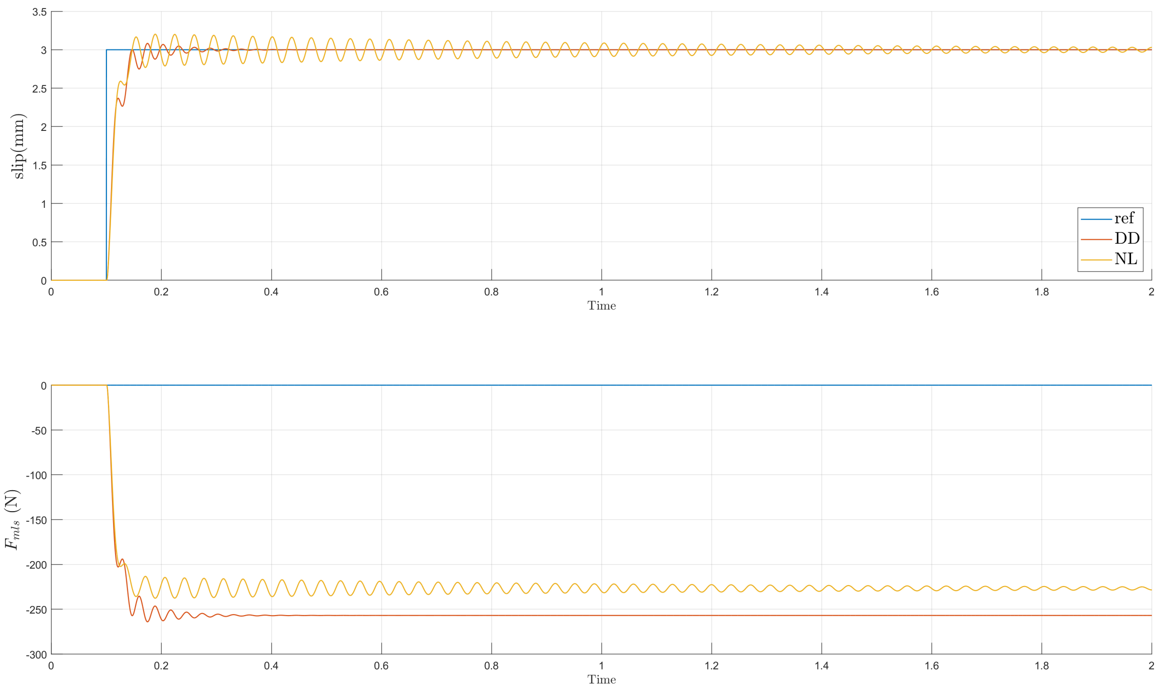

Figure 6.12: Slip response to step with slip controller.

In the current response of the test, figure 6.13, the quadrature axis current can be seen to have a relatively smooth curve other than one rapid change in direction where it likely cancelled out a high frequency oscillation caused by the rapid excitation of the system by the step response. As the slip increases, the effectiveness of the controller becomes less prominent.

The controller is then tested with the reference trajectory and a hand tuned PID controller for determining the slip reference value based on the translator position error.

From the performance of the translator with the PID controller implemented, seen in figure 6.14, the controller works very effectively for both the nonlinear and direct drive models. Both tests show a minor amount of steady-state error, however, considering that no static friction compensation is implemented,

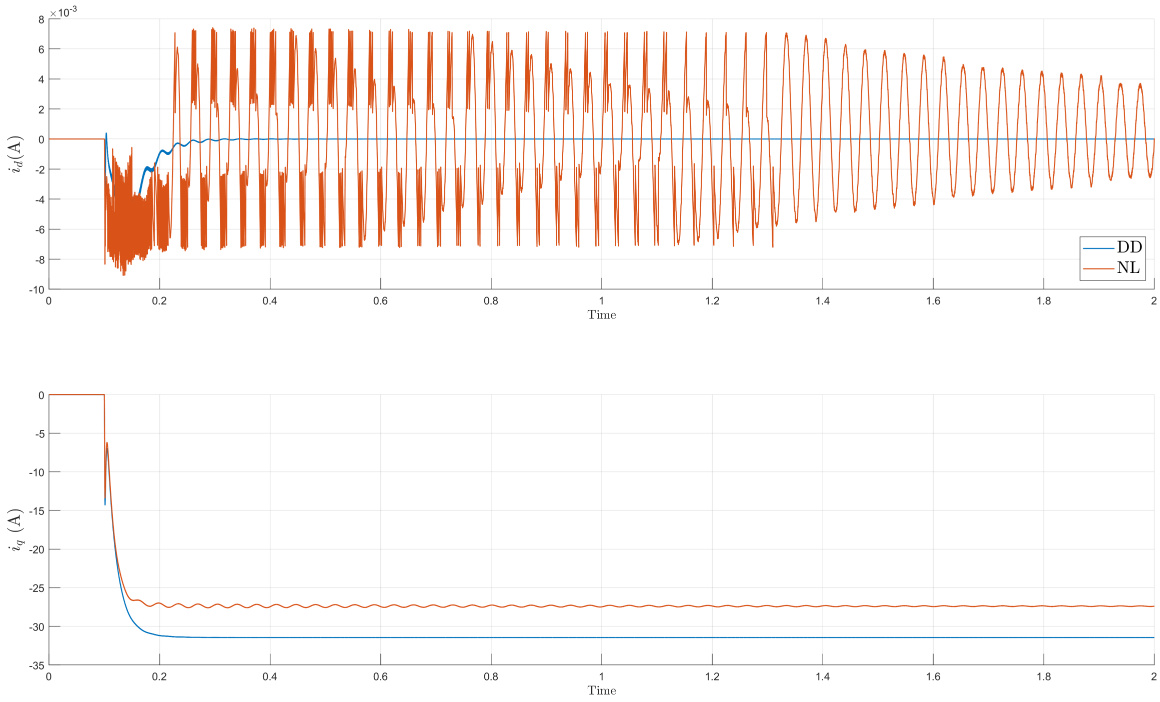

Figure 6.13: Current response to step with slip controller.

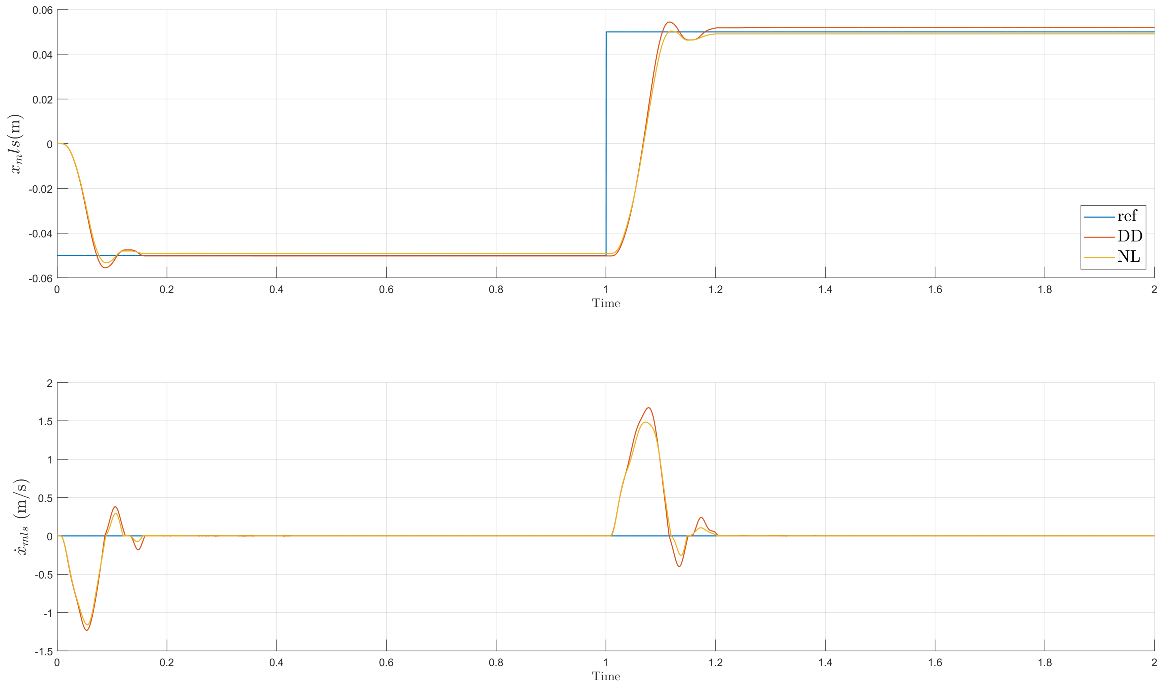

Figure 6.14: Translator response to reference trajectory with slip controller.

the performance is fairly effective.

The slip response under the same test, with the reference value generated by the PID controller, can be seen in figure 6.15, where the value of the slip follows closely behind the reference. The slip tracking is relatively free of excess oscillations compared to many other control tests on the system, however, if the slip controller time constant is made much faster, the system becomes unstable. This controller is not taken further as the instability to high slip values and sensitivity to excitation makes testing of discretization and friction compensation challenging.

	T_s(5cm)	T_s(10cm)	OS(5cm)	OS(10cm)
SC_{DD}	0.14sec	$--$	5mm	4mm
SC_{NL}	0.15sec	0.19sec	3mm	3.7mm

Table 6.1: Caption

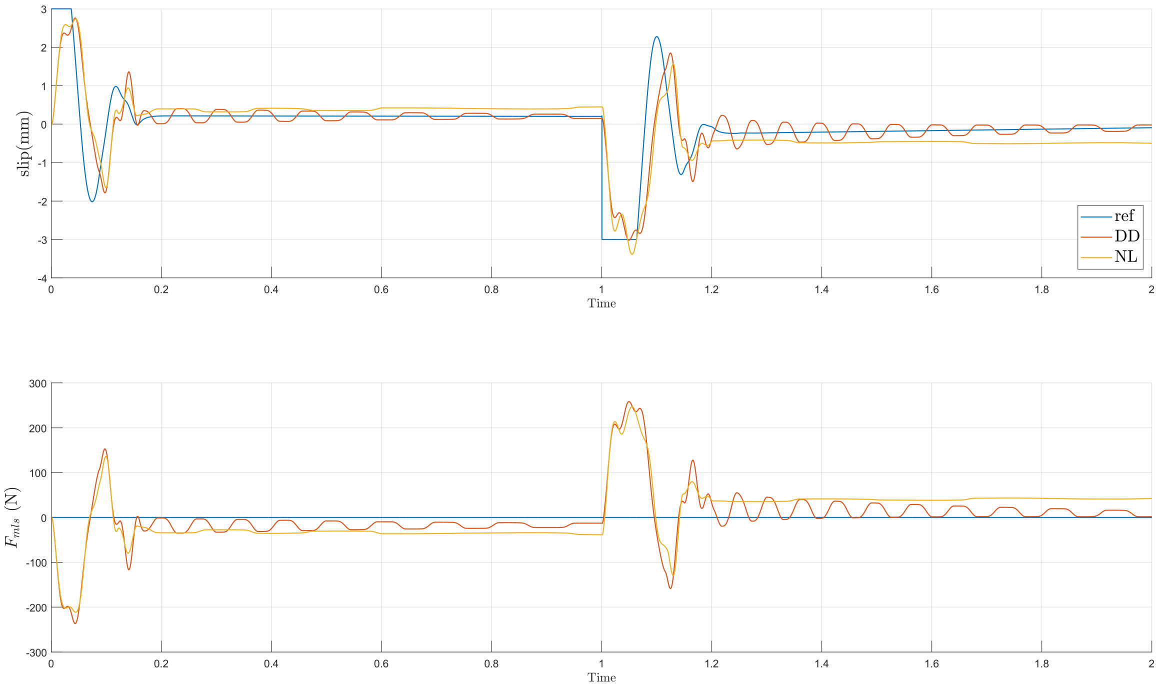

Figure 6.15: Slip response to reference trajectory with slip controller.

6.5 Calculated Current Controller

Similarly to the slip controller, a controller was developed in order to directly control the force applied to the MLS instead of attempting to determine the force based on the position. This is done by calculating the current necessary to apply the torque corresponding to the desired force while considering the friction in the rotor system.

$$i_{q_{ref}} \approx \frac{4\frac{\gamma}{2\pi}F_{ref} + B_{vr}\dot{\theta} + F_{sr}sgn(\dot{\theta})}{3p\lambda_{pm}} \tag{6.40}$$

The reference force is determined by a hand tuned PID controller driven by the translator position error.

The translator position can be seen in figure 6.16 to stably move to the reference however, a reasonably large steady state error is present. Various methods of compensating for this error were tested, however, they generally caused either further oscillation in the system or a significantly slower response time. From this test however, it can be seen that this method achieves a reasonably fast response though the oscillations prevent it from settling fully.

Under this form of control, the force is seen to have many oscillations as the current is not calculated from the translator position as well. The force generally follows the reference curve generated by the PID controller and does not overshoot at high values which is important to the stability of the system.

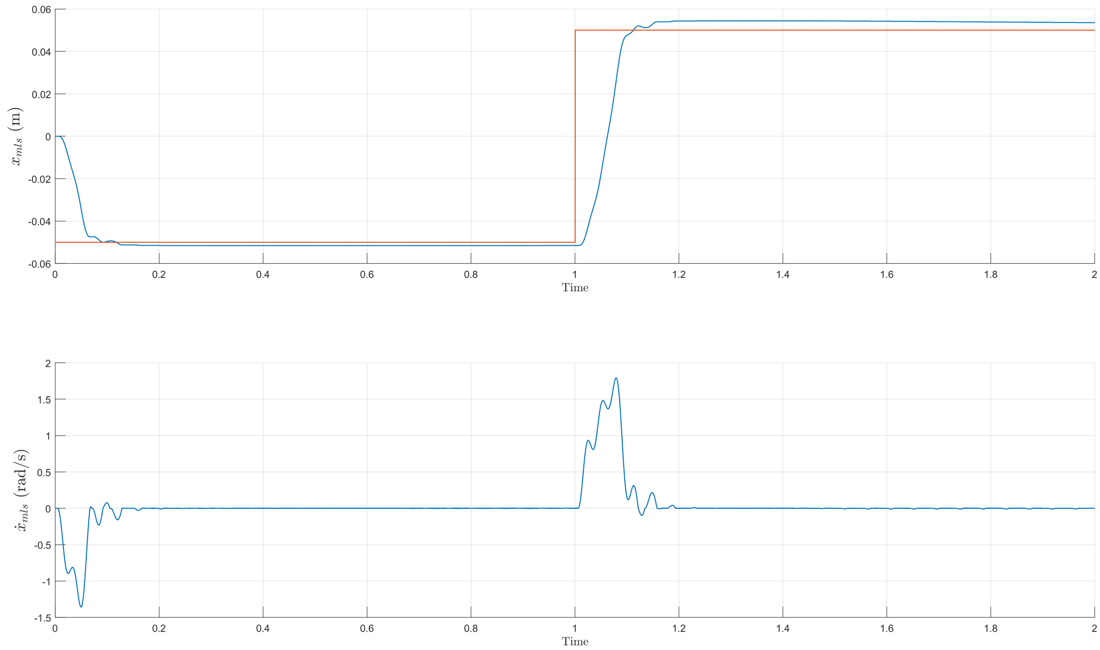

Figure 6.16: Translator dynamics compared to reference in calculated current controller.

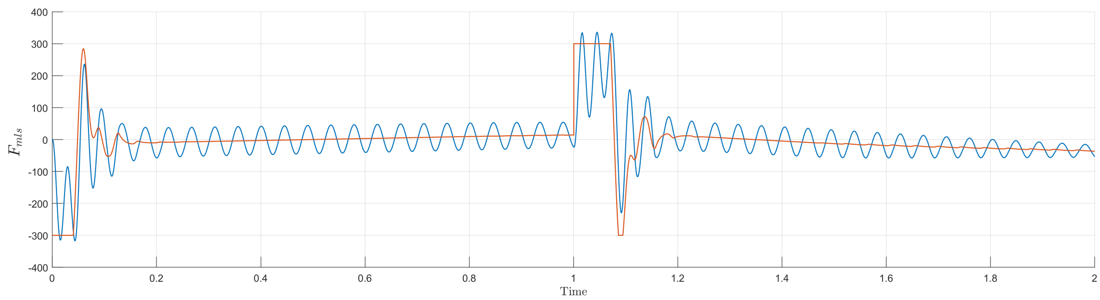

Figure 6.17: Force dynamics compared to reference in calculated current controller.

6.6 Linear Quadratic Regulator

As the slip controller suffered from the phase shifts and oscillations of the many states, the next logical step is to consider all of the mechanical system states in the controller. Linear quadratic regulators utilize the state space model of the system as well as a weighting matrix to develop a gain matrix for the stabilization of a plant. The model used for the development of the LQR controller is the mechanical system reduced state space model.

$$\dot{x}_{mech} = \boldsymbol{A}_{mech} x_{mech} + \boldsymbol{B}_{mech} u \tag{6.41}$$

$$y = \boldsymbol{C}_{mech} x_{mech} \tag{6.42}$$

$$x_{mech} = \begin{bmatrix} \theta_r & \dot{\theta}_r & x & \dot{x} \end{bmatrix} \tag{6.43}$$

The LQR gain K_r is calculated through an optimization problem, defined around the settling of the system to zero from a nonzero initial state, through minimization of the cost function[13]:

$$J_r = \int_0^{\infty} (x(t)^T Q x(t) + u(t)^T R u(t)) dt \tag{6.44}$$

From this optimization problem, the optimal solution may be found as:

$$u(t) = -K_r x(t) \tag{6.45}$$

$$K_r = R^-1 B^T X \tag{6.46}$$

And where X is the algebraic solution of the Ricatti equation:

$$A^T X + XA - XBR^{-1}B^T X + Q = 0 \tag{6.47}$$

The matrices Q and R are the state weighting and the cost weight matrices respectively. In the case of the reduced system, the Q and R matrices may be defined as:

$$Q = \begin{bmatrix} Q_\theta & 0 & 0 & 0 \\ 0 & Q_{\dot{\theta}} & 0 & 0 \\ 0 & 0 & Q_{x_{mls}} & 0 \\ 0 & 0 & 0 & Q_{\dot{x}_{mls}} \end{bmatrix} \quad R = \begin{bmatrix} R_{i_q} \end{bmatrix} \tag{6.48}$$

In this case, the value of each entry in the Q matrix is the weight of how important the control of each state is. If the MLS was the only state to be controlled, the value of $Q_{x_{mls}}$ would be very high and all of the other values would be very low or zero. The value(s) in the R matrix are input-cost weights, which are determined based on factors like actuation dynamics, saturation, and power considerations. In this case, where there is only one input, the R matrix may be combined into the Q matrix.

$$Q = \begin{bmatrix} \frac{Q_\theta}{R_{i_q}} & 0 & 0 & 0 \\ 0 & \frac{Q_{\dot{\theta}}}{R_{i_q}} & 0 & 0 \\ 0 & 0 & \frac{Q_{x_{mls}}}{R_{i_q}} & 0 \\ 0 & 0 & 0 & \frac{Q_{\dot{x}_{mls}}}{R_{i_q}} \end{bmatrix} \quad R = [1] \tag{6.49}$$

The linear quadratic regulator gain is calculated through the use of the $lqr()$ command in Matlab.

6.6.1 Direct Drive Model LQR

The linear quadratic regulator is initially developed on the direct drive model in order to prevent the complication of tuning the controller on a nonlinear response. For the purpose of tuning the controller, each state is considered. The highest importance state is the MLS translator position as it is the controlled variable. The second most important state is the rotor position, as it should follow the MLS translator. The third most important state is the linear velocity of the MLS translator as oscillations should be minimized. Similarly, the least important state is the rotor velocity which should settle to zero, however it should also have the opportunity to move rapidly to apply force to the translator. From this, and applying the MLS "gear ratio", the preliminary Q matrix values may be set as:

$$Q_{x_{mls}} = \frac{1000 \cdot 2\pi}{\gamma} \tag{6.50}$$

$$Q_\theta = 100 \tag{6.51}$$

$$Q_{\dot{x}_{mls}} = \frac{10 \cdot 2\pi}{\gamma} \tag{6.52}$$

$$Q_{\dot{\theta}} = 1 \tag{6.53}$$

An initial test of these values finds that the weights are too low compared to the desired settling timeframe, thus the values are increased.

$$Q_{x_{mls}} = \frac{10000000 \cdot 2\pi}{\gamma} \tag{6.54}$$

$$Q_\theta = 100000 \tag{6.55}$$

$$Q_{\dot{x}_{mls}} = \frac{1000 \cdot 2\pi}{\gamma} \tag{6.56}$$

$$Q_{\dot{\theta}} = 10 \tag{6.57}$$

With these values, a more acceptable performance is seen.

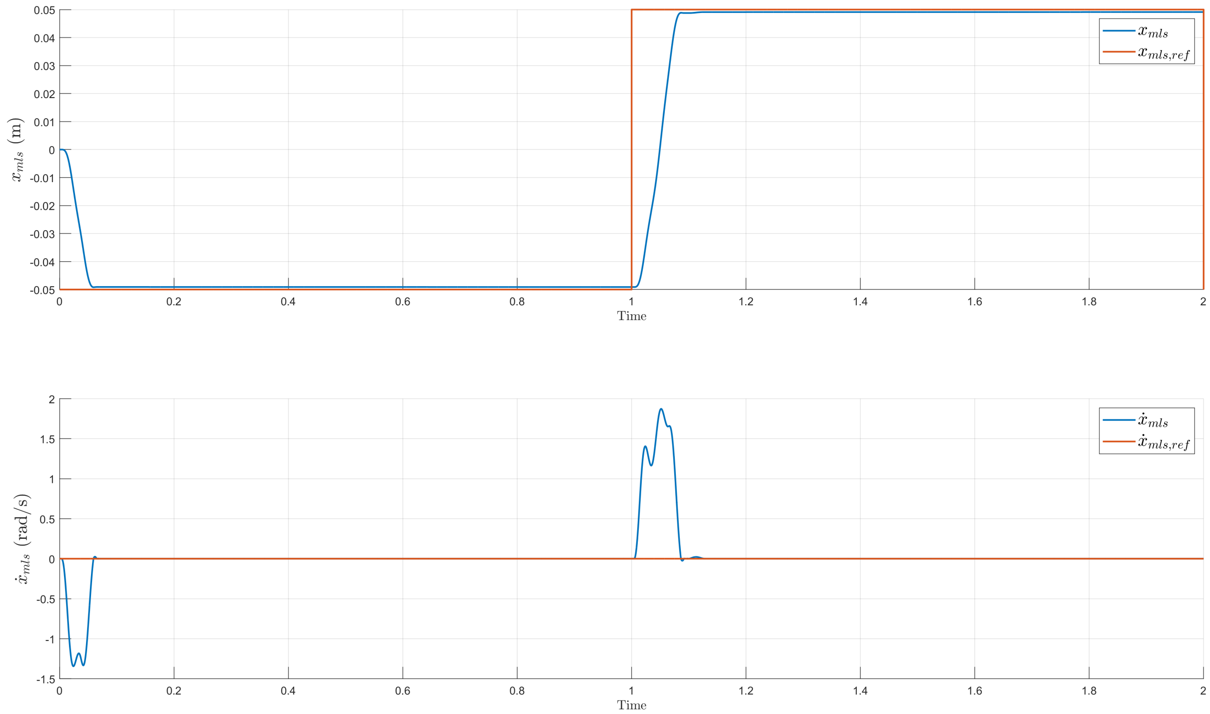

Figure 6.18: Translator settling dynamics under LQR on direct drive model.

In figure 6.18, the MLS translator can be seen to converge rapidly to the reference value without many oscillations, however the translator never reaches the reference due to the static friction in the system. The translator velocity is relatively stable with only minor oscillations while traveling and settles to zero rapidly. Though the translator does not reach the reference value, it can be said to settle at 0.056 seconds for the 5cm step and after 0.116 seconds for the 10 cm step. The MLS barely makes it inside the 1mm settling region and does not converge further from there.

The rotor position settles very rapidly to the reference and with very few oscillations. As the rotor position is non-critical, relaxing this parameter could improve acceleration and deceleration performance. The velocity response shown in figure 6.19, when compared to that of the MLS translator shows the expected behavior where the rotor leads the translator. The rotor velocity as well settles to zero rapidly and smoothly.

The force applied to the MLS and the slip associated with it can be seen to oscillate a lot as well as peaking above 480N which is not realizable in the nonlinear system.

The current controllers work well in the control of the system and follow the reference produced by the LQR controller well. It can be seen that, while the current is saturated occasionally, the magnitude of

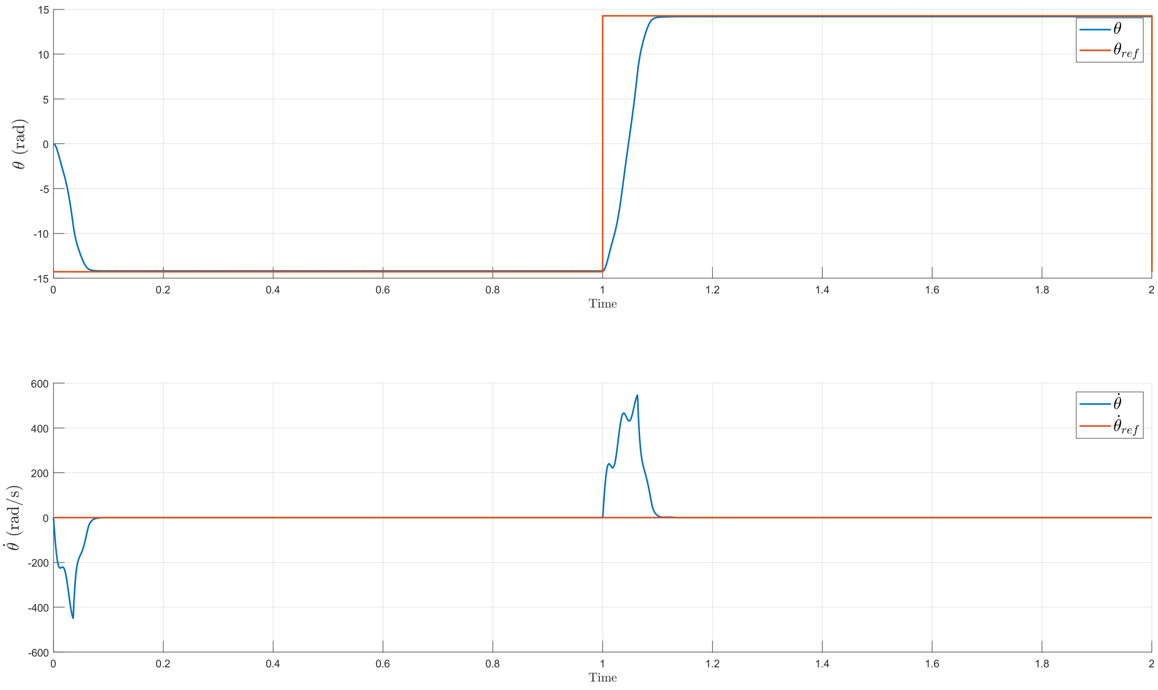

Figure 6.19: Rotor dynamics under LQR on direct drive model.

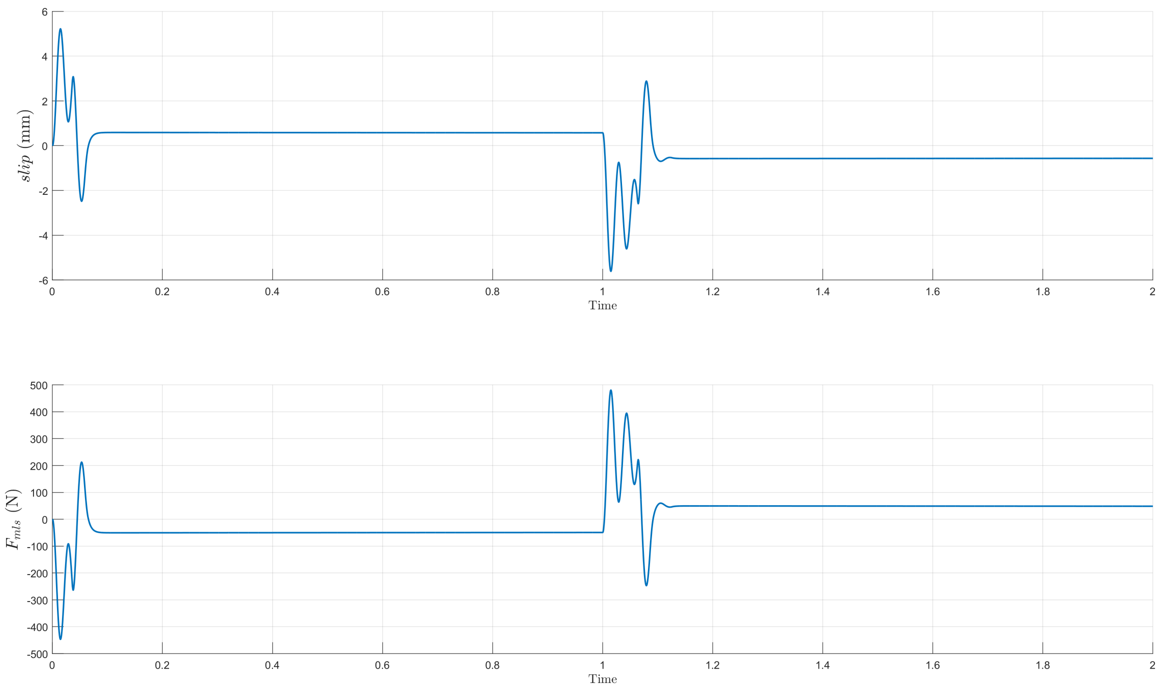

Figure 6.20: Slip and force dynamics under LQR on direct drive model.

the saturation is not high and does not last long.

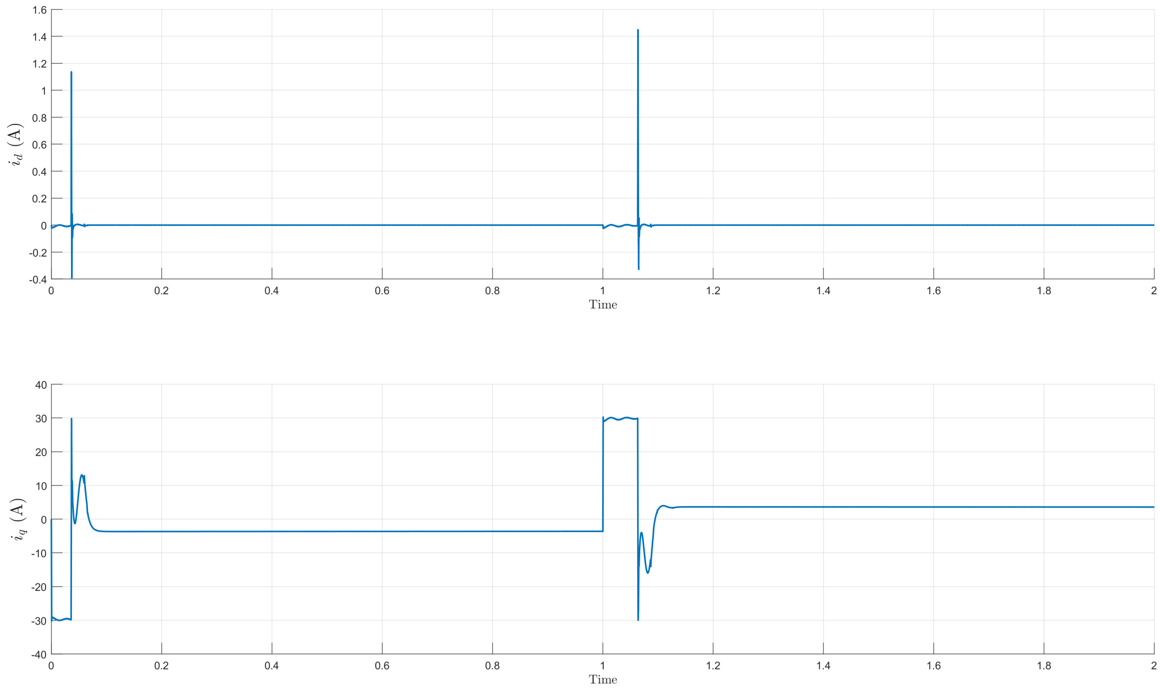

Figure 6.21: Current dynamics under LQR on direct drive model.

Static Friction Feed-Forward

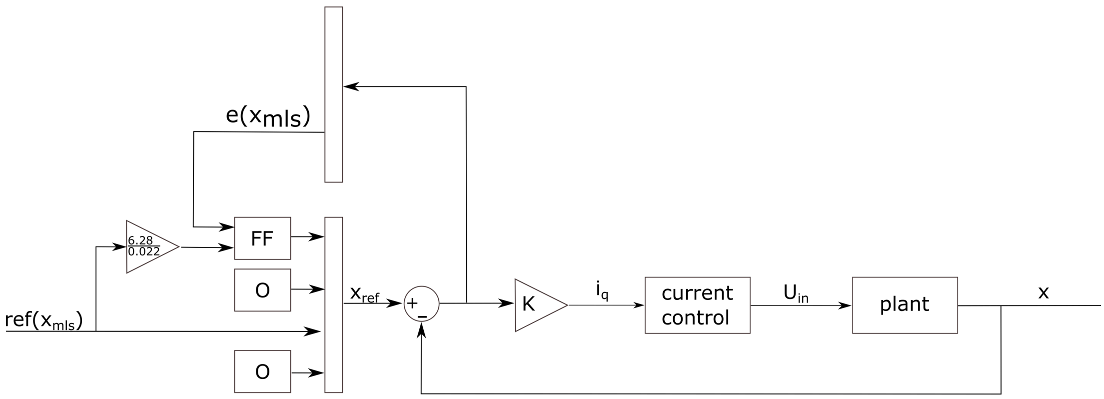

Figure 6.22: Implementation of LQR gain in control scheme.

In order to solve the steady-state error seen in the translator response, compensation for the static friction is fed forward into the rotor reference. As the rotor dynamics determine the behavior of this compensator, it makes sense to directly feed the compensator in to the rotor reference. The magnitude of the compensator value is determined by the slip necessary for the static friction to be compensated for, which in this case is 0.6mm. the value is slightly increased in order to additionally assist with the static friction in the rotor when there are such small errors.

$$\theta_{ref} = \frac{2\pi}{\gamma}\left(x_{mls_{ref}} + 0.0007sgn(e_{x_{mls}})\right) \tag{6.58}$$

When tested with the static friction compensation, the MLS position can be seen to settle to the reference with very little of the previous steady-state error present. The MLS linear velocity does not appear to have any extra oscillations due to the extra excitation caused by the discontinuous compensator. The translator is seen to have a 5cm settling time of 0.053 seconds and the 10cm step settling time of 0.86 seconds. Again the force applied is seen to exceed the $300N$ the tested system is capable of, thus the times are representative.

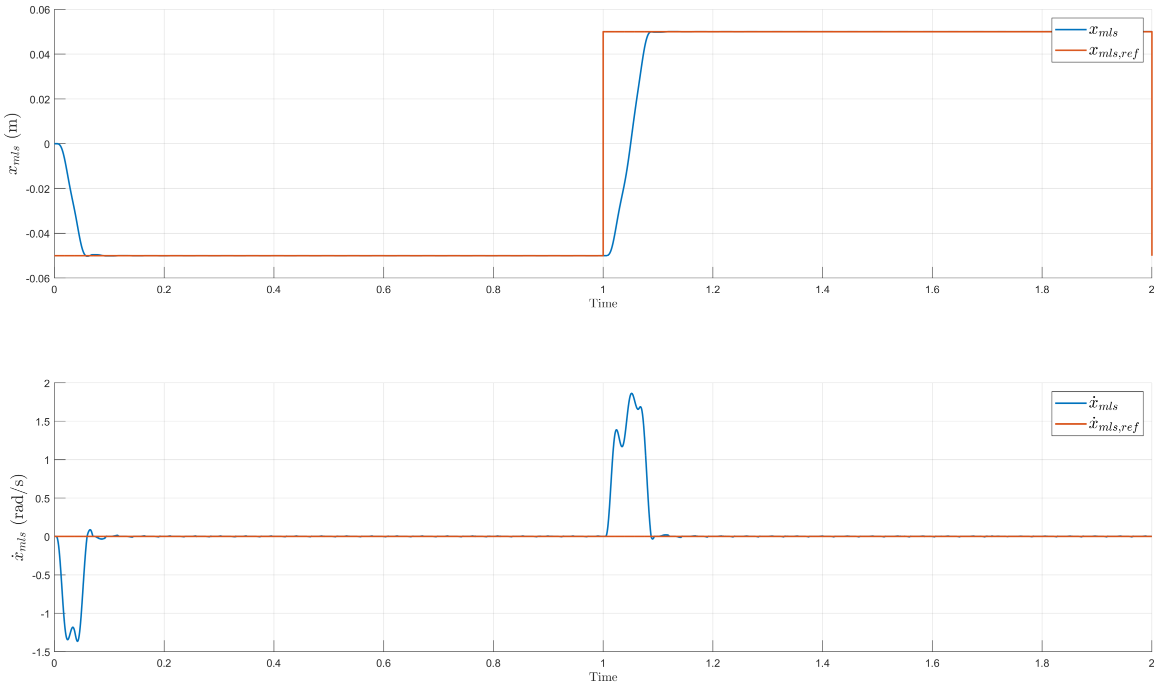

Figure 6.23: Translator settling dynamics under LQR with feed-forward on direct drive model.

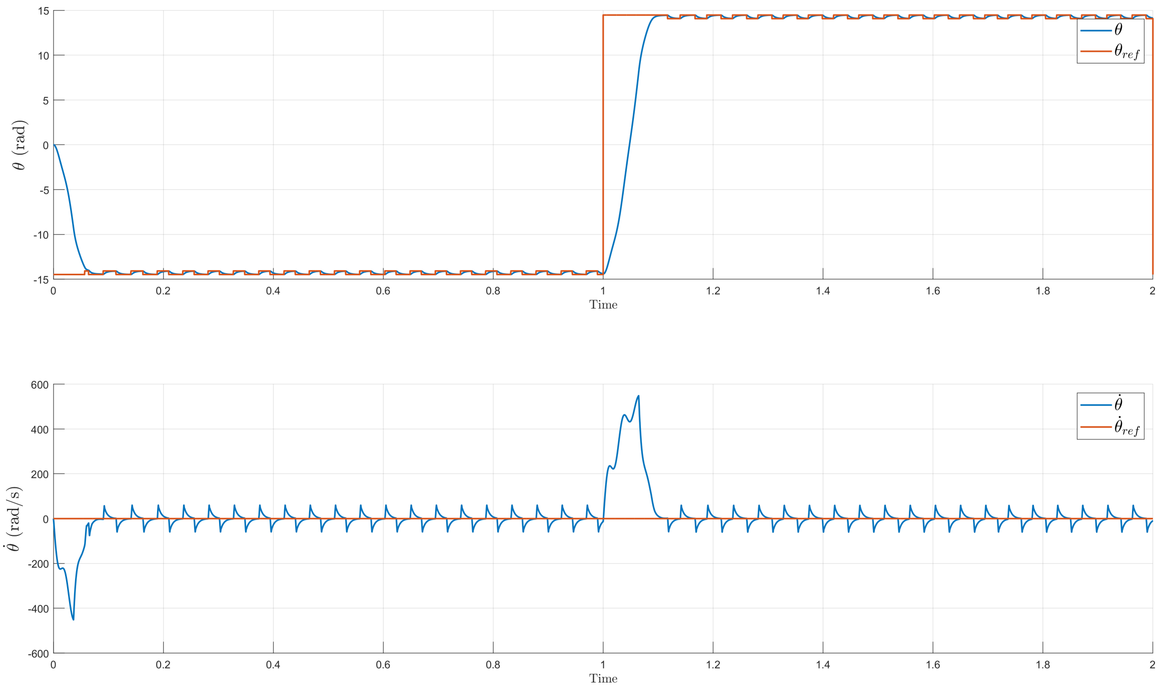

Figure 6.24: Rotor dynamics under LQR with feed-forward on direct drive model.

As seen in figure 6.24, as the MLS crosses the reference value, the compensator switches direction and the rotor position begins to oscillate. The velocity can be seen to take around 0.2 seconds to settle and then switch direction again. This suggests that the current implementation is only fitting for longer term steady state errors, and the accuracy can only be relied on accurately within 1mm of the target value if speed is of necessity. Looking at the high speed dynamics in the velocity, the rotor moves much faster when the reference is changed than most of the settling time thus the compensation could potentially act much quicker. Increasing the rotor control weight, R_θ, however prioritizes the rotor too much over the translator position. A solution to this could come in the form of an alternative controller gain matrix while the MLS and rotor are in the nearby region to the reference or a fully discontinuous controller in the same region.

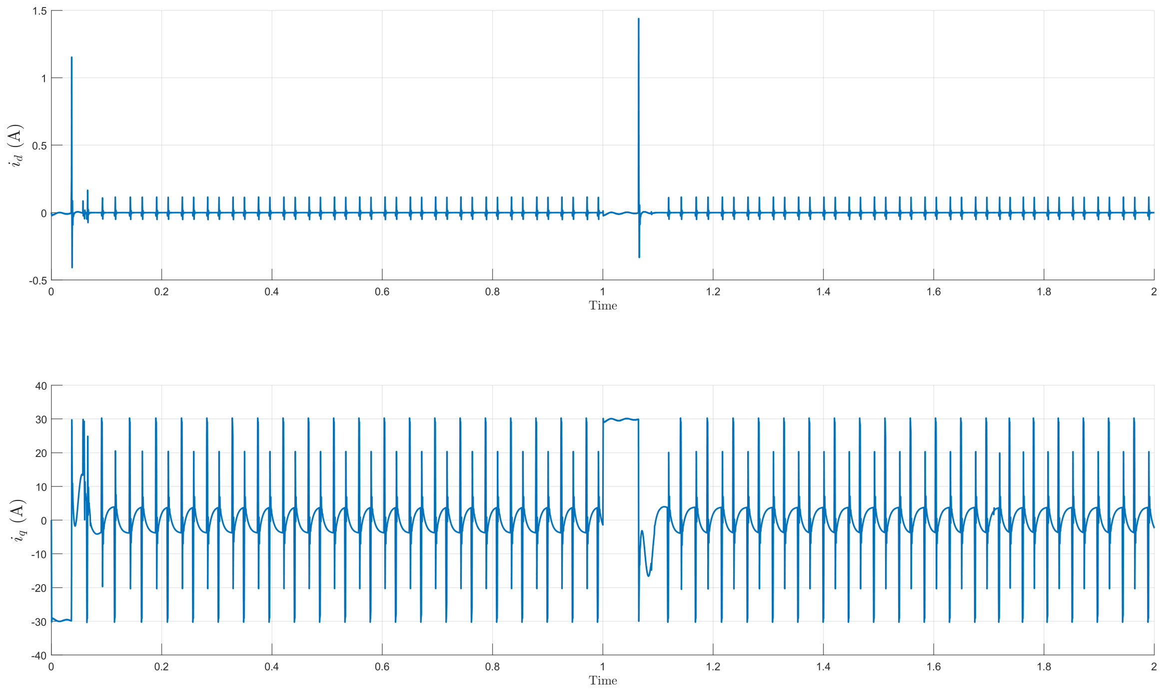

Figure 6.25: Current dynamics under LQR with feed-forward on direct drive model.

The currents, in figure 6.25 can be seen to be much more noisy when the static friction compensation is implemented, however, the transients are not as discontinuous as they appear, thus the system does not appear to be over driven by the controller.

6.6.2 Nonlinear Model LQR

The Controller is then applied to the nonlinear system model where the MLS has a sinusoidal spring constant.

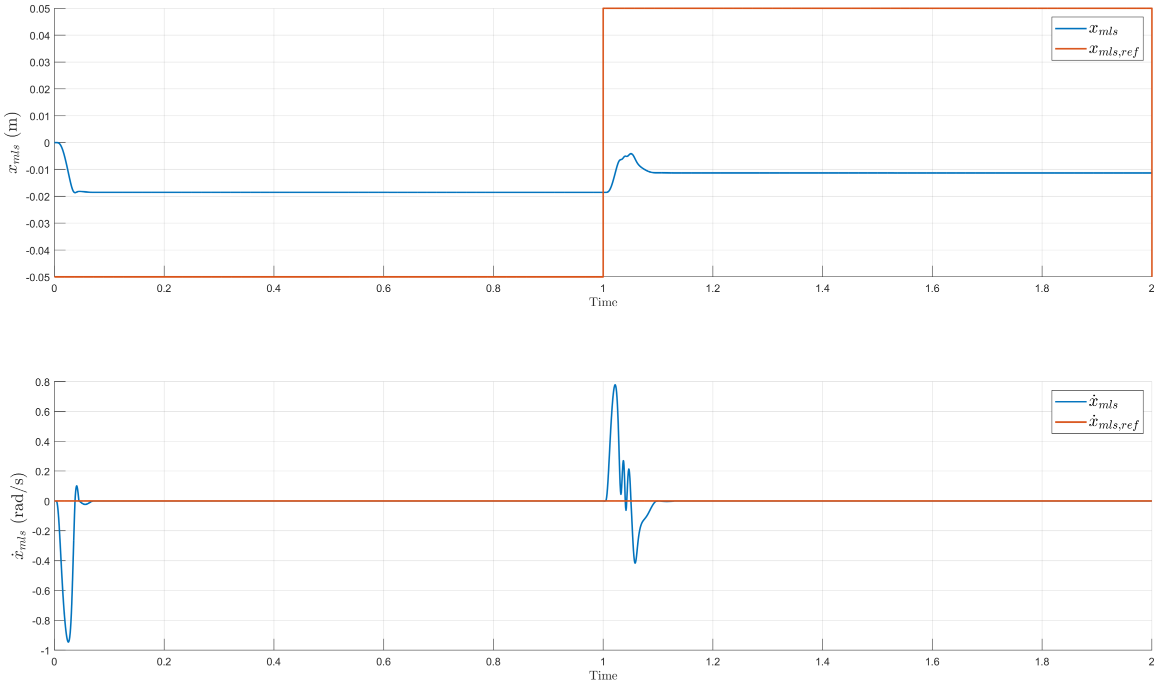

Figure 6.26: Translator dynamics under LQR with feed-forward on nonlinear model.

In this situation, figure 6.26, the translator can be seen to initially get agitated before a slip fault occurs. The same situation occurs with the larger step, however the fault occurs across multiple periods of the MLS causing the further oscillation in the MLS velocity.

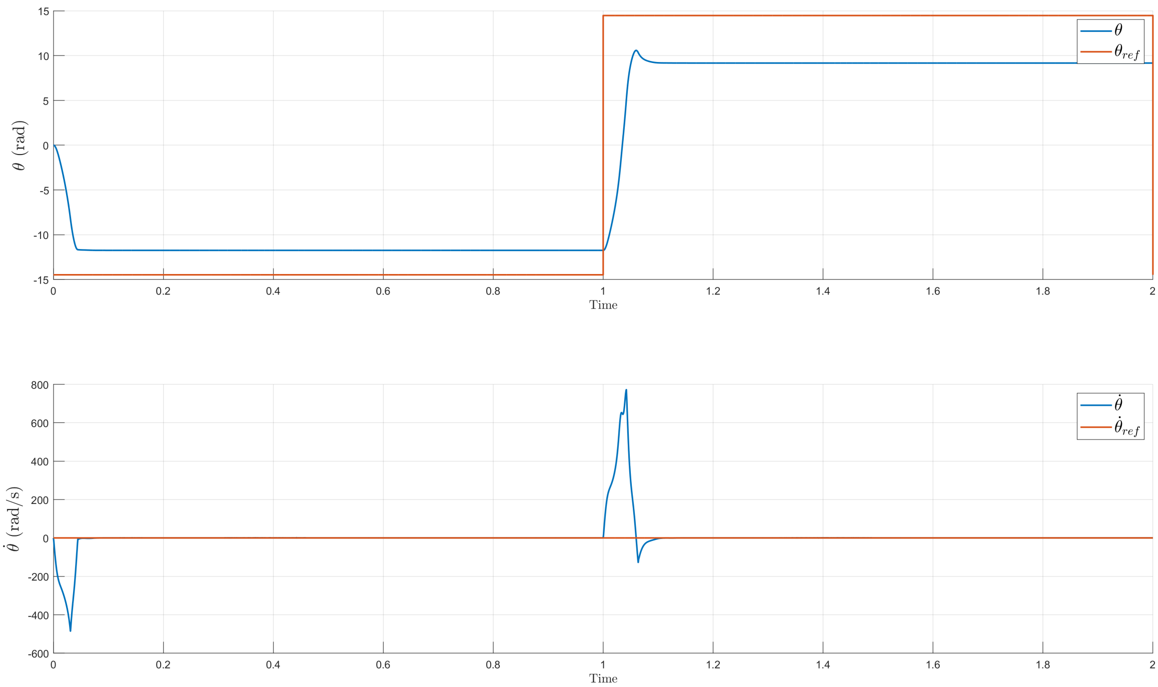

Figure 6.27: Rotor dynamics under LQR with feed-forward on nonlinear model.

The rotor is seen in figure 6.27 to move further towards the reference, however, due to the nature of the LQR gain, it does not move further as the lack of movement in the MLS is reducing the controller output.

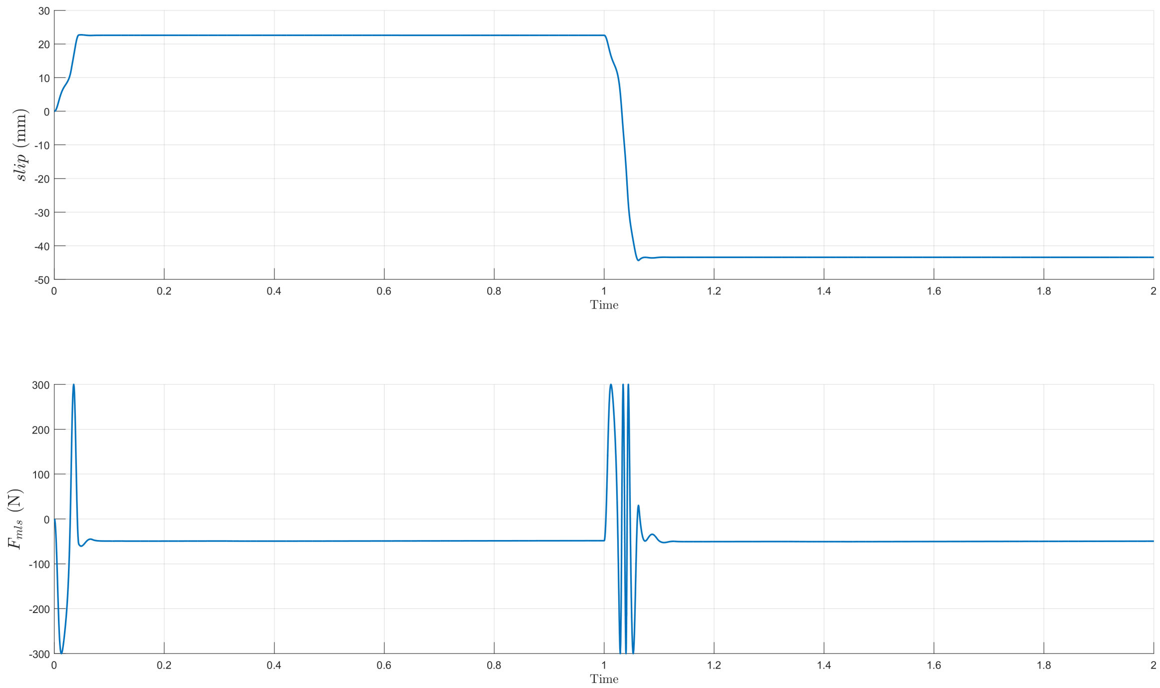

Figure 6.28: Slip and force dynamics under LQR with feed-forward on nonlinear model.

The amount of slip and the number of slip faults can be seen in figure 6.28. These faults could potentially be improved on by adapting the rotor reference to the new period of the MLS it has slipped into, however, this does not directly address the source of the problem.

Slip Fault Prevention

In order to adapt to the non-linearity of the MLS, the sensitivity of the control to the error must be reduced as the value of the slip approaches the critical value. This can be done through gain scheduling which would also allow for further increasing the gain when compensating for static friction. Another method is to simply scale the output of the controller based on the slip position. This is the method used here as it is very simple to implement and as the exact value of the slip is harder to determine due to the lack of translator position feedback.

The scaling methods tested are:

$$K_{s,cos} = cos(slip\frac{2\pi}{\gamma}) \tag{6.59}$$

$$K_{s,2} = \frac{(\frac{\gamma}{4})^2 - slip^2}{(\frac{\gamma}{4})^2} \tag{6.60}$$

$$K_{s,3} = \frac{(\frac{\gamma}{4})^3 - abs(slip^3)}{(\frac{\gamma}{4})^3} \tag{6.61}$$

The scaling curves created by these functions can be seen in figure 6.29. The cosine function which would initially make intuitive sense as the spring is sinusoidal can be seen to taper the control input off relatively quickly meaning that very little of the operating range will be receiving $> 90\%$ of the control input. The square scaling factor has a similar but slightly higher curve whereas the cubic scaling factor maintains a high factor for much longer and tapers off more sharply as the peak force is approached.

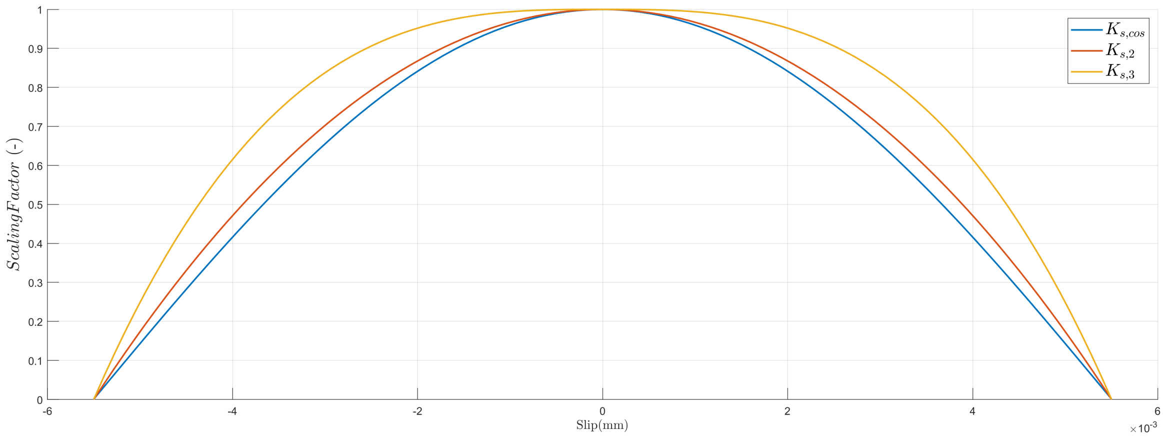

Figure 6.29: Scaling curves of various methods tested for slip fault prevention.

When the system is tested with the above scaling methods, the behavior becomes much more predictable and the position settles much more effectively to the reference.

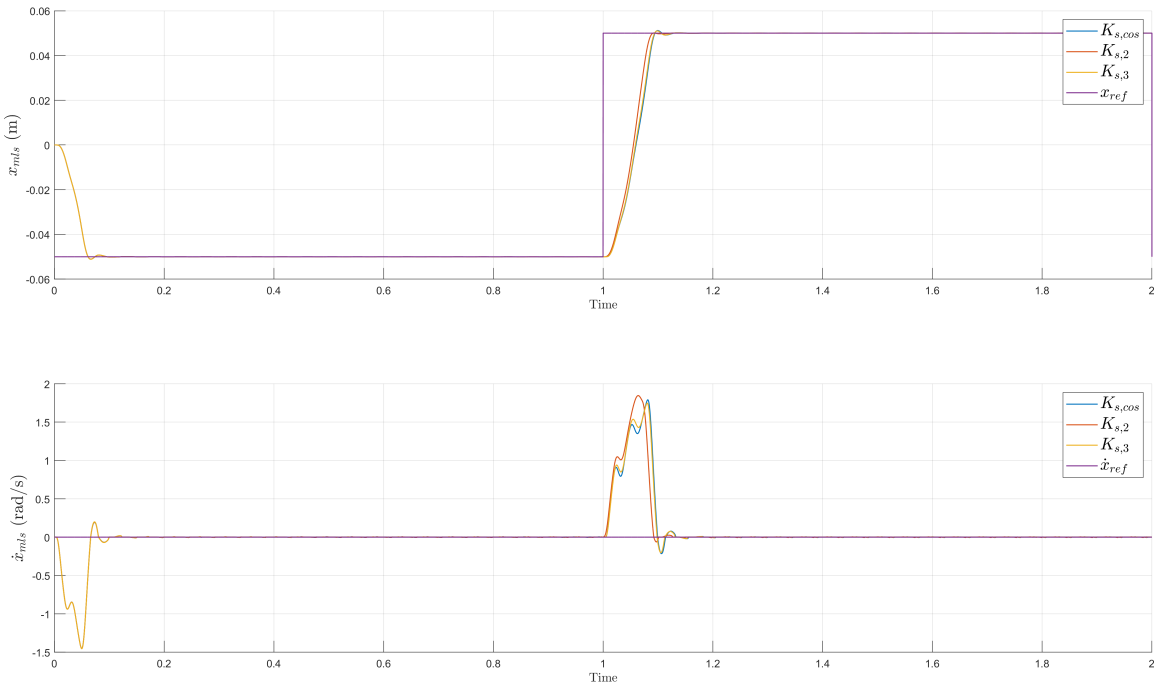

Figure 6.30: Translator settling dynamics under LQR with feed forward and controller scaling.

Each of the methods can be seen to have slightly different settling dynamics. For the small step, the three methods all behaved the same and settled at the same time. For the large step, each method settled at a different rate and had a different overshoot. They all settled reasonably quickly, however only the quadratic scaling method did not overshoot by more than 1mm. The specific values may be seen in table 6.2.

	T_s(5cm)	T_s(10cm)	OS(5cm)	OS(10cm)
$K_{s,cos}$	0.067sec	0.10sec	1.1mm	1.1mm
$K_{s,2}$	0.067sec	0.087sec	1.1mm	0.3mm
$K_{s,3}$	0.067sec	0.092sec	1.1mm	0.98mm

Table 6.2: LQR performance with various controller scaling methods.

Overall the quadratic scaling factor was the most effective with the lowest settling time. This settling time is 0.01 seconds higher than the 'ideal' value found previously.

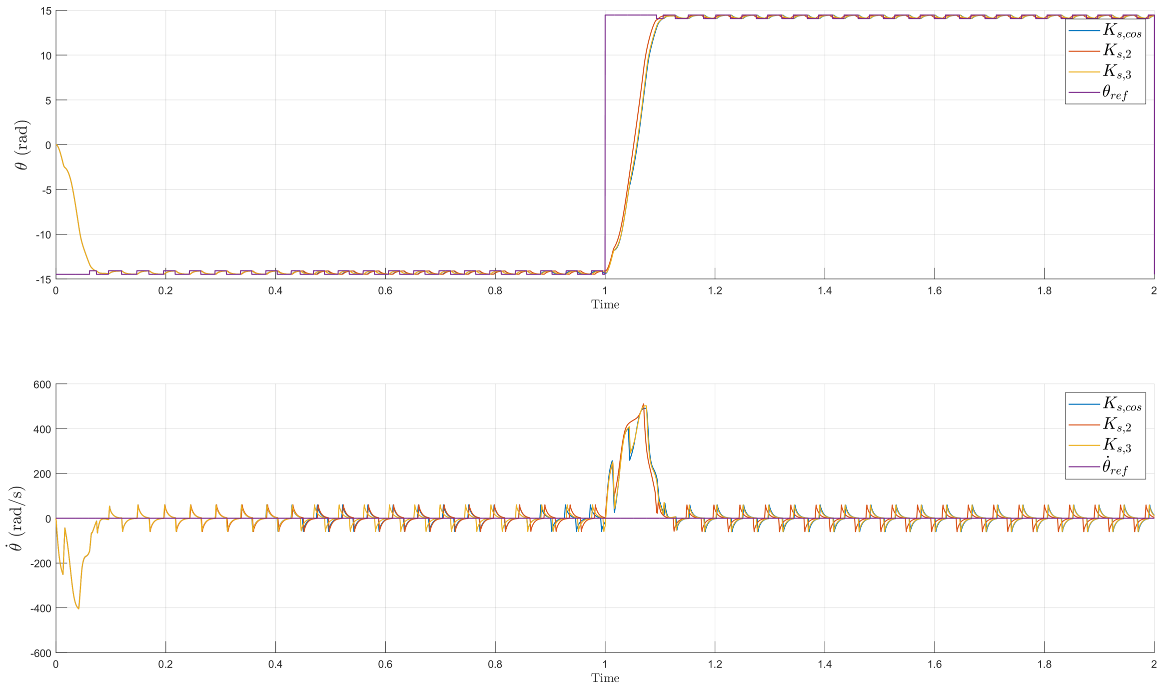

Figure 6.31: Rotor dynamics under LQR with feed forward and controller scaling.

The rotor behavior can be seen to be marginally different between two of the scaling methods, however, the quadratic method includes one less melocity oscillation which increases the average speed. The dynamics of the friction compensation remain identical to previously as can be expected.

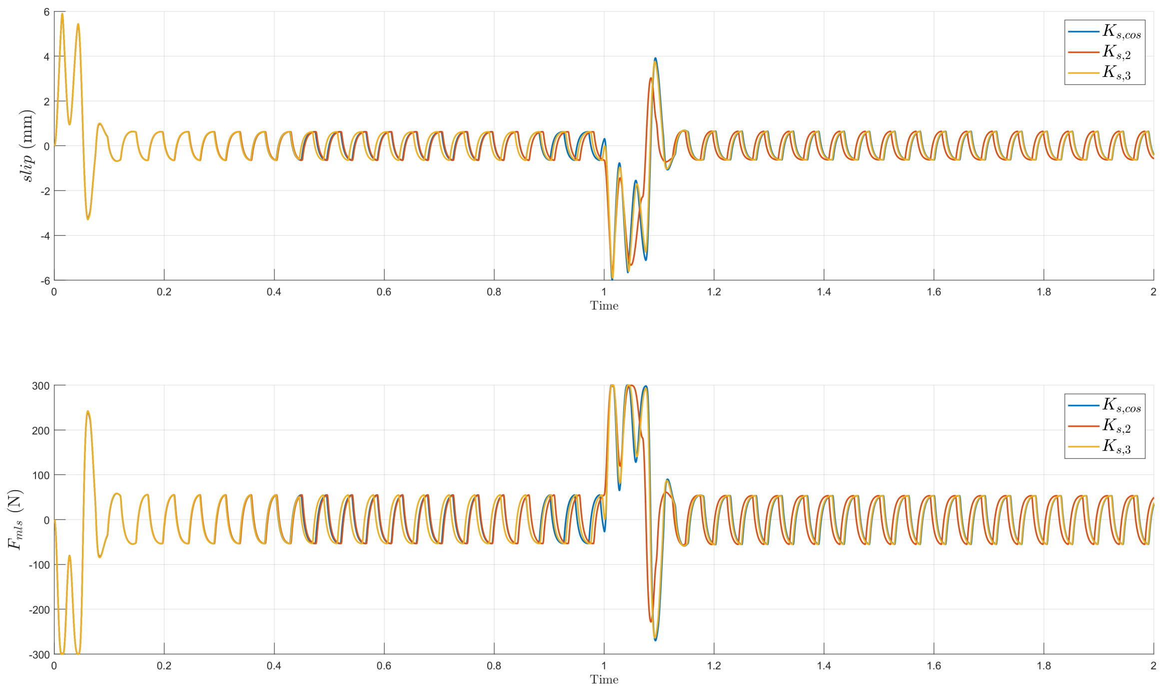

Figure 6.32: Force dynamics under LQR with feed forward and controller scaling.

In viewing the values of the slip and the MLS force, the dynamics can be seen to reach the maximum slip and while the slip passes the peak, it rapidly returns to the desired stable region.

6.6.3 Discrete LQR

In order to test the controller when the control loop is discretized, the controller gain is recalculated with the same parameters with a discrete form of the optimization problem. This is done with the $lqrd()$ function in Matlab with an assumed time step of 1kHz. In addition, the state feedback is fed into the controller through a zero order hold of the form[14]:

$$T_s = \frac{1}{1kHz} \tag{6.62}$$

$$\bar{e}(t) = e(t) - e\left(t - T_s floor\left(\frac{t}{T_s}\right)\right) \tag{6.63}$$

Furthermore, as the amount of state feedback necessary for effective control of the system is unknown, various extents of feedback reduction are simulated. A common factor for each of these methods is the use of a discrete time derivative, used on the state feedback when passed through the zero order hold.

$$\frac{dx(z)}{x(z)} = \frac{z-1}{T_s z} = \frac{1-z^{-1}}{T_s} \tag{6.64}$$

$$dx(z) = \frac{(1-z^{-1})x(z)}{T_s} = \frac{x(z)-x(z-1)}{T_s} \tag{6.65}$$

Full State Feedback

The first scenario tested is the case where all states are measured perfectly and the only consideration tested is the sampling time introduced by the zero order hold. This test will be referred to by ZOH.

Rotor Projected Position

The second and third scenarios tested include the zero order hold as well, however the only direct measurement will be the rotor position, sampled to have 24 measurement points per rotation. The angular velocity and the linear velocity will be calculated through discrete derivatives. The translator position will be estimated by:

$$\hat{x}_{mls} = \theta_r \frac{\gamma}{2\pi} \tag{6.66}$$

$$\hat{x}_{mls,c} = \left(\theta_r + 0.2sgn(e_x(t-1))\right)\frac{\gamma}{2\pi} \tag{6.67}$$

These are referred to as rotor projected position(RPP) and compensated rotor projected position($cRPP$). The RPP method simply assumes that the MLS is at a position of zero slip at all times. The compensated RPP assumes the same, however the position is offset by the feed forward compensation introduced in section 6.6.1, which allows for the static friction dead zone to be adjusted for.

Additional Translator Sensor

The fourth and fifth scenarios tested are with the addition of position sensing on the MLS translator. The two cases tested are where a 1mm measurement resolution is possible(ATS_1) and where a 0.1mm resolution is possible(ATS_{01}). In these cases, the velocities will again be calculated through discrete derivatives.

State Estimation

The sixth, seventh and eighth methods take into account the linear model of the system in order to estimate the exact positions with a higher resolution than possible with just the sensors. The first method utilizes a state estimator on the rotor position in combination with the RPP mentioned previously($RSE + RPP$). The second method utilises just a translator state estimator(TSE). The third method uses a combined state estimator for all the states(CSE). Further details on the developed state estimators are present in chapter 7.

Testing of State Feedback Methods

The LQR controller is tested with each of the state feedback methods mentioned.

In figure 6.33, each of the methods can be seen to control the rotor to the reference value. A few of the responses behave in a different manner which may be of note. The combined state estimator can be seen to have a lower speed initial response and larger oscillations once the reference has been reached. The rotor state estimator with RPP can be seen to respond very rapidly and reach the highest peak speed, however this is due to a slip fault occurring. ATS_1, ATS_01, $cRPP$, and TSE all behave similarly in this scenario with only minor differences.

In figure 6.34, some of the estimators can be seen to fail significantly at controlling the translator position. The rotor state estimator with RPP encounters a clear slip fault due to the inability to scale the controller output based on the slip as no slip value is generated. The compensated RPP is also seen to slip, however in this case, the compensation amount is enough to prevent the slip fault in the upwards direction, though this cannot be relied on. The full state feedback, and both instances of the additional sensor behave very well as can be expected with only minor variations in behavior. The combined state estimator can be seen to have a very slow response to the 5cm step and then the fastest response to the 10cm step. This is likely due to the tendency of this estimator to overestimate the translator position which causes a lower slip value to be considered in the control loop and thus larger oscillations. The translator state estimator does not have as much of an issue in either scenario though some oscillation is present.

Looking at the plots of slip and F_{mls} for the test scenario in figure 6.35, provides extra insight into the failures. From the slip, it can be seen that the combined state estimator experiences a slip fault and then recovers from it which explains the unusual behavior seen initially. The rotor state estimator with RPP experiences a similar slip fault but does not recover, and the rapid response it achieves with the large step includes another large slip fault. The slip fault of the $cRPP$ method is also seen. With the large step, the combined state estimator can be seen to hold very tightly to the peak of the force range which is very effective for the fast response but is worrying for the repeatability of the performance due to the under measurement of the slip. The translator state estimator appears promising in terms of force and slip dynamics as do the tests with additional translator sensors.

	T_s(5cm)	T_s(10cm)	OS(5cm)	OS(10cm)
FSF	0.058sec	0.089sec	0.8mm	0.8mm
ATS_1	0.059sec	0.093sec	0.2mm	0.6mm
ATS_{01}	0.58sec	0.11sec	0.4mm	1.3mm
$cRPP$	$--$	$--$	$--$	$--$
$RSE + RPP$	$--$	$--$	$--$	$--$
TSE	0.077sec	0.085sec	0.6mm	0.5mm
CSE	0.19sec	0.101sec	2.3mm	1.5mm

Table 6.3: Performance of each feedback method when combined with the developed LQR controller.

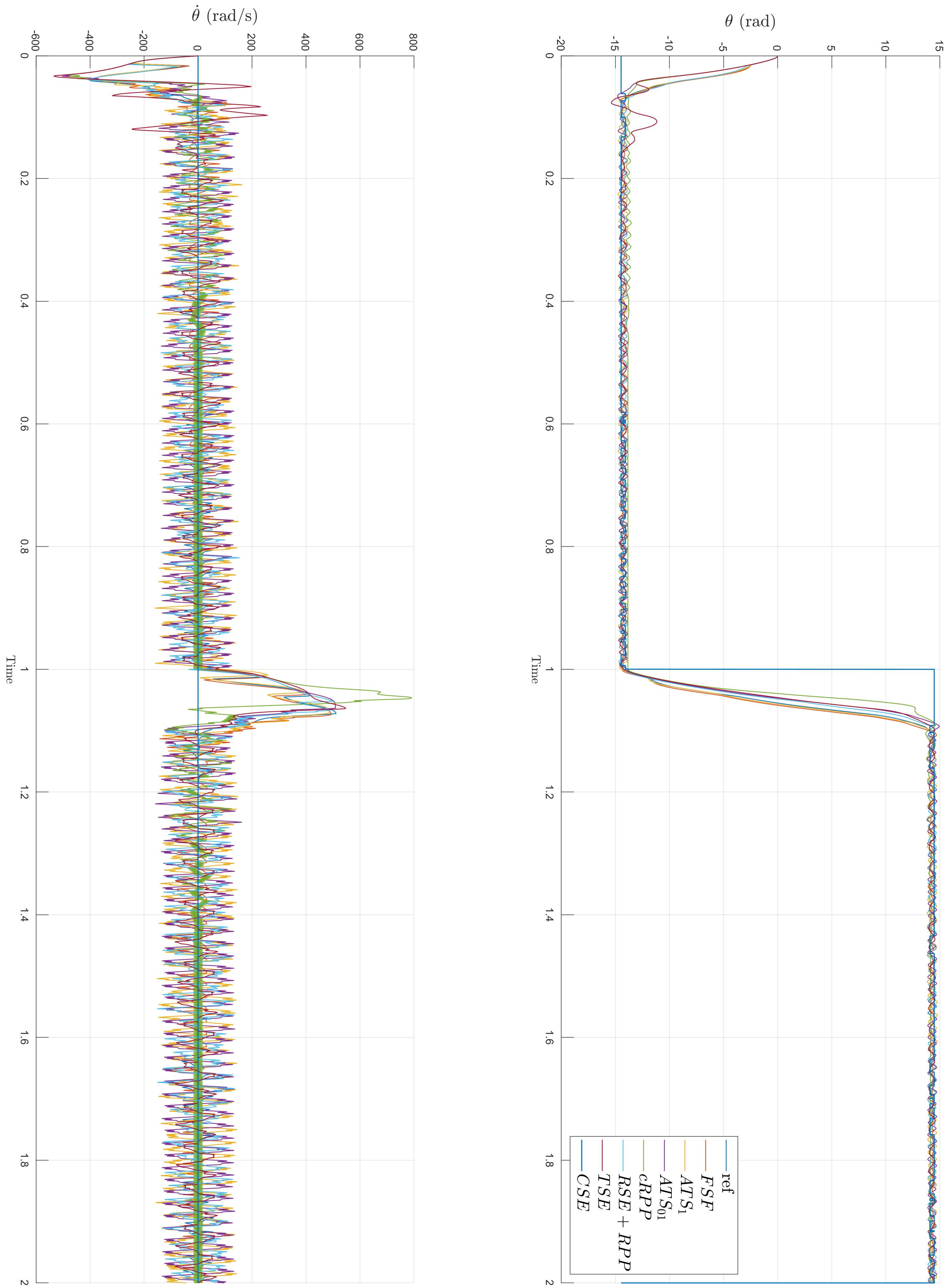

Figure 6.33: Rotor behavior when tested with various state feedback methods.

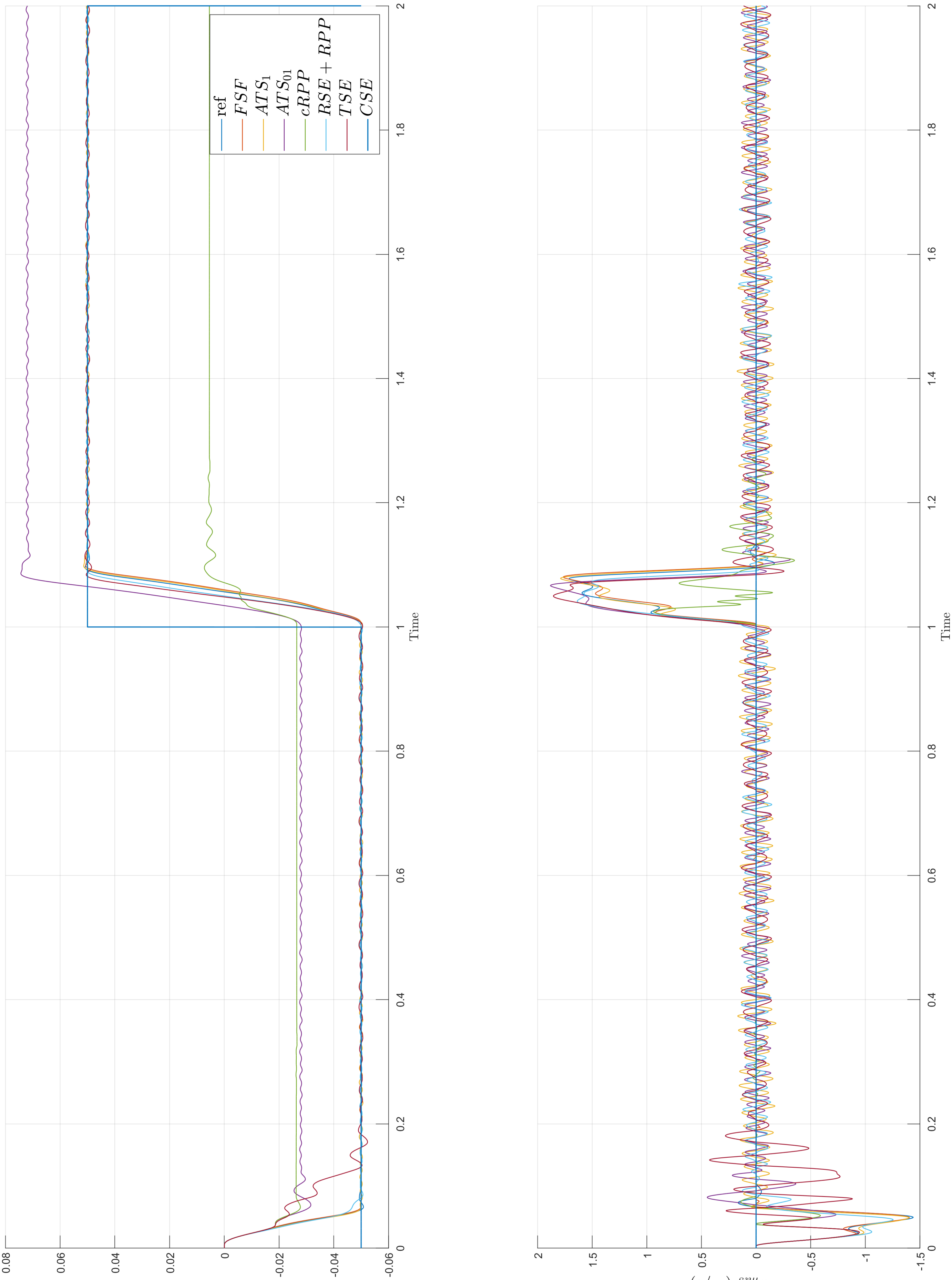

Figure 6.34: MLS translator behavior when tested with various state feedback methods.

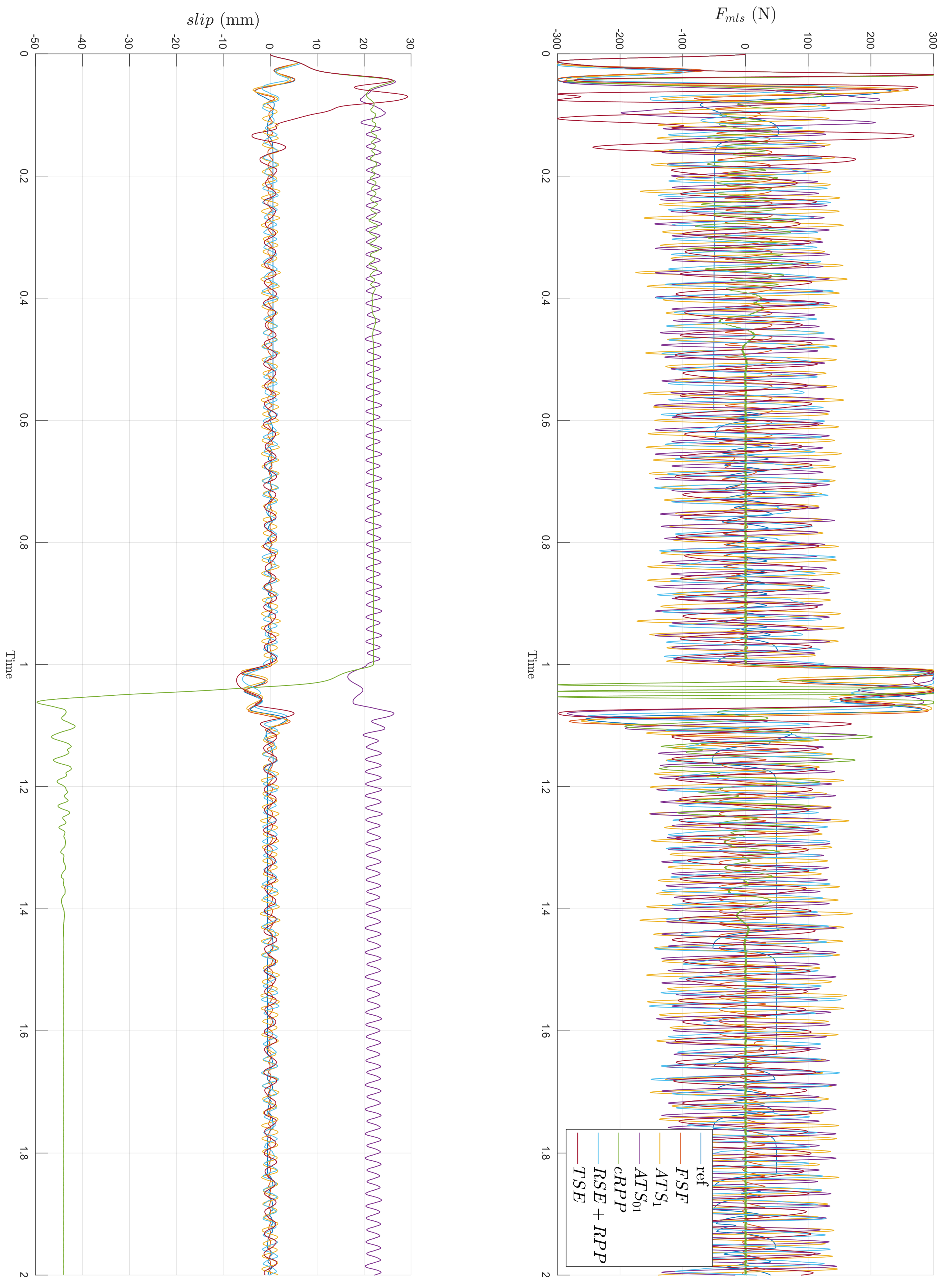

Figure 6.35: MLS force and MLS-rotor slip when tested with various state feedback methods.

6.7 Loading and Disturbance Rejection

For testing of the controller with an additional load and with disturbances added to the system, the ATS_{01} and TSE state estimation methods will be used as well as an additional ATS_{37} where six position sensors are added per period of the MLS force similarly to the hall effect sensors in the motor. The system is tested with a normally distributed white noise added to the translator force with a standard deviation of 9.5N. In order to test robustness to loading, the mass of the translator, set as 3kg in simulation and in the linear model, is increased to 2, 4, and 8 times the original value.

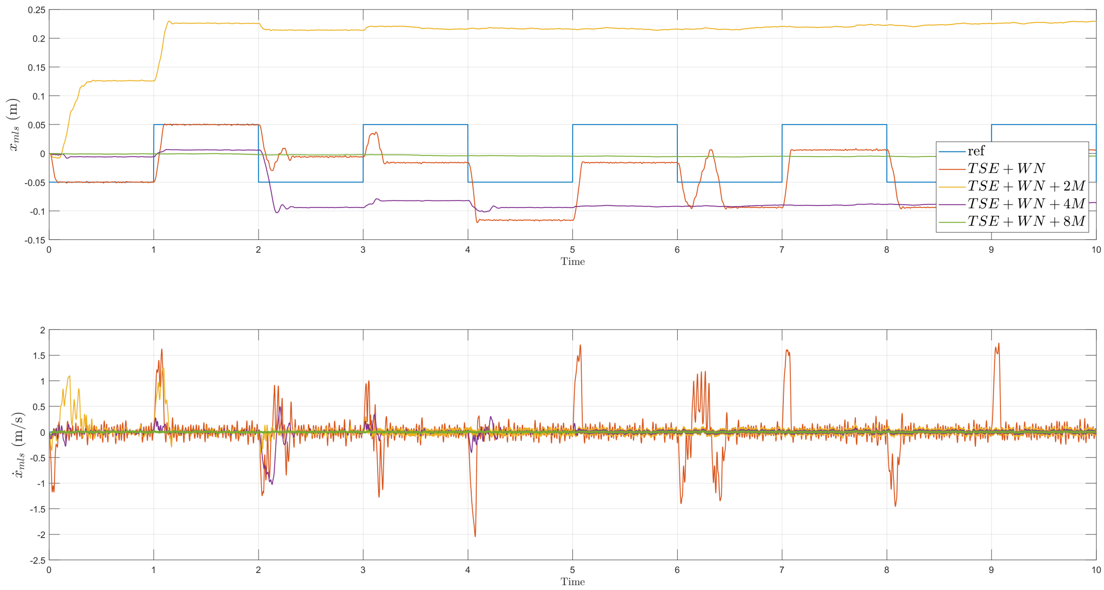

Figure 6.36: Translator behavior when controlled with different disturbances and state estimated position feedback.

When the control is tested with disturbances and translator state feedback through state estimation, seen in figure 6.36, the performance is found to be lacking. When only noise is added, the controller is effective for the first period, but does not maintain the performance across multiple steps. As further weight is added, the performance degrades further until, at eight times the original mass, the translator barely moves as the rotor skips right over the magnetic phases.

In this test, as can be seen in figure 6.37, the rotor follows the reference fairly well initially, however it rapidly shoots off in one direction once the translator error is established substantially enough. This is likely also due to the controller scaling due to the slip not having a lower bound and causing runaway behavior.

The undesirable slip behavior can be clearly seen in figure 6.38 where only the test with no change in mass stays within the stable region for any extended period of time.

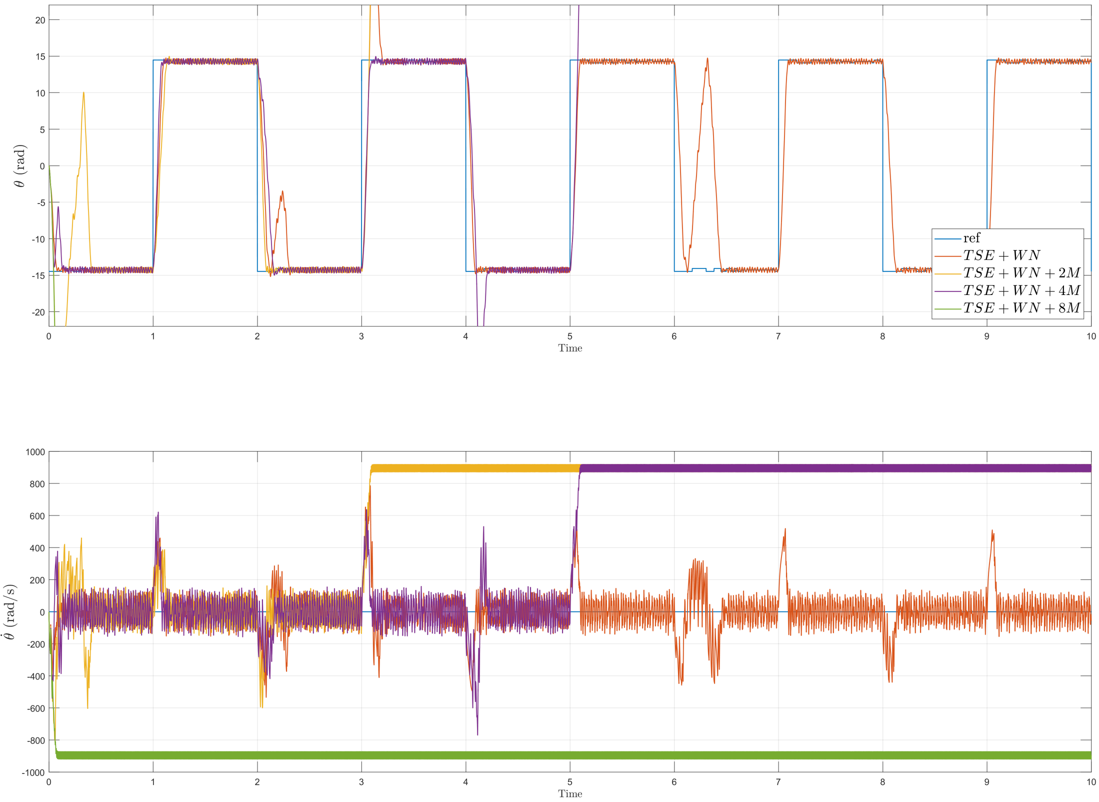

Figure 6.37: Rotor behavior when controlled with different disturbances and state estimated position feedback.

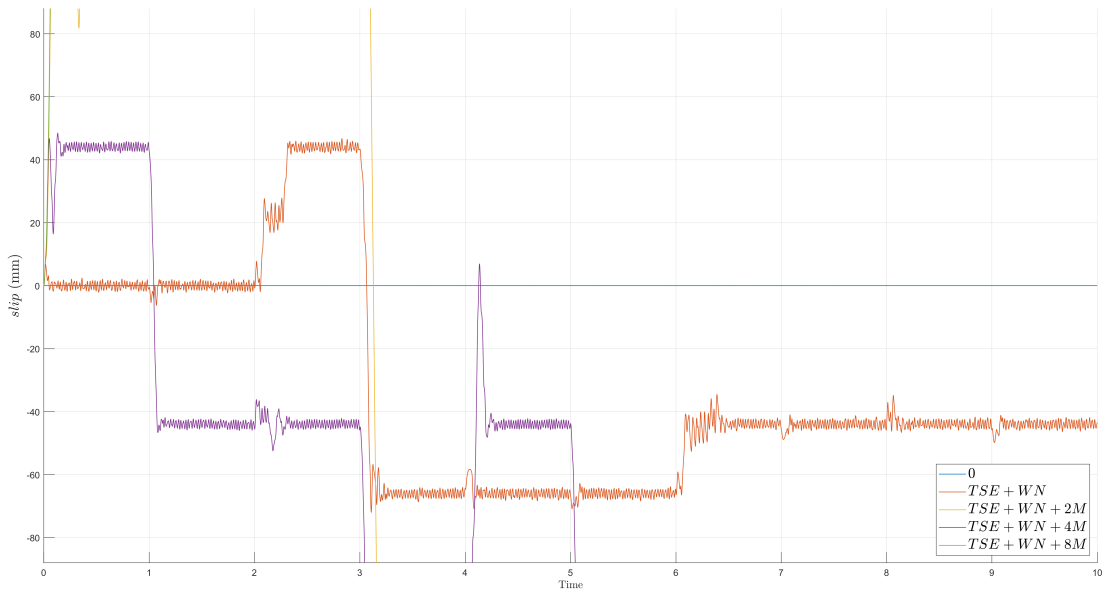

Figure 6.38: Slip behavior when controlled with different disturbances and state estimated position feedback.

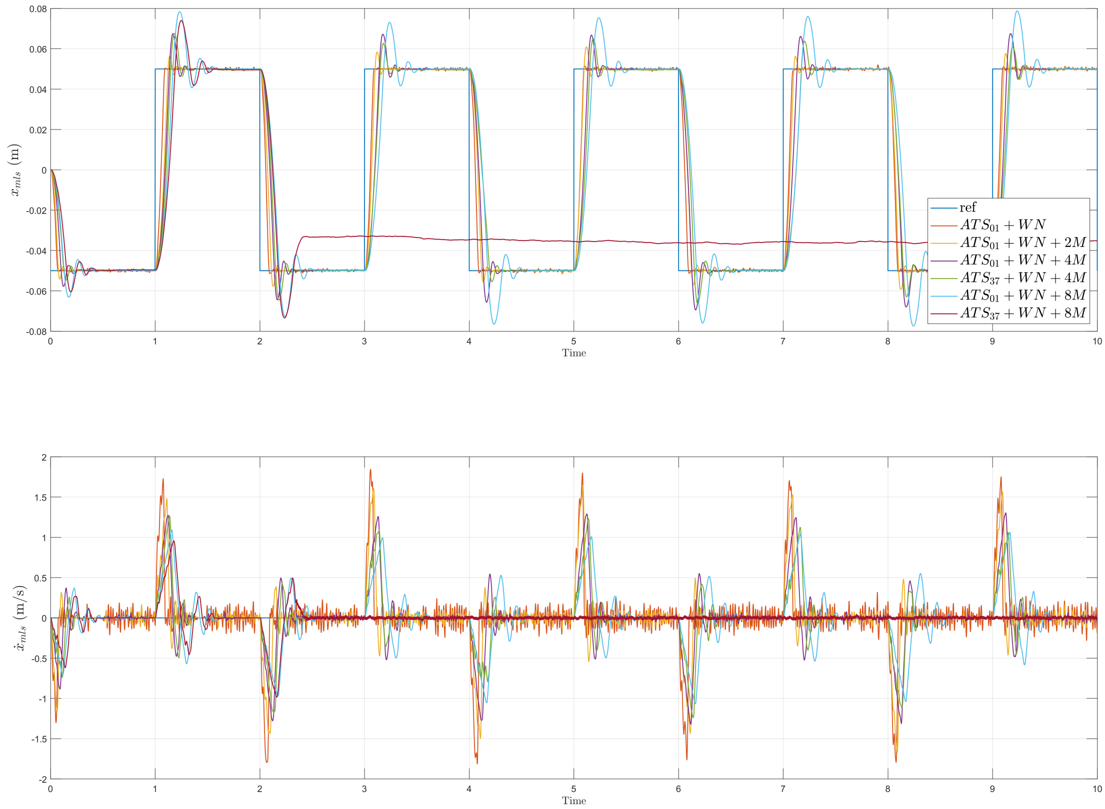

Figure 6.39: Translator behavior when controlled with different disturbances and additional sensors as feedback.

When additional sensors are used under the same test, the translator response, as seen in figure 6.39, eventually settles to zero in almost all cases. As the mass is increased, the overshoot increases which can be expected with the model-based design of the controller. It can be seen that the lower resolution sensing can be fairly effective until a large load is added where it only survives one period of the reference.

In all of these test cases, seen in figure 6.40, the rotor can be seen to show the same result. Each of the methods other than the low resolution measurement with a large mass follow the reference. In the failed test scenario, the rotor slips off in one direction and does not return. In figure 6.41, the slip can be seen to confirm the previous results.

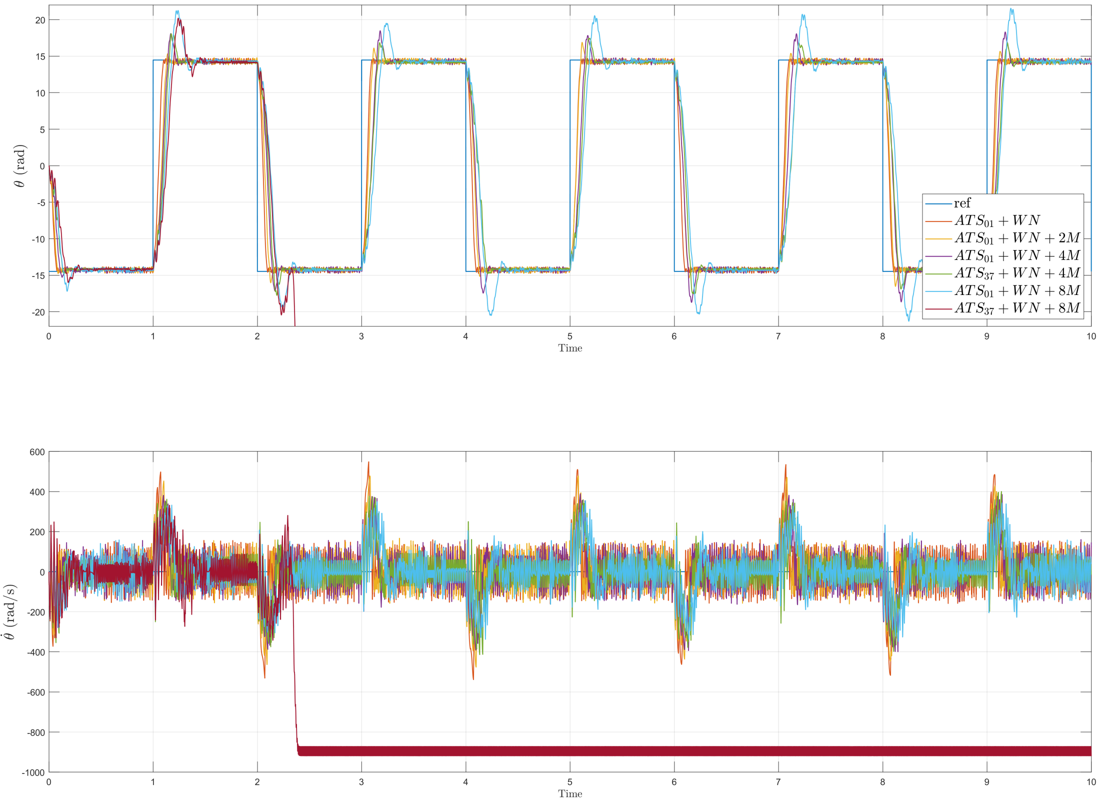

Figure 6.40: Rotor behavior when controlled with different disturbances and additional sensors as feedback.

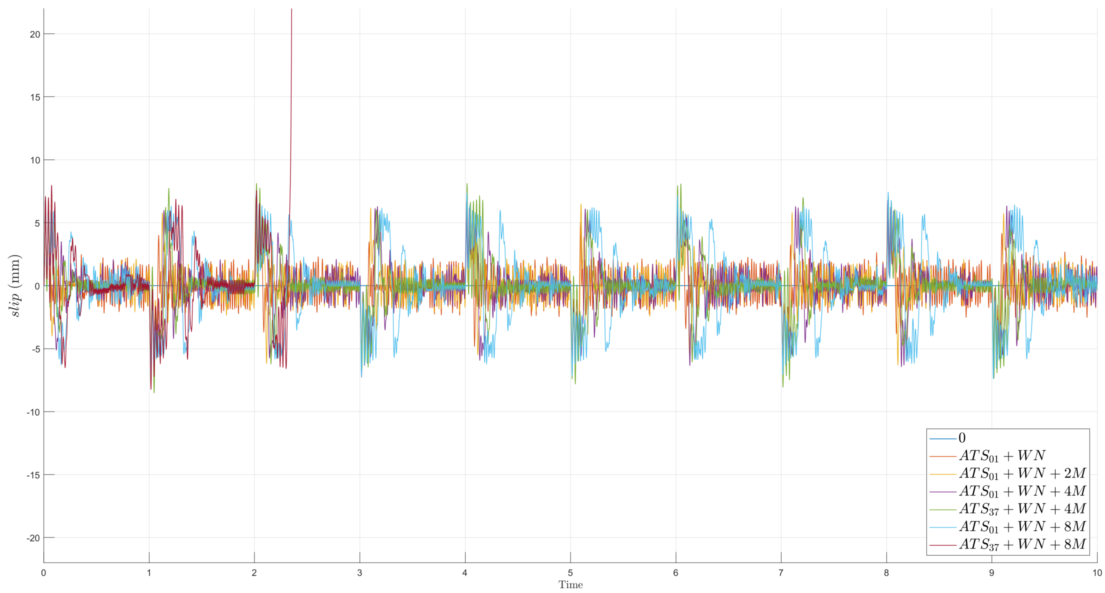

Figure 6.41: Slip behavior when controlled with different disturbances and additional sensors as feedback.

7 State Estimation

In order to interpolate the limited feedback from the hall effect sensors and to estimate the values of the unmeasured states, various Luenberger observers are created based on the linear model.

7.1 Rotor Projected Position

The simplest method that can be used to identify the MLS translator position utilizes the sensor measurements to predict the position of the translator. The sensor values and the discrete derivatives of them are multiplied by $\frac{\gamma}{6.28}$ to give the position of the MLS if there were to be zero slip. Further description of this configuration is present in section 6.6.3. This method is very computationally efficient but does not allow for the controller to compensate for the nonlinearity of the MLS force.

7.2 Rotor State Estimator

In order to create a state estimator for the rotor position and velocity, the previously found rotor response transfer function is used to create a reduced state space model.

$$L_{i_q,\dot{\theta}} = \frac{1284(s^2 + 31.45s + 2.856e4)}{(s + 32.92)(s^2 + 32.53s + 4.957e4)} \tag{7.1}$$

$$L_{i_q,\dot{\theta}} = \frac{1284s^2 + 4.039e04s + 3.667e07}{s^3 + 65.45s^2 + 5.064e04s + 1.632e06} \tag{7.2}$$

In order to convert the model into a state space format, the following method is used[15]:

$$\frac{y}{u} = L_{i_q,\dot{\theta}} = \frac{1284s^2 + 4.039e04s + 3.667e07}{s^3 + 65.45s^2 + 5.064e04s + 1.632e06} \frac{N(s)}{D(S)} \tag{7.3}$$

$$\frac{y}{u} = \frac{y}{v}\frac{v}{u} \tag{7.4}$$

$$\frac{y}{v} = N(s) \quad \frac{v}{u} = \frac{1}{D(s)} \tag{7.5}$$

Where v is the estimator state variable. From $\frac{v}{u} = \frac{1}{D(s)}$, the characteristic equation is converted to a differential form.

$$u = \dddot{v} + a_1\ddot{v} + a_2\dot{v} + a_3 \tag{7.6}$$

$$u = \dddot{v} + 65.45\ddot{v} + 5.064e04\dot{v} + 1.632e06 \tag{7.7}$$

From this, the first portion of the state space model is defined as:

$$\boldsymbol{x} = \begin{bmatrix} \ddot{v} \\ \dot{v} \\ v \end{bmatrix} \qquad \dot{\boldsymbol{x}} = A_2\boldsymbol{x} + B_2 u \tag{7.8}$$

$$A_2 = \begin{bmatrix} -a_1 & -a_2 & -a_3 \\ 1 & 0 & 0 \\ 0 & 1 & 0 \end{bmatrix} \qquad B_2 = \begin{bmatrix} 1 \\ 0 \\ 0 \end{bmatrix} \tag{7.9}$$

A similar process is followed for the denominator considering $\frac{y}{v} = N(s)$.

$$y = b_1\ddot{v} + b_2\dot{v} + b_3 v \tag{7.10}$$

$$= \begin{bmatrix} b_1 & b_2 & b_3 \end{bmatrix} \begin{bmatrix} \ddot{v} \\ \dot{v} \\ v \end{bmatrix} \tag{7.11}$$

$$= C_2\boldsymbol{x} + [0]u \tag{7.12}$$

As this does not consider the position, but only the inertia, the integral of the output may be added to include the state.

$$A_2 = \begin{bmatrix} -a_1 & -a_2 & -a_3 & 0 \\ 1 & 0 & 0 & 0 \\ 0 & 1 & 0 & 0 \\ b_1 & b_2 & b_3 & 0 \end{bmatrix} \qquad B_2 = \begin{bmatrix} 1 \\ 0 \\ 0 \\ 0 \end{bmatrix} \tag{7.13}$$

$$y = \begin{bmatrix} b_1 & b_2 & b_3 & 0 \\ 0 & 0 & 0 & 1 \end{bmatrix} \begin{bmatrix} \ddot{v} \\ \dot{v} \\ v \\ \hat{\theta}_r \end{bmatrix} \tag{7.14}$$

$$\begin{bmatrix} \dot{\hat{\theta}}_r \\ \hat{\theta}_r \end{bmatrix} = C_2\boldsymbol{x} + [0]u \tag{7.15}$$

The state space model is applied to the system in a discrete form found through the same method with the discrete time transfer function. The state space model is adapted to the state measurements through the use of an adaptation gain K found through pole placement.

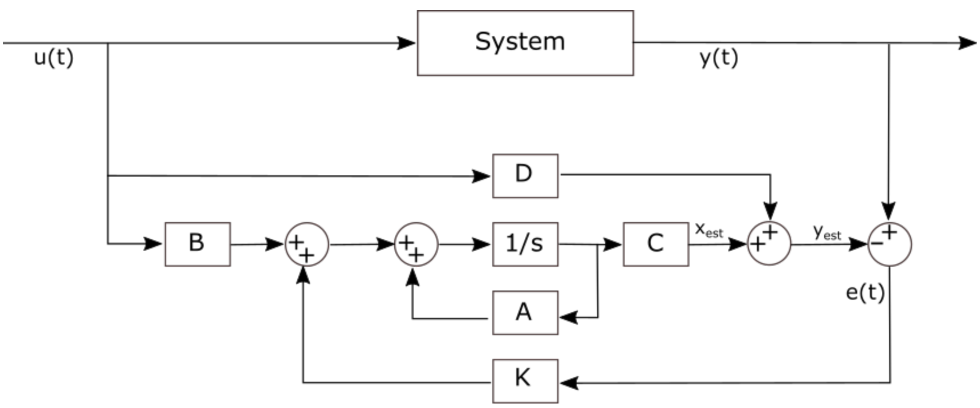

Figure 7.1: Standard form of a Luenberger observer.

The state feedback is quantized to match the measurement resolution of the hall effect sensors, a zero order hold is applied, and the discrete derivative is calculated. This gives feedback on two of the four states. The MLS translator states are calculated by projecting them from the values of the rotor position.

7.3 MLS Translator State Estimator

Creating a state estimator for the MLS translator follows much the same process, however, the transfer function used is the one defined by the relation between the rotor response and the translator response.

$$\frac{L_{\dot{\theta}}}{L_{\dot{x}}} = \frac{100}{s^2 + 31.45s + 2.856e4} \tag{7.16}$$

From this transfer function, the same process as for the rotor state estimator is used. The input to the state estimator is the measured rotor position and velocity. In this case, there is no adaptation gain as there is no measured state to be fed back to the estimator.

7.4 Combined State Estimator

The combined state estimator uses the mechanical system reduced state space model discussed previously in section 4.1. For this, the C matrix is changed to reduce the state feedback.

$$C_{est} = \begin{bmatrix} 1 & 0 & 0 & 0 \\ 0 & 1 & 0 & 0 \end{bmatrix} \tag{7.17}$$

The model is discretized and implemented in simulink where the adaptation gain is again calculated through pole placement.

7.5 Testing of State Estimators

In order to test the various state estimation methods, the estimators were implemented on the current controlled nonlinear model with a 10 amp step input given. As the system is sampled and the velocity is not directly measurable, the zero order hold sampled signal and the discrete derivative of it are the only available signals to the estimators.

In the state estimation of the rotor position and velocity seen in figure 7.2, it can be seen that all of the methods behave rather differently. The position is most accurately represented by the zero order hold as can be expected, however the discrete time derivative of this signal does not give the most accurate representation of the actual value. The rotor state estimator can be seen to have a similar behavior and to have a slightly worse performance than the zero order hold. The combined state estimator has a more continuous measurement and is fairly accurate, however there are still some discrepancies.

The state estimation of the MLS translator is the more challenging state to evaluate as it has no feedback loop. From this test it can be seen that the rotor projected position and the projection from the rotor state estimator do not capture the dynamics of the translator well and, as can be expected, do not capture the correct phase shift. The translator state estimator and the combined state estimator are more promising as the dynamics are more effectively captured.

When the error between the actual value and the estimated value is calculated, the performance is easier to visualize. From the squared error of the rotor estimation, shown in figure 7.5, it can be seen that the

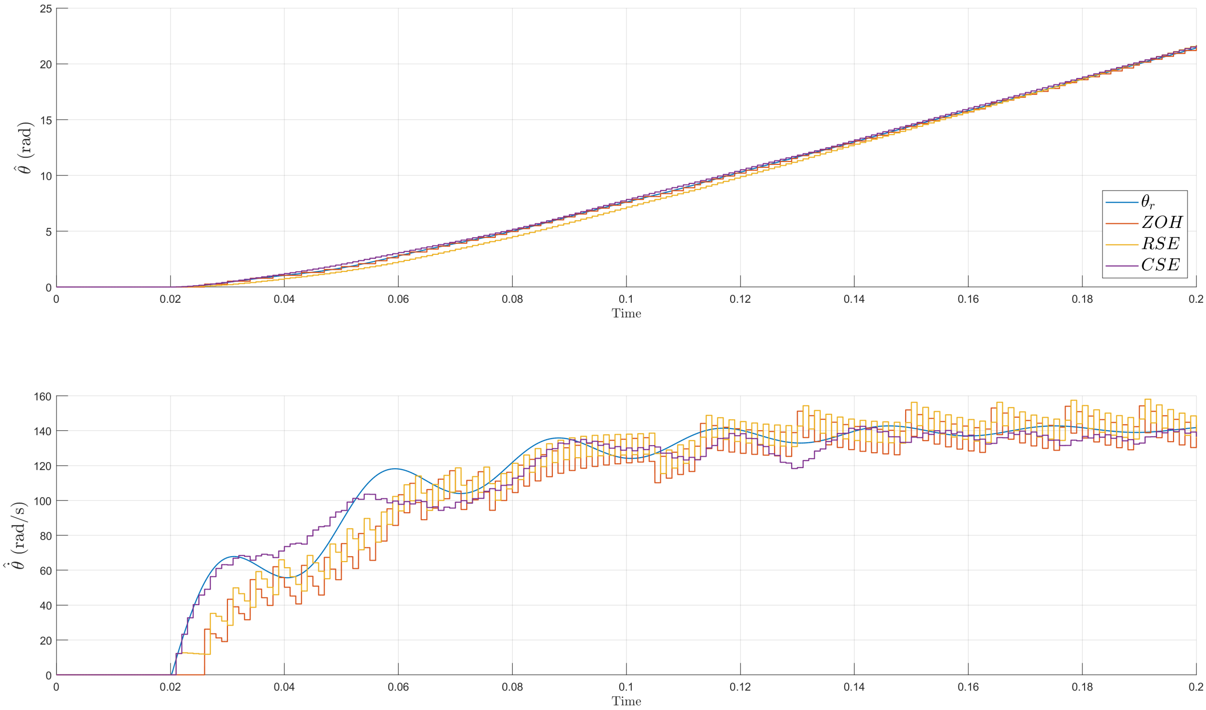

Figure 7.2: Rotor state estimation tested with a step input and various methods.

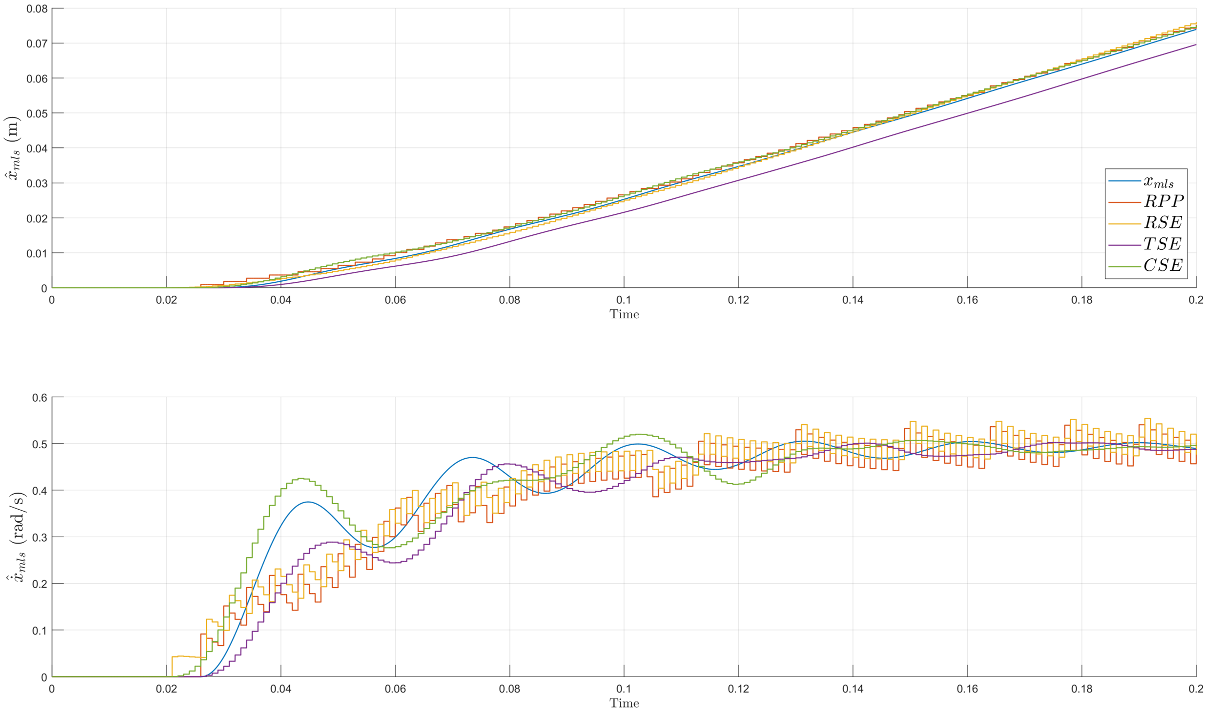

Figure 7.3: MLS state estimation tested with a step input and various methods.

zero order hold gives a very accurate approximation of the position, but the velocity is not very accurate. The combined state estimator on the other hand, can be seen to be relatively effective overall.

Looking at the squared error for the translator position in figure 7.5, the translator state estimator can be seen to suffer significantly due to the lack of state feedback. The rotor projected position and that projected from the rotor state estimator fare comparably better, however the combined state estimator again presents the best performance.

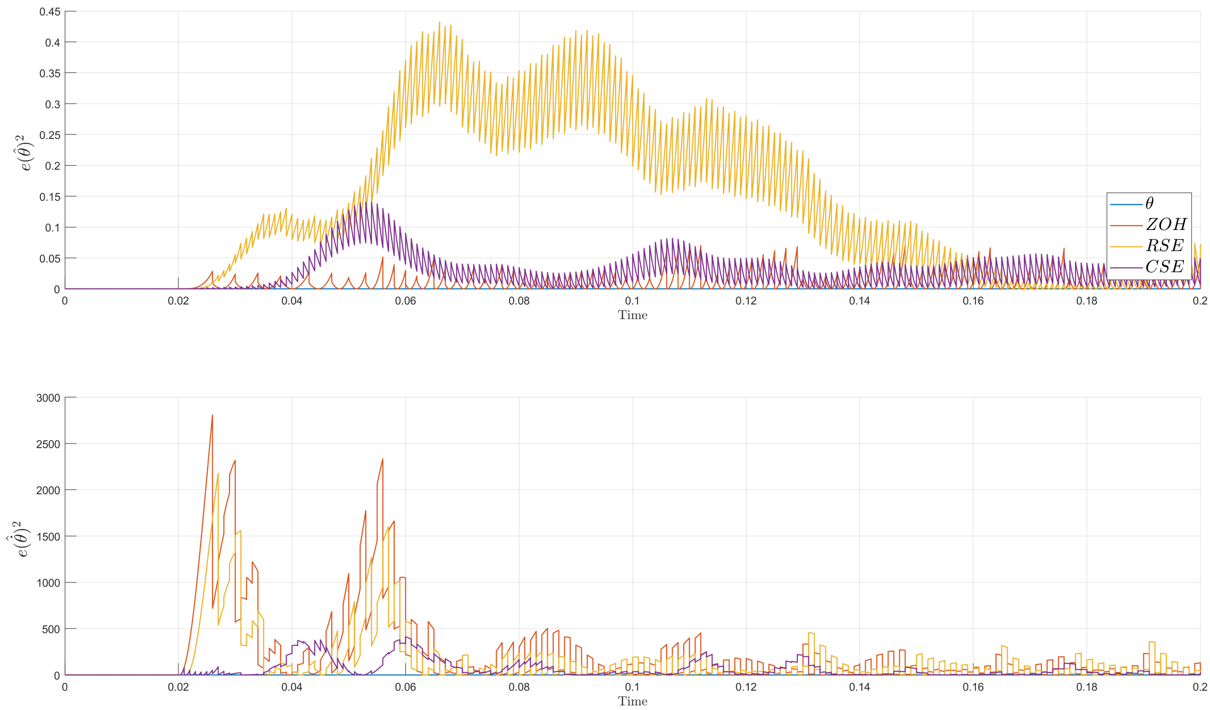

Figure 7.4: Rotor state estimation error across various methods.

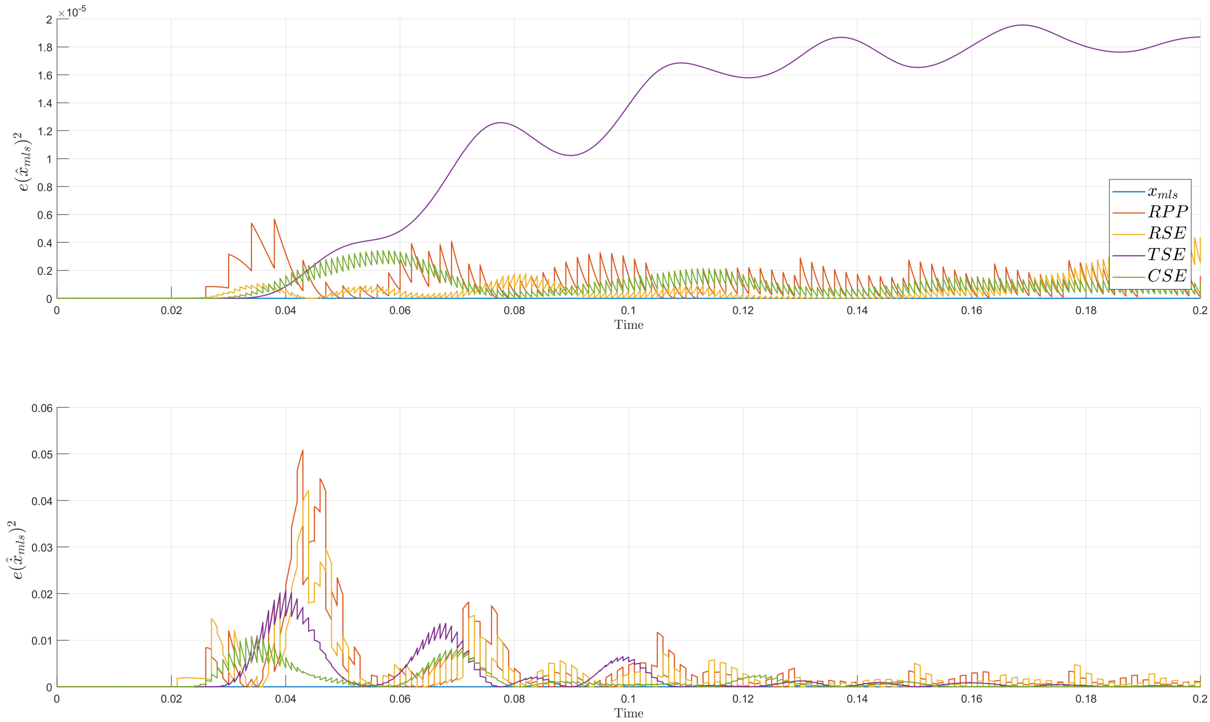

Figure 7.5: MLS state estimation error across various methods.

Conclusion 8

The original research question defined at the beginning of this thesis was: *How effectively can a magnetically driven lead screw be controlled in a way that maintains position accuracy while prioritizing speed in conditions where a load and/or disturbances are present?* Based on this question, a system model was developed and the behavior validated in comparison to that expected from the system. From the developed model, various controllers were developed based on the expected hardware implementation of the controllers. Each of the controllers were evaluated based on the speed to settle with a square wave trajectory as well as the peak overshoot. The best of the controllers were additionally tested with limited state feedback as well as with some methods to compensate for the reduced feedback.

The system model was developed based on the relatively standard method of representing the motor in the fixed rotor reference frame and the addition of the mechanical system model of the MLS translator based on the sinusiodal force curve identified in previous works. In testing of this model, with parameters identified from motor measurements, the behavior was found to match with the values stated in the specifications provided by the creators of the test setup.

A overarching control scheme was developed based on the expected implementation of the system as well as the frequency responses of the system obtained from analysis of a linearized system model. From this, it was decided to make a cascaded current control scheme where the current controllers are considered independent from the mechanical system control. With this independence in mind, PID current controllers were developed with an effective settling time of 0.001seconds and reasonable rejection of disturbances. Based on the system model with assumed ideal current control, as the current controllers are much faster than the mechanical system, controllers were developed in order to control the rotor-MLS slip, calculate the exact current for a given MLS force, and control all of the mechanical system states. Each of these controllers showed promise however they all lost some effectiveness as the mechanical system approached the most nonlinear region.

	T_s(5cm)	T_s(10cm)	OS(5cm)	OS(10cm)
SC_{DD}	0.14sec	$--$	5mm	4mm
SC_{NL}	0.15sec	0.19sec	3mm	3.7mm
CC_{DD}	$--$	$--$	$--$	$--$
CC_{NL}	$--$	$--$	3mm	$--$
$K_{s,cos}$	0.067sec	0.10sec	1.1mm	1.1mm
$K_{s,2}$	0.067sec	0.087sec	1.1mm	0.3mm
$K_{s,3}$	0.067sec	0.092sec	1.1mm	0.98mm

Table 8.1: Performance of the various developed controllers, $--$ denotes that the response did not settle within 1mm of the reference.

As the linear quadratic regulator was the most effective and robust of the controllers tested, the tests were redone with a discrete time realization and with various configurations of additional sensors on the MLS translator as well as various state estimation schemes. From these, it was found that direct sensor feedback is much more reliable than state estimation, however, of the state estimation methods tested, utilizing the rotor sensor feedback as-is and utilizing a linear estimator for the translator worked fairly well. When disturbances or loads were added to the system however, the linear state estimation methods fell short and the addition of sensors or some further nonlinear estimation became necessary.

	T_s(5cm)	T_s(10cm)	OS(5cm)	OS(10cm)
ZOH	0.058sec	0.089sec	0.8mm	0.8mm
ATS_1	0.059sec	0.093sec	0.2mm	0.6mm
ATS_{01}	0.58sec	0.11sec	0.4mm	1.3mm
$cRPP$	$--$	$--$	$--$	$--$
$RSE + RPP$	$--$	$--$	$--$	$--$
TSE	0.077sec	0.085sec	0.6mm	0.5mm
CSE	0.190sec	0.101sec	2.3mm	1.5mm

Table 8.2: Performance of LQR with various state feedback configurations, $--$ denotes that the response did not settle within 1mm of the reference.

All in all, the reluctance magnetic lead screw system is controllable with the above described methods and, if implemented in a way that can achieve the stated sensing frequencies, should be capable of traveling a distance of 10cm within 0.1 seconds without significant overshoot or oscillation. In order to achieve this response, a linear quadratic regulator was found to be the best method of balancing control of the rotor and the translator while prioritizing speed. For loads to be added, the system must be augmented with either an extremely effective state estimation scheme, or some position sensors, for which a resolution of 1mm should be sufficient for compensating both the loading inconsistencies as well as detecting the MLS slip. Overall this thesis defines that reluctance magnetic lead screws, though with a more complex control structure than typical linear actuators, can be controlled effectively at high speeds and with high loads compared to the system size.

Future Work 9

Beyond the work conducted in this thesis, further work must be conducted in order to bring the RMLS prototype to a commercially-viable controlled linear actuator system. For this to be possible, further controllers should be tested, specifically those more targeted towards nonlinear systems. Furthermore, nonlinear state estimation may be a possible solution to the sensor reliance seen in the testing when an unknown load is added. As the system behavior is very parameter specific, some method of system identification would likely be useful for applying control to an unknown RMLS or PMMLS configuration. Related to this, some controller robustness to a varying load will be necessary and would likely require some form of online load measurement. Lastly, the control systems need to be implemented in hardware and tested relative to the actual physical behavior of the RMLS system.

As the results of the controller testing demonstrate that every controller still has some excitation dynamics due to the nonlininearity in the system, the implementation of controllers more targeted towards nonlinear systems are a clear next step in developing optimized control of the system. Directly building from the controllers developed, gain scheduling would be a relatively simple next step for compensating the system behavior[13]. As the gain scheduling would depend on the slip position, this would either require position sensors, or a very accurate state estimation scheme. Aside from linear methods an adaptive inverse dynamics controller would likely be an effective method for controlling both the MLS translator, as well as adapting for an uncertain load. The mechanical may be considered in a fourth order differential equation from which a controller may be developed[16]. Similarly, as the current dynamics are very fast, a sliding mode controller may be an option for handling the static friction and unknown loads of the system, however the excitation of the system may be a concern with the discontinuous input[16].

As the addition of gain scheduling would require accurate position measurement, an alternative to additional sensors could be the addition of some form of state estimation such as an extended Kalman filter (EKF)[17]. In combination with a lower resolution position sensor, this could also be used to compensate for unknown loading scenarios.

As the parameters of every industrial setup would not be identical, some form of system identification for detecting the system parameters would allow for the controller to further extend the gain scheduling to use a lookup table for different sets of system parameters. Such parameters would be those such as the motor resistance, inductance, and motor constant, as well as the rotor inertia and translator mass. Detecting these would allow the controllers, even if they adapt to system parameters, to better define themselves around some more correct 'hard' parameters. This could also be extended, perhaps with the use of an EKF to detect the loading scenario while under use.

Of course to test any of these, the control must be implemented on a microcontroller and with an inverter board as shown in figure 6.1. The IHM08M1 board considered in this thesis could be fitting for minimal control of the system, however the peak current it is capable of is half the peak value of the motor. For basic testing the inverter is fine as the peak torque possible with this current is 0.93Nm, however this only corresponds to a peak force of 265N and thus would theoretically not be able to slip fault which does not allow for testing of controller slip fault robustness and would limit the maximum positioning speed of the rotor.

Bibliography

[1] Nick Berg, Rasmus Holm, and Peter Rasmussen. A novel magnetic lead screw active suspension system for vehicles. *2014 IEEE Energy Conversion Congress and Exposition, ECCE 2014*, pages 3139–3146, 09 2014.

[2] B. Andrews. Magnetic screw, May 4 1925. US1562730A.

[3] Harold T. Faus. Magnetic transmission, March 13 1945. US2371511A.

[4] Nicholas Gerard Vitale. Rotary torque to axial force energy conversion apparatus, November 16 1999. US5984960A.

[5] Nick Ilsø Berg, Rasmus Koldborg Holm, and Peter Omand Rasmussen. A novel magnetic lead screw active suspension system for vehicles. In *Proceedings of the 2014 IEEE Energy Conversion Congress and Exposition (ECCE)*, pages 3139–3146. IEEE Press, 9 2014. 2014 IEEE Energy Conversion Congress and Exposition (ECCE) ; Conference date: 14-09-2014 Through 18-09-2014.

[6] A. Stupakowski, A. Højris, M. Pentek, M. Stati, and V. Mishukov. Microprocessor implementation of passive damping/skyhook schemes in a vehicle using permanent magnet synchronous motor and magnetic lead screw. Technical report, AAU, 2019.

[7] Nick Ilso Berg, Alexander Becsei Christiansen, Rasmus Koldborg Holm, and Peter Omand Rasmussen. Design and test of a reluctance based magnetic lead screw pto system for a wave energy converter. In *2017 IEEE International Electric Machines and Drives Conference, IEMDC 2017*, United States, 8 2017. IEEE. 2017 IEEE International Electric Machines and Drives Conference, IEMDC 2017 ; Conference date: 21-05-2017 Through 24-05-2017.

[8] Mateus Cirolini, Aly Ferreira Flores Filho, Yi Chen Wu, and David G Dorrell. Design aspects of a reluctance-based magnetic lead screw. *IEEE Transactions on Magnetics*, 55(7):1–6, 2019.

[9] STMicroelectronics. *Low-Voltage BLDC motor driver expansion board based on STL220N6F7 for STM32 Nucleo.* "https://www.st.com/resource/en/data_brief/x-nucleo-ihm08m1.pdf", 2017.

[10] Peter O. Rassmusen. *AC Motor Drives: Converters and Control: Dynamic model and control of the PMSM.* "https://movement.osu.edu/Courses/ME8230NonlinearDynamics_Sp2016/LectureNotes/L14_ForcedNonlinearSystemsPhenomena.pdf", 2018.

[11] M.P. Kazmierkowski and H. Tunia. *Automatic Control of Converter-Fed Drives.* Automatic Control of Converter-fed Drives. Elsevier Science, 1994.

[12] Manoj Srinivasan. *Basic phenomenology of simple nonlinear vibration.* "https://movement.osu.edu/Courses/ME8230NonlinearDynamics_Sp2016/LectureNotes/L14_ForcedNonlinearSystemsPhenomena.pdf", 2016.

[13] Sigurd Skogestad and Ian Postlethwaite. *Multivariable Feedback Control: Analysis and Design.* John Wiley & Sons, Inc., Hoboken, NJ, USA, 2005.

[14] John M. Parr Charles L. Philips. *FEEDBACK CONTROL SYSTEMS.* Number ISBN-13: 978-0-13-186614-0 in 5th edition. Pearson, 2011.

[15] MIT OCW. *Topic #6 16.30/31 Feedback Control Systems.* "https://ocw.mit.edu/courses/aeronautics-and-astronautics/16-30-feedback-control-systems-fall-2010/lecture-notes/MIT16_30F10_lec06.pdf", 2010.

[16] Jean-Jaques E. Slotine and Weiping Li. *Applied Nonlinear Control.* Prentice Hall, Inc., Upper Saddle River, NJ, USA, 1991.

[17] Rolf Isermann. *Fault Diagnosis Systems - An Introduction from Fault Detection to Fault Tolerance.* Springer-Verlag, Berlin Heidelberg, Germany, 2006.